

**ELECTROCHEMICAL STUDIES
OF TITANIUM, MANGANESE
AND COBALT
PHTHALOCYANINES**

A thesis submitted in fulfillment of the requirements for the degree of

MASTER OF SCIENCE

Of

RHODES UNIVERSITY

By

NOLWAZI NOMBONA

January 2009

DEDICATION

To my parents

Mphathelwa and Nomzi Nombona

and

to all who believe in the richness of learning.

Acknowledgements

I wish to thank God for giving me such a lovely environment that made this work possible.

Everyone is influenced by a great thinker; I am privileged to have been influenced by Prof. T. Nyokong at a time when I was a clueless undergraduate student! Prof., thank you for your valuable guidance, detailed comments and support throughout this project, without which this work would not have been possible. Thank you for the wonderful opportunities that you have given me, the three months I spent in Belgium are most memorable; I never thought travelling could be so much fun! I absolutely enjoyed the experience. Thank you for the SEANAC (Botswana) and ICCPP (Russia) conferences I attended under your supervision.

I acknowledge the significant contribution of these individuals who have provided encouragement and mentoring: Dr. Nthapo Sehlotho, Dr. Prudence Tau, Dr. Daniela Geraldo, Dr. Phillipe Westbroek, Dr. Jean Hakuzimana, and Dr. Edith Antunes. Thank you.

I wish to thank my family: *Mama, Tata* (for being positive role models in my life) and my siblings. You have given me love, support and encouragement to further my studies. Thank you for all your prayers. *Ndithi, Mashiya amahle nje nge nyamazane*, I love you all dearly. To my friends, thank you for the good laughs and the wonderful times.

I would like to thank the chemistry department for the lovely tea times ☺ and for providing a marvelous research environment, a special thank you to Mr. Andre Adriaan for helping with the construction of my electrodes and to Ms Gail Cobus for all her help. I thank the Andrew Mellon Foundation and NRF for financial assistance and I would like to thank Gent University (Belgium) for the lovely experience which was made possible through the bilateral research project funded by NRF (SA) and UGent-BOF (Belgium).

The future belongs to those who believe in the beauty of their dreams-Eleanor Roosevelt

Abstract

Syntheses, spectral, electrochemical and spectroelectrochemical studies of phenylthio and amino derivatised metallophthalocyanines complexes are reported. The complexes are immobilized onto a gold macro disk, gold ultramicroelectrode and gold coated fiber electrodes via self assembly with phenylthio MPc derivatives or onto a glassy carbon electrode via electropolymerisation with amino MPc derivatives. For the first time MPc SAMs were formed on gold coated fiber. The electrocatalytic behavior of the modified electrodes was studied for the detection of nitrite and L-cysteine, all modified electrodes showed improved electrocatalytic oxidation compared to the unmodified electrode. The MPc complexes catalyzed nitrite oxidation via a two-electron mechanism producing nitrate. Cobalt tetraaminophthalocyanine showed the best catalytic activity for nitrite oxidation in terms of overpotential lowering compared to other complexes and thus was used for nitrite detection in a food sample, the nitrite concentration was determined to be 59.13 ppm, well within the limit for cured meat products.

Electrocatalytic oxidation of L-cysteine on SAM modified gold coated fiber was reported for the first time. The gold coated fiber and ultramicro cylinder electrode were less stable towards the electro-oxidation of cysteine compared to its oxidation on the gold disk. The gold disk electrode gave better catalytic performance in terms of stability and reduction of overpotential. The phenylthio cobalt phthalocyanine derivative gave the best catalytic activity for L-cysteine oxidation in terms of overpotential lowering compared to other phenylthio derivatized MPc complexes. The amount of L-cysteine in human urine was 2.4 mM, well within the urinary L-cysteine excretion range for a healthy human being.

Table of contents

Title page	i
Dedication	ii
Acknowledgements	iii
Abstract	iv
Table of contents	v
List of abbreviations	ix
List of symbols	xi
List of figures	xiv
List of schemes	xviii
List if tables	xix

Chapter 1: Introduction

1.1 Electrocatalysis	2
1.2 Phthalocyanines: An overview	5
1.2.1 Discovery, structure and general applications	5
1.2.2 The synthesis of phthalocyanines	8
1.2.3 Electronic structure and spectroscopy of phthalocyanines	11
1.2.4 The electrochemistry of phthalocyanines	15
1.2.5 Electrocatalytic behaviour of metallophthalocyanines	17
1.2.5.1 Tuning of metallophthalocyanine redox potential	18
1.2.5.2 Mode of electrocatalysts	19
1.3 Modes of electrode modification for electrocatalysis	23
1.3.1 Electropolymerization.....	24
1.3.2 Self assembled monolayers (SAMs).....	26

1.3.2.1 Types of SAMs	27
1.3.2.2 Electrodes used	28
1.3.2.2.1 Textile electrodes	29
1.3.2.2.2 Ultramicroelectrodes (UMEs).....	31
1.3.3 Characterization of modified electrodes	33
1.4 Overview of voltammetric methods employed.....	35
1.4.1 Cyclic voltammetry.....	35
1.4.2 Spectroelectrochemistry.....	37
1.4.3 Rotating disk voltammetry.....	38
1.5 Electrocatalysis of biologically important compounds by MPes.....	43
1.5.1 An overview of nitrite catalysis	43
1.5.2 An overview of L-cysteine catalysis.....	46
1.6 Summary of aims	49

Chapter 2: Experimental

2.1 Materials	52
2.2 Instrumentation	53
2.3. Electrochemical methods	53
2.4 Synthesis	55
2.4.1 Phthalonitriles	55
2.4.1.1 3-Nitrophthalonitrile	55
2.4.1.2 4-Nitrophthalonitrile	57
2.4.1.3 Phenylthiosubstituted phthalonitriles.....	58
2.4.2 Phthalocyanines	59
2.4.2.1 Phenylthio tetra-substituted phthalocyanines	59
2.4.2.2 Amino substituted phthalocyanines	60
2.5 Nitrite sample preparation.....	62

Chapter 3: Synthesis and characterization of MPc derivatives

3.1 Synthesis and spectral characterization	66
3.1.1 Phthalonitriles	66

3.1.1.1 Nitro substituted phthalonitriles	66
3.1.1.2 Phenylthio derivatised phthalonitrile	68
3.1.2 Phenylthio derivatized metallophthalocyanines	69
3.1.2.1 CoPc derivatives	72
3.1.2.2 (OH)MnPc and OTiPc derivatives.....	73
3.1.3 Amino-derivatised phthalocyanines.....	74
3.1.3.1 Cobalt tetraaminophthalocyanine (CoTAPc)	76
3.1.3.2 Managese tetraaminophthalocyanine ((OH)MnTAPc)	76
3.1.3.3 Titanium tetraaminophthalocyanine (OTiTAPc)	77
3.2 Electrochemical characterization	79
3.2.1 Phenylthio derivatised phthalocyanines.....	81
3.2.1.1 CoPc derivatives	81
3.2.1.2 MnPc derivatives	92
3.2.2 Amino-derivatised phthalocyanines.....	97
3.2.2.1 CoTAPc	97
3.2.2.2 (OH)MnTAPc	101
3.2.2.3 OTiTAPc	107

Chapter 4: Electrode modification and characterization

4.1 Self assembled monolayers.....	113
4.1.1 Fabrication of gold ultramicrocylinder and fiber electrodes.....	113
4.1.2 SAM formation on gold electrodes.....	114
4.1.2.1 SAM characterization of the gold disk electrode.....	115
4.1.2.2 SAM characterization of gold ultramicro cylinder electrodes (UMCE). 119	
4.1.2.3 SAM characterization of gold coated fiber electrodes.....	122
4.1.3 Redox couples of MPcs on SAM electrodes.....	124
4.2 Electropolymerization.....	129

Chapter 5: Electrocatalysis

5.1 Nitrite electrocatalytic oxidation.....	138
5.1.1 SAM modified gold electrodes	138

5.1.2 MTAPc modified electrodes	148
5.1.3 Nitrite detection in a food sample.....	155
5.2 L-cysteine electrocatalytic oxidation	158
5.2.1 L-cysteine oxidation on SAM modified gold disk electrodes	158
5.2.2 L-cysteine electrooxidation on UMCE and Au coated fiber electrodes	165
5.2.3 L-cysteine detection in biological media	172

Chapter 6: Conclusion

6. Conclusion	176
---------------------	-----

References

References.....	181
-----------------	-----

List of abbreviations

Ac₂O	-	Acetic anhydride
Ag AgCl	-	Silver-silver chloride electrode
Au	-	Gold working electrode
CoPc	-	Cobalt phthalocyanine
CoTNPc	-	Cobalt tetranitrophthalocaynine
CoTAPc	-	Cobalt tetraaminophthalocaynine
CME	-	Chemically modified electrode
CV	-	Cyclic voltammetry Cyclic voltammogram
DBU	-	1, 8-diazabicyclo[5.4.0]undec-7-ene
DMF	-	N, N-dimethylformamide
DMSO	-	Dimethylsulphoxide
GCE	-	Glassy carbon electrode
H₂Pc	-	Metal-free phthalocyanine
¹H-NMR	-	Proton nuclear magnetic resonance
HOMO	-	Highest occupied molecular orbital
HPLC	-	High performance liquid chromatography
IR	-	Infrared
MPc	-	Metallophthalocyanine
MnPc	-	Manganese phthalocaynine
MnTNPc	-	Manganese tetranitrophthalocaynine
MnTAPc	-	Manganese tetraaminophthalocaynine

NH₂	-	Amino
NIR	-	Near infrared
O	-	Oxidized species
OSWV	-	Osteryoung square wave voltammetry
OTiPc	-	Oxotitanium(IV)phthalocyanine
OTTLE	-	Optically transparent thin-layer electrode
P	-	Product
Pc	-	Phthalocyanine
PDT	-	Photodynamic therapy
R	-	Reduced species
RDE	-	Rotating disk electrode
rt	-	room temperature
rds	-	rate determining step
SWV	-	Square wave voltammetry/voltamogram
S	-	Substrate
SAM	-	Self assembled monolayer
TBABF₄	-	Tetrabutylammonium tetraflouoroborate
TiPc	-	Titanium phthalocaynine
TiTNPc	-	Titanium tetranitrophthalocaynine
TiTAPc	-	Titanium tetraaminophthalocaynine
UME	-	Ultramicroelectrode
UMCE	-	Ultramicro cylinder electrode
UV/Vis	-	Ultraviolet/visible

List of symbols

α	-	Non-peripheral position
	-	Transfer coefficient
β	-	Peripheral position
e^-	-	Electron
ε	-	Extinction coefficient
λ_{\max}	-	Maximum wavelength
Γ	-	Surface coverage
Γ_{ibf}	-	Ion barrier factor
η	-	Overpotential
n	-	Number of electrons
n_t	-	Total number of electrons transferred
n_α	-	Number of electrons in rate determining step
E	-	Potential
E_{pa}	-	Anodic peak potential
E_{pc}	-	Cathodic peak potential
ΔE	-	Difference in peak potential
E°	-	Formal potential
$E_{1/2}$	-	Half wave potential
E_p	-	Peak potential
F	-	Faraday's constant
v	-	Scan rate
δ	-	Diffusion layer

	-	Parts per million
A	-	Absorbance
	-	Area of electrode
C	-	Concentration
D	-	Diffusion coefficient
I	-	Current
I_L	-	Limiting current
I_k	-	Kinetic current
I_p	-	Peak current
I_{pa}	-	Anodic current
I_{pc}	-	Cathodic current
k	-	Heterogeneous rate constant
M	-	Molar concentration
mV	-	Milli volts
Q	-	Charge
R	-	Universal gas constant
r	-	Electrode radius
T	-	Temperature
t	-	Time
v	-	Kinematic viscosity
v	-	Volume
V	-	Volt
ω	-	Angular rotation rate

C_{4h}

D_{2h}

C_{2v}

C_s



Molecular point groups of non-peripherally substituted MPCs

List of figures

Figure 1. 1: A schematic illustration of electrocatalysis.....	3
Figure 1. 2: Phthalocyanine structure	6
Figure 1. 3: Constitutional isomers of non-peripherally substituted MPcs.....	10
Figure 1. 4: Molecular structure of an MPc showing the 18- π conjugated system.	12
Figure 1. 5: Molecular orbital diagram of a phthalocyanine.....	13
Figure 1. 6: Absorption spectra of metallated and unmetallated Pcs.....	14
Figure 1. 7: The reduction and oxidation of the LUMO and HOMO.....	16
Figure 1. 8: Energy-level diagram showing Pc oxidation and reduction.....	17
Figure 1. 9: The electropolymerization a phthalocyanine on a glassy carbon electrode .	26
Figure 1. 10: Different orientations of MPc-SAMS on gold electrodes.	27
Figure 1. 11: Textile based electrode.	30
Figure 1. 12: Common ultramicroelectrode geometries.	32
Figure 1. 13: A typical Cyclic voltammogram.	36
Figure 1. 14: Streamlines for a rotating disk electrode.	39
Figure 1. 15: Current-potential RDE voltammogram for an irreversible system.	40
Figure 1. 16: Structures of Co, Mn and Ti phthalocyanines studied.	50
Figure 3. 1: ^1H NMR spectrum of 3-nitrophthalonitrile in DMSO- d_6	68
Figure 3. 2: UV/Vis spectra of 12 and 13 in DMF.	72
Figure 3. 3: UV/Vis spectrum of complex 14 and 15 in DMF.	73
Figure 3. 4: UV/Vis spectra of 16 and 19 in DMF..	76
Figure 3. 5: UV/Vis spectra of 17 and 20 in DMF..	77
Figure 3. 6: UV/Vis spectra of 18 and 21 in DMF.	78
Figure 3. 7: SWV and CV of 12 in DMF	83
Figure 3. 8: SWV and CV of 13 in DMF	84
Figure 3. 9: UV/Vis/NIR spectral changes of complex 12 in DMF	89
Figure 3. 10: UV/Vis/NIR spectral changes of complex 13 in DMF	91
Figure 3. 11: SWV and CV of 14 in DMF	93
Figure 3. 12: UV/Vis/NIR spectral changes of complex 14 in DMF	96
Figure 3. 13: SWV and CV of 19 in DMF	98

Figure 3. 14: UV/Vis/NIR spectral changes of 19 in DMF	100
Figure 3. 15: SWV and CV of 20 in DMF.....	103
Figure 3. 16: UV/Vis/NIR spectral changes of 20 in DMF	106
Figure 3. 17: SWV and CV of 21 in DMF.....	108
Figure 3. 18: UV/Vis/NIR spectral changes of 21 in DMF	110
Figure 4. 1: CVs of unmodified gold disk electrode and SAM of 12	118
Figure 4. 2: CVs of unmodified gold UMCE and SAM of 12	121
Figure 4. 3: CVs of unmodified gold coated fiber and SAM of 12	123
Figure 4. 4: Ramanscope images of bare fiber and 12 SAM-fiber.	124
Figure 4. 5: CVs of 12 , 13 and 14 in pH 4 buffer and pH 7.4 buffer.....	127
Figure 4. 6: CVs of 12 , 13 SAMs on UMCE in pH 4 buffer	127
Figure 4. 7: CVs on GCE in DMF showing the formation of <i>poly-19</i> and CV of <i>poly-19</i> film on GCE in pH 7.4.....	131
Figure 4. 8: CVs on GCE in DMF showing the formation of <i>poly-20</i> and CVs of <i>poly-20</i> film on GCE in pH 7.4.....	133
Figure 4. 9: CVs on GCE in DMF showing the formation of <i>poly-21</i> and <i>poly-21</i> film on GCE in pH 7.4.....	135
Figure 5. 1: CVs of bare Au, complex 12 , 13 , 14 and 15 SAM electrodes for 1mM nitrite oxidation in pH 7.4..	140
Figure 5. 2: Peak current variation with scan number for the electrocatalytic response of 1mM nitrite on complex 12 , 13 , 14 and 15 SAM electrodes in pH 7.4.....	140
Figure 5. 3: Peak current variation with square root of scan rate for the electrocatalytic response of 1mM nitrite on complex 12 , 13 , 14 and 15 SAM electrodes in pH 7.4.....	141
Figure 5. 4: Plot of peak current versus nitrite concentration on 12 modified electrode in pH 7.4.....	142
Figure 5. 5: Peak potential variation with logarithm of scan rate for the electrocatalytic response of 1mM nitrite on 12 , 13 , 14 and 15 SAM electrodes in pH 7.4.	142
Figure 5. 6: Spectroscopic changes of 12 observed on addition of 1mM nitrite solution in DMF to solution and on addition of NaBH ₄	146

Figure 5. 7: CVs of oxidation of 1 mM nitrite on bare GCE, <i>poly-19</i> , <i>poly-20</i> and <i>poly-21</i> modified GCE in pH 7.4.....	149
Figure 5. 8: Peak current variation with scan number for the electrocatalytic response of 1mM nitrite on <i>poly 19, 20</i> , and 21 modified electrodes in pH 7.4.....	150
Figure 5. 9: Peak current variation with square root of scan rate for the electrocatalytic response of 1mM nitrite on 12, 13, 14 and 15 SAM modified electrodes in pH 7.4.....	151
Figure 5. 10: Peak potential variation with logarithm of scan rate for the electrocatalytic response of 1mM nitrite on <i>poly-19, 20</i> and 21 electrodes in pH 7.4 buffer.....	152
Figure 5. 11: Hydrodynamic voltammograms of nitrite oxidation on <i>poly-19, 20</i> and 21 electrodes.....	154
Figure 5. 12: Tafel plot for nitrite oxidation on <i>poly 19, 20</i> and 21 electrodes for 1mM nitrite in pH 7.4 buffer solution.....	154
Figure 5. 13: Differential pulse voltammograms of bare gold disk electrode and <i>poly-19</i> SAM modified gold disk electrode in a sausage sample.....	157
Figure 5. 14: A linear dependence of peak current with increasing nitrite concentration in a sausage sample.....	157
Figure 5. 15: CVs of bare Au, 12, 13, 14 and 15 SAM electrodes for L-cysteine oxidation in pH 4.....	159
Figure 5. 16: Peak current variation with square root of scan rate for the electrocatalytic response of 1mM L-cysteine on 12, 13, 14 and 15 SAM electrodes in pH 4.....	159
Figure 5. 17: Peak current variation with scan number for the electrocatalytic response of 1mM L-cysteine on 12, 13,14 and 15 SAM electrodes in pH 4.....	161
Figure 5. 18: Peak potential variation with logarithm of scan rate for the electrocatalytic response of L-cysteine on 12, 13, 14 and 15 SAM electrodes in pH 4.....	163
Figure 5. 19: Plot of peak current versus concentration for L-cysteine in pH 4 on 12 SAM.....	163
Figure 5. 20: Hydrodynamic voltammograms of L-cysteine oxidation on SAM of complex 12,13,14 and 15	164
Figure 5. 21: CVs of bare gold UMC electrode, 12 SAM and 13 SAM in L-cysteine in pH 4.....	167

Figure 5. 22: Plot of I_p vs. CV scan number for the electrocatalytic oxidation of L-cysteine in pH 4 on 12 and 13 on Au UMCE SAMs.....	168
Figure 5. 23: CVs of bare electrode, 12 and 13 SAMs in 1mM L-cysteine in pH 4.	169
Figure 5. 24: Plot of I_p vs. CV scan number for the electrocatalytic oxidation of L-cysteine on 12 and 13 SAMs on Au coated fiber electrodes.	170
Figure 5. 25: Differential pulse voltammograms of bare gold disk electrode and 12 SAM modified gold disk electrode in a human urine sample	173
Figure 5. 26: The linear dependence of the peak current with increasing L-cysteine concentration in a urine sample.	173

List of schemes

Scheme 1. 1: Synthetic routes of MPcs from starting materials.	8
Scheme 1. 2: Electro-polymerization of an amino Pc monomer.....	25
Scheme 3. 1: Synthesis of 3-nitrophthalonitrile (5) and 4-nitrophthalonitrile (9).	66
Scheme 3. 2: Synthetic pathway to thio derivatized phthalonitriles.	69
Scheme 3. 3: Synthetic pathway for Co, Mn and Ti tetra substituted phthalocyanines...	70
Scheme 3. 4: Synthetic pathway for Co, Mn and Ti tetraaminophthalocyanines.	75
Scheme 5. 1: Proposed mechanism for the catalytic oxidation of nitrite on complex 12 and 13 SAM modified electrodes.	147
Scheme 5. 2: Proposed mechanism for the catalytic oxidation of nitrite on complex 12 SAM modified electrode.....	147
Scheme 5. 3: Proposed mechanism for the catalytic oxidation of nitrite on complex 15 modified electrode. Axial oxygen left out for clarity.	155

List of tables

Table 1. 1: Electrochemical data for the electro-oxidation of nitrite and L-cysteine using selected Ti and Mn phthalocyanine complexes.	22
Table 1. 2: Comparative peak potentials for nitrite oxidation in pH 4 buffer on MPc modified electrodes.	45
Table 1. 3: Comparative peak potentials for L-cysteine oxidation on MPc modified electrodes.	48
Table 3. 1: Main absorption bands for complexes 12-15 and 19-21	78
Table 3. 2: Summary of redox potentials of Co, Mn and Ti phenylthio Pc complexes in DMF containing 0.1 M TBABF ₄	79
Table 3. 3: Summary of redox potentials of Co, Mn and Ti amino Pc complexes in DMF containing 0.1 M TBABF ₄	80
Table 4. 1: Surface coverage and ion barrier factor values for the various MPcs-SAMs in pH 4 buffer solution.	129
Table 5. 1: Electrocatalytic oxidation of 1mM nitrite at modified electrodes with complexes 12-15 and 19-21 in pH 7.4 buffer solution.	139
Table 5. 2: Electrocatalytic oxidation of 1mM L-cysteine at SAM modified electrodes with complexes 12, 13, 14 and 15 in pH 4 buffer solution.	160

Chapter 1

Introduction

1. Introduction

This thesis is on the electrochemical and electrocatalytic behaviour of titanium, manganese and cobalt phthalocyanines

1.1 Electrocatalysis

There are a number of reactions that occur on the electrode surface through electron transfer between the substrate and the electrode. However, there are reactions that do not take place on the electrode surface, since they occur at potentials where the substrate under study is electro-inactive due to high activation energy [1].

In electrocatalysis a catalyst acts as an electron transfer mediator in order to reduce the overpotential or activation energy of an electrochemical reaction bringing it closer to the thermodynamic equilibrium potential [1,2]. This situation creates a thermodynamic paradox in that the catalyst which has a redox potential less than the substrate is able to induce an electrochemical reaction of the substrate whereas an electrode kept at the same potential cannot.

An electrocatalytic process is shown in Figure 1.1 where an electro-active species (O) on the electrode surface is reduced (R) and its interaction with a substrate (S) results in a product (P) being produced.

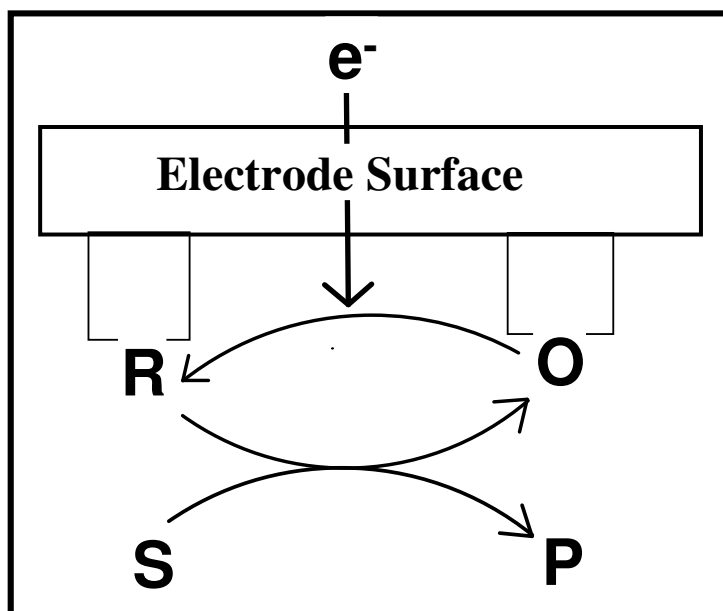


Figure 1. 1: A schematic illustration of electrocatalysis.

The electrode plays no significant role other than supplying the electronic conductivity and interface for charge-transfer for the mediator bound to the electrode surface [3]. It is possible for the electrode surface to have defects, this allows for the substrate to interact with the exposed sites. Electron transfer takes place between the modifier or electrode and the substrate, the rates at which such reactions occur are often limited by the diffusion of the substrates towards the electrode surface [4]. Fouling or passivation of the electrode from the products produced often occurs and it becomes difficult to regenerate the catalyst, hence current research includes finding or improving the stability of the catalysts.

The electrocatalyst must meet a number of fundamental requirements which are essential for good performance. These include high activity and maximum number of active sites on the electrode. The overall efficiency of the electrocatalyst is highly influenced by its

composition and on the subsequent catalyst regenerability of the surface to replenish catalytic sites. The electrocatalyst should have good electrical conductivity so as to minimize resistive losses in the catalyst layer and it is important that it is stable in the reaction environment. The catalyst should be inexpensive to manufacture at high volumes with good reproducibility [5,6]. Commercially available electrocatalysts include the Pt-Ru/Vulcan XC-72 from E-Tek which is used for the production of fuel cells [5]. In this work phthalocyanines are employed as electrocatalysts for biologically important reactions.

1.2 Phthalocyanines: An overview

1.2.1 Discovery, structure and general applications

Serendipity is defined as the accidental discovery of something fortunate while looking for something entirely different. This was the case with the discovery of phthalocyanines (Pcs) at the Grangemouth plant of Scottish Dyes Ltd in 1928 during the industrial preparation of phthalimide from phthalic anhydride where the glass-lined reaction vessel cracked, exposing the outer steel casing to the reaction resulting in the formation of a blue-green material. Due to academic interest the study of this compound was taken up by Professor J. T. Thorpe who gave it to Reginal Patrick Linstead (1902-1966) for investigation. Using a combination of elemental analysis, molecular mass determination and oxidative degradation, Linstead was able to come up with the correct structure for this material. He called this compound phthalocyanine because of its phthalic anhydride origin (phthalo) and deep blue color (cyanine) [7] and published a series of papers describing the synthesis and chemical properties of phthalocyanines.

Phthalocyanines are macrocyclic compounds that are closely related to the porphyrin ring system (Figure 1.2), the structural difference being the four isoindole subunits and nitrogen atoms at the four *meso* positions, hence phthalocyanines are often referred to as *tetra-benzotetraazaporphyrins* [8].

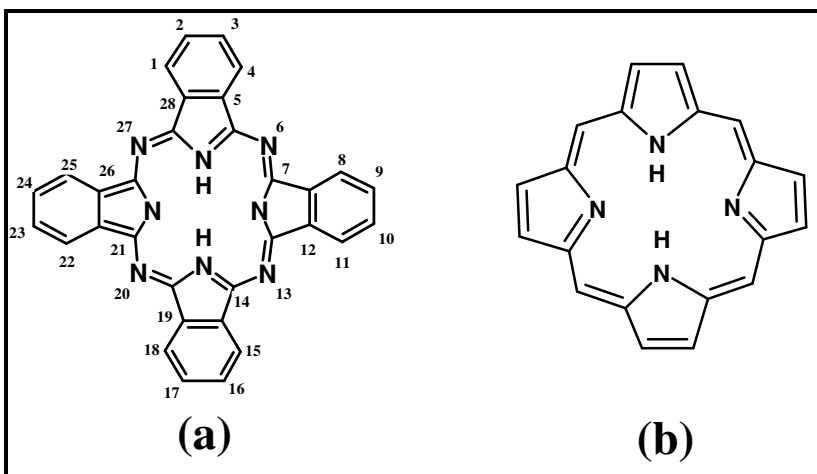


Figure 1. 2: Phthalocyanine structure (a) with possible substitution sites at benzo-positions numbered using the accepted notation. (b) The structure of a simple porphine (porphine).

Pcs are aromatic compounds owing to their planar conjugated display of 18 π -electrons. They are used in a number of applications because of their increased stability, architectural flexibility, diverse coordination properties and improved spectroscopic characteristics. Applications in fields such as chemical sensors [9-11], liquid crystals [12, 13], semiconductors [14], non-linear optics [15, 16], and photodynamic therapy (PDT) [17, 18], have given an increased importance of these macrocycles.

The Pc, although it can be oxidised or reduced to different oxidation states exists as a dianion (Pc^{2-}). The physicochemical properties of Pcs can be fine-tuned by manipulation of the structure such as inserting a metal at the centre of the Pc ring. A number of different metal ions can be placed in the centre cavity of the ring; however the choice of metal cation can strongly influence its physical properties. Some metal ions (Co^{2+} , Mn^{2+} , Zn^{2+}) are held tightly by the ring such that their removal would result in the destruction of the Pc. This is not the case for big metal ions such as Pb^{2+} that lie above the plane of the

ring resulting in the distortion of the geometry of the ring [19, 20]. A metal-free Pc (H_2Pc) has D_{2h} symmetry and this symmetry is increased to D_{4h} on a metallated Pc (MPc) for well fitting metal ions, but reduced to C_{4v} for metal ions that lie above the ring.

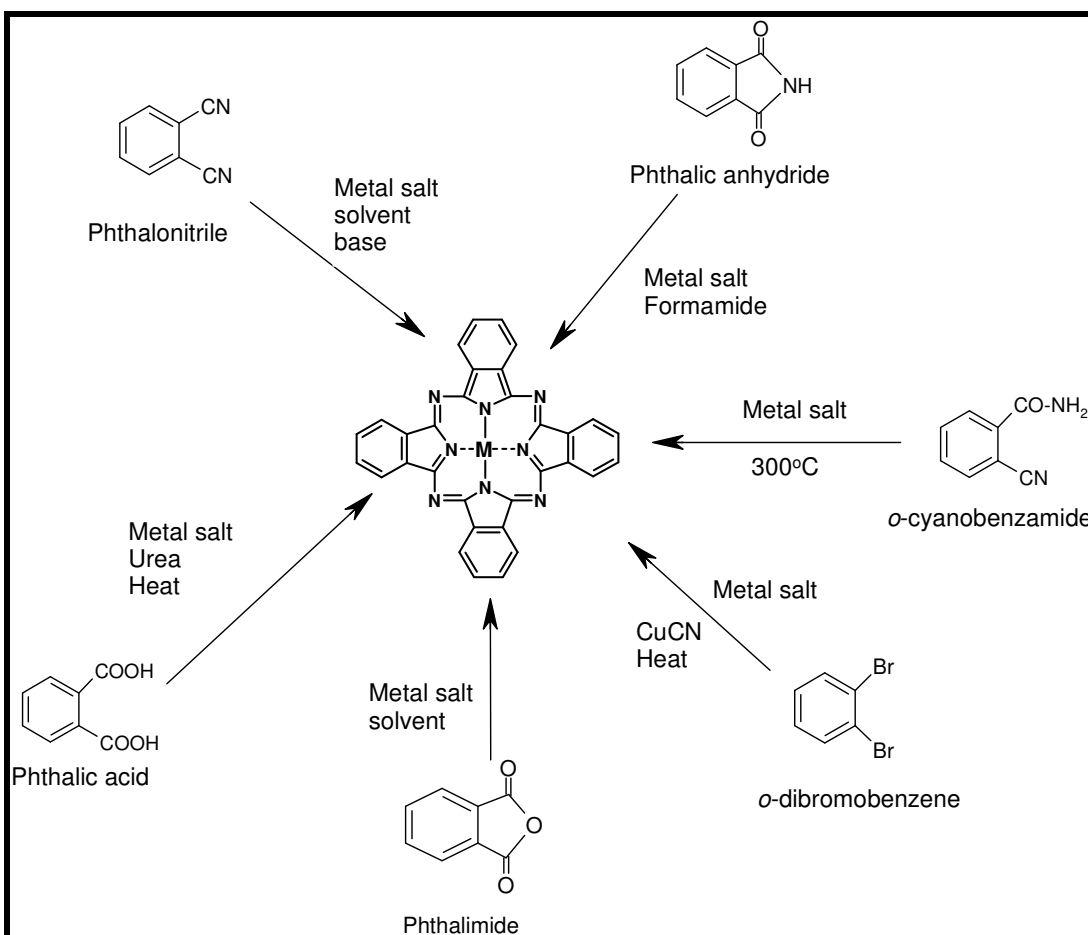
The flexible structure of a Pc ring allows for the incorporation of different substituents on the peripheral {(2,3), (9,10), (16,17) or (23,14)} or non-peripheral {(1, 4), (8,11), (15,18) or (22,25)} positions of the ring. Such structural manipulations greatly improve the solubility and decrease aggregation. Phthalocyanine aggregation is usually depicted as a coplanar association of rings progressing from monomer to dimer to higher order complexes, this occurs through the π - π interaction of Pc rings [21].

Another method of manipulating phthalocyanine structure is through axial ligation which is achieved by attaching axial ligands to the central ion of a MPc. This type of substitution highly reduces the intermolecular interactions (aggregation) enhancing solubility [21, 22].

Phthalocyanines are light absorbing compounds, particularly red light. The positions of the absorption bands in phthalocyanines, (particularly the Q band) are affected to a varying degree by the central metal, axial ligation, solvents, peripheral and non-peripheral substitution, aggregation and by extension of the conjugation [23]. Pcs that are highly red shifted have found applications in energy conversion and optical devices [24]. The red shift is more prominent with electron-donating substituents such $-NH_2$, $-OR$, $-SR$, etc [25].

1.2.2 The synthesis of phthalocyanines

A number of ortho-disubstituted benzene derivatives can act as Pc precursors, these include phthalonitrile, phthalic acid, phthalic anhydride, phthalimide, diiminoisoindoline, *o*-cyanobenzamide, *o*-dibromobenzene and other derivatives (Scheme 1.1). The phthalonitrile is the more popular choice for laboratory synthesis as it gives high yields of the Pc product, for mass production of Pc, the phthalic anhydride is used as it is relatively cheap [26].



Scheme 1. 1: Synthetic routes of MPcs from starting materials.

Unsubstituted metal-free Pcs can be conveniently prepared by the Linstead method [27] from a phthalonitrile in a refluxing alcohol solution containing lithium, sodium or magnesium alkoxides. This results in an MPc that is demetallated by the addition of a dilute acid affording the H₂Pc. Other methods include the use of a base (ammonia, or 1,8-diazabicyclo[5.4.0]undec-7-ene) or organic reducing reagents that will create the ideal environment for the cyclotetramerisation of the phthalonitrile [28]. Lastly the use of microwave irradiation offers a quick and solvent free alternative [29].

Metallated Pcs can be prepared from metal-free Pc through the addition of a metal salt in a reaction. The limitation of this method is that big metals are unable to fit in the cavity of the H₂Pc therefore the metal salt is added in the refluxing solution of a phthalonitrile precursor.

Unsubstituted H₂Pc and MPc show poor solubility in most organic solvents due to strong π - π interactions which causes aggregation of the Pcs. This has led to synthetic methods that allow for the substitution of benzo-substituents on the α (peripheral) and β (non-peripheral) positions of the Pc ring (Figure 1.2). The steric hindrance caused by substitution encourages Pc dissolution in a solvent and this greatly improves solubility. The importance of synthesizing substituted Pcs is the development of new derivatives that have improved chemical properties.

Phthalocyanines tetra-substituted at the peripheral positions have been extensively synthesized and studied more than the non-peripheral derivatives despite the fact that substitution at the non-peripheral positions reduces phthalocyanine aggregation

tendencies more than substitution at the less sterically crowded peripheral position. For that reason this thesis will focus on non-peripherally tetra-substituted phthalocyanines.

Substituted Pcs are generally synthesized from phthalonitrile precursors that contain the desired substituent. Octa-substituted Pcs are formed from disubstituted precursors and tetra-substituted Pcs are formed from monosubstituted precursors. The latter leads to constitutional isomers which form as a result of the symmetry involved in the condensation reaction for phthalocyanine synthesis. These isomers, shown in Figure 1.3 can be isolated using high performance liquid chromatography (HPLC) [30].

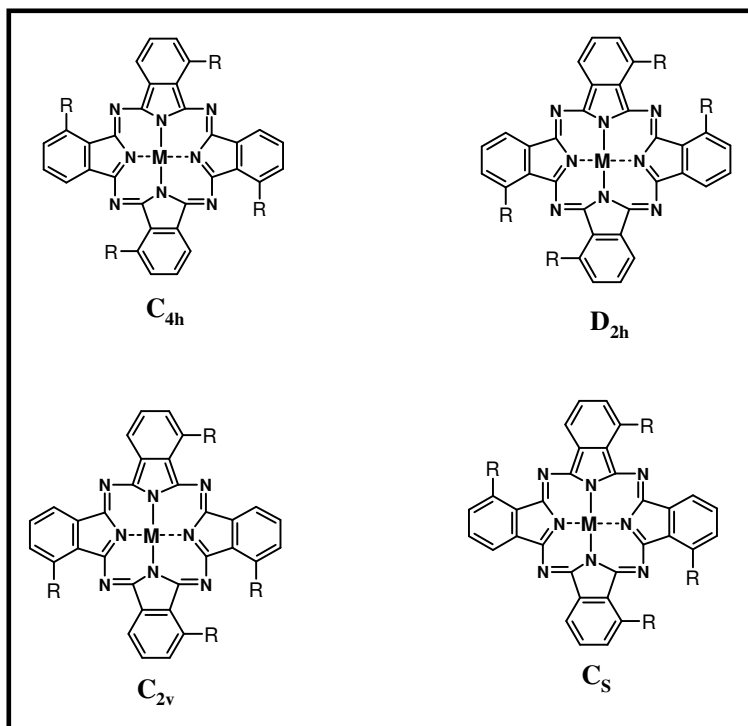


Figure 1. 3: Constitutional isomers of non-peripherally substituted MPcs. R represent a substituent.

The crucial part in Pc synthesis is the purification for the removal of unreacted starting material or by-products, hence suitable purification methods are often coupled for Pc synthesis. Conventional purification methods such as column chromatography can be applied to phthalocyanines that are soluble in organic solvents, though care must be taken as aggregation of the Pcs can occur and this could hamper the purification process. Gel permeation chromatography has been shown to be one of the best techniques as the phthalocyanine is eluted first. Phthalocyanines that are insoluble in common volatile organic solvents (such as unsubstituted MPcs) are typically difficult to purify. Their purification method often includes sublimation at temperatures up to 600°C *in vacuo*, resulting in ultra-pure materials [31].

1.2.3 Electronic structure and spectroscopy of phthalocyanines

There are various methods used for the characterization of Pcs. Such methods include infra-red spectroscopy (IR), elemental analysis, nuclear magnetic resonance (NMR) spectroscopy, matrix-assisted laser desorption ionisation spectroscopy (MALDI) and many others. Of all these methods ultraviolet/visible spectroscopy (UV/Vis) is the most popular form of Pc characterization. The method gives an indication of what is known as the Q-band that is of particular importance. The Q-band is a characteristic absorption peak for phthalocyanines and its position is largely influenced by the central metal and the substituents on the Pc ring.

The spectral properties of Pcs arise due to the 18- π conjugated ring system as shown in Figure 1.4 [32]. It is important to understand the basics or the origin of phthalocyanine spectra to fully appreciate phthalocyanine spectral properties.

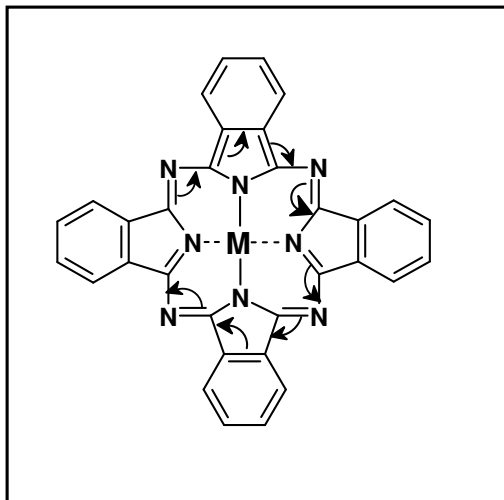


Figure 1. 4: Molecular structure of an MPc showing the path of the 18- π conjugated system used.

The UV-Vis spectrum of phthalocyanines is understood through the use of Gouterman's four-orbital model, a model based on a linear combination of atomic orbitals (LCAO). The model interprets the spectrum in terms of the transitions between the two highest occupied molecular orbitals (HOMOs) which are the a_{1u} (π) followed by the a_{2u} (π) to the lowest unoccupied molecular orbital (LUMO) which is the doubly degenerate e_g (π^*) with b_{1u} (π^*) just above it [32, 33], Figure 1.5.

The Q band originates from the π - π^* electronic transition involving the a_{1u} and e_g orbitals. Phthalocyanines also have Soret or B bands which are blue shifted with respect to the Q-band. They originate from the π - π^* electronic transition involving the a_{2u} or b_{2u} and e_g orbitals as shown in Figure 1.5 [34]. There are other absorption bands of higher energy states which involve other orbitals of the π conjugated system, these bands are denoted as N, L, C, X1 and X2 bands.

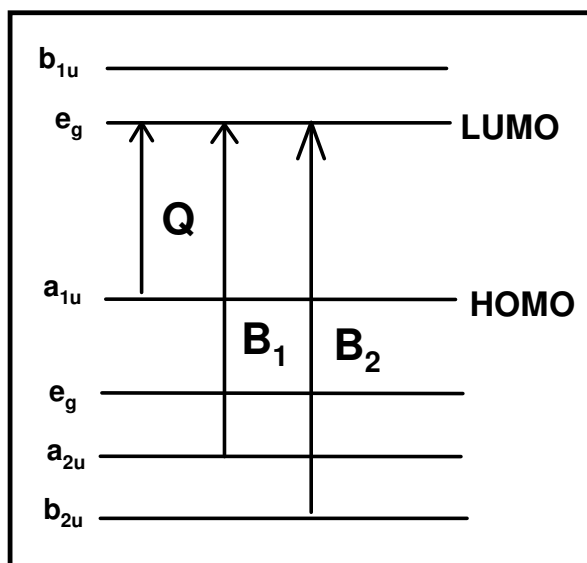


Figure 1. 5: Molecular orbital diagram of a phthalocyanine showing transitions that give rise to absorption bands.

The symmetry of the MPc is attributed to the degenerate e_g orbital, however the H₂Pc has a non-degenerate e_g orbital (e_{gx} and e_{gy}) resulting in a loss of symmetry. The consequence of this is seen in the UV/Vis spectra where the H₂Pc has two Q-bands and the MPc has one as shown in Figure 1.6. Also shown in the figure are vibronic bands caused by transitions from the a_{1u} (π) of the HOMO to vibronic bands of the e_g (π^*) of the LUMO. There also exists charge transfer bands which result in MPc when the d orbitals of the metal lie between the HOMO-LUMO energy gap. This arrangement allows for the electronic transitions either from the metal to the Pc ring (Metal to Ligand charge transfer) or vice versa (Ligand to Metal charge transfer). These bands are usually observed in the 550-400 nm range [23].

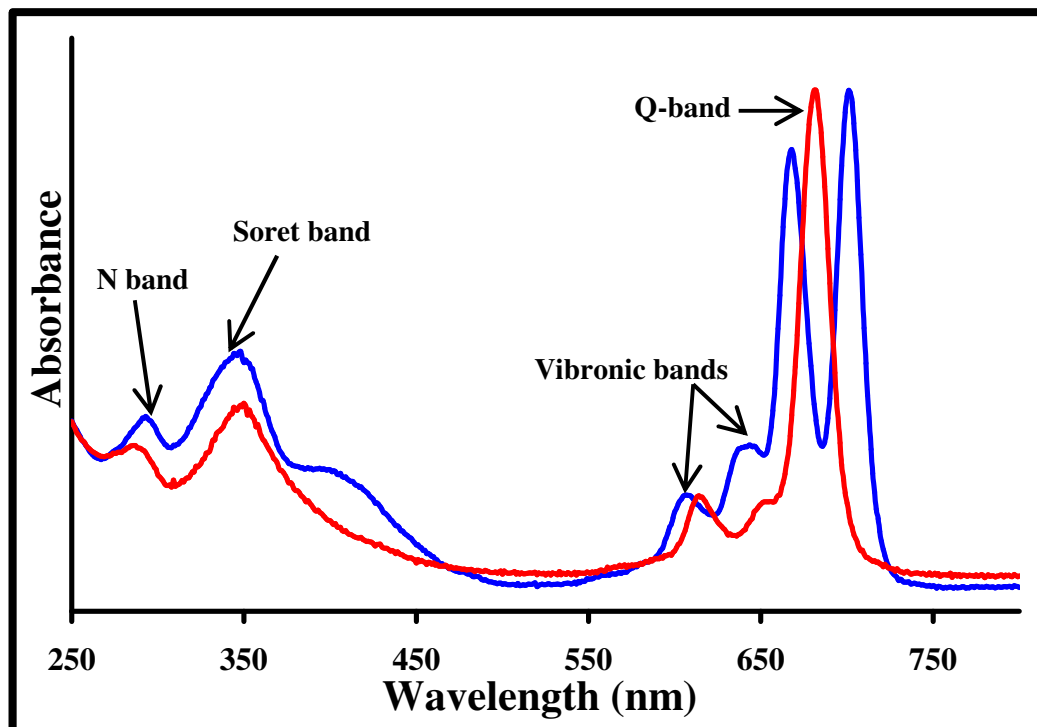


Figure 1. 6: Absorption spectra of metallated (red) and unmetallated (blue) phthalocyanine showing typical phthalocyanine absorption bands.

Substituted phthalocyanines show a shifted Q-band absorption relative to the unsubstituted phthalocyanine, the shift in absorption may be a blue (bathochromic) or red (hypsochromic) shift. Substitution at the non-peripheral (α) position has been shown to cause a red shift compared to peripheral (β) substitution. This red shift is caused by the increased electron density of the ring resulting in a reduction of the phthalocyanine HOMO-LUMO energy gap. Electron donating groups have been shown to enhance this red shift as compared to electron withdrawing substituents. ‘Special’ metal ions such as Mn^{2+} , Ti^{4+} and V^{4+} have also shown to enhance the red shift [34-36].

1.2.4 The electrochemistry of phthalocyanines

Sulfonated phthalocyanines were the first to be studied by electrochemistry because of their solubility in common organic solvents. It was through the development of phthalocyanine synthetic chemistry leading to substituted phthalocyanines soluble in organic media that the field of phthalocyanine electrochemistry grew. These substituted phthalocyanines showed modified redox properties that could potentially be fine tuned for the development of materials in various fields such as sensors, and modified electrodes [37].

The oxidation or reduction of phthalocyanines in solution is influenced by the Fermi level of the working electrode. The Fermi level corresponds to the energy of the highest occupied orbital. This level is not fixed and can be adjusted by the supply of electrical energy (voltage). Depending on the position of the Fermi level it may be thermodynamically feasible to oxidize or reduce phthalocyanine molecules in solution. If the HOMO of the Pc is at a higher energy level than the Fermi level of the electrode then oxidation of the Pc will take place and if the LUMO has a low energy level than the Fermi level then reduction of the Pc will occur (Figure 1.7).

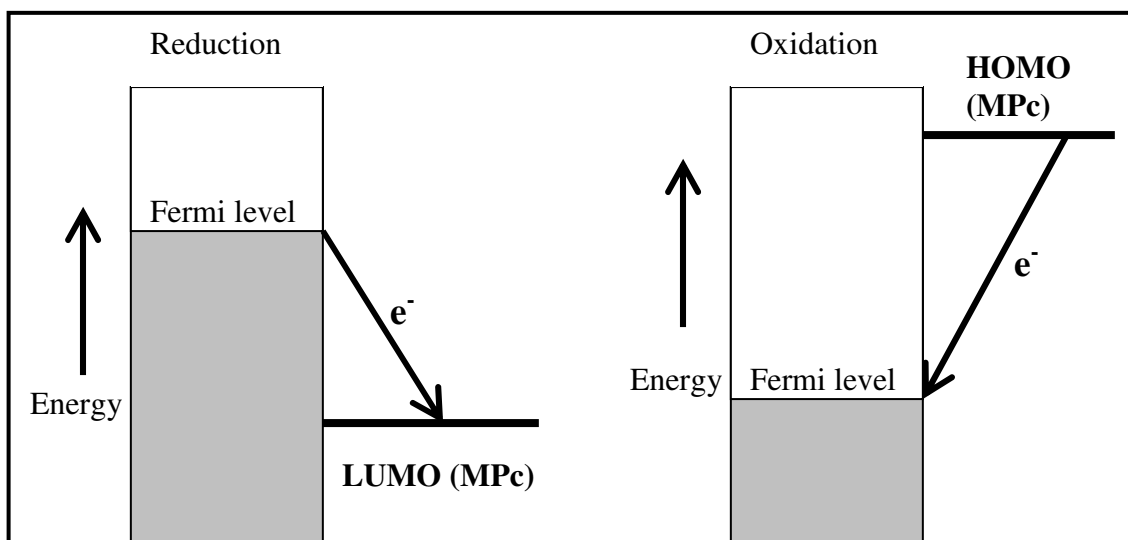


Figure 1. 7: A diagram showing the reduction and oxidation involving the MPc LUMO and HOMO.

The Pc dianion (Pc^{-2}) may be oxidized in steps to give Pc^{-1} and Pc^0 species. This oxidation occurs through the removal of two electrons from the a_{1u} (HOMO) orbital. Reduction of the Pc dianion occurs when electrons are added to the e_g (LUMO) orbital resulting in the formation of Pc^{-3} , Pc^{-4} , Pc^{-5} and Pc^{-6} species [33] shown in Figure 1.8.

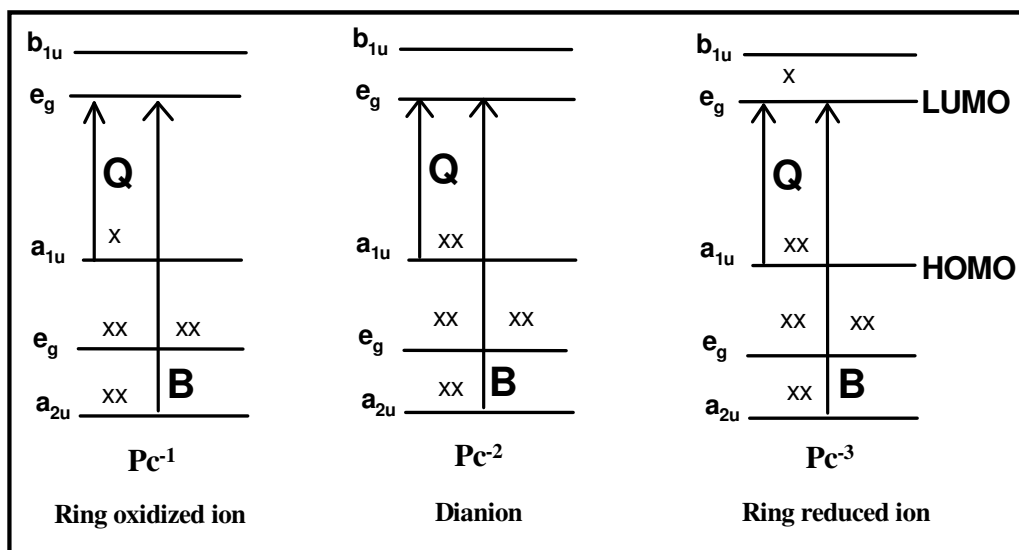


Figure 1. 8: Energy-level diagram showing the Pc dianion, ring reduced Pc and a ring oxidized Pc. The ‘x’ represents an electron [23].

These processes are typical for metal-free Pcs and Pcs with redox inactive metal ions (i.e. metals with fully occupied *d* orbitals). When metal *d* orbitals of electro-active metal ions lie between the HOMO-LUMO gap, MPcs experience oxidation or reduction on the metal and on the Pc ring with metal redox processes generally occurring between the first ring redox processes. MPc redox processes can be identified using spectroelectrochemistry; a method that monitors electrochemical reactions using spectroscopy. Metal-based redox processes are characterized by a spectral shift of the Q-band whereas ring-based processes are characterized by a decrease in Q-band intensity accompanied by a simultaneous increase in intensity at the 500 – 600 nm region [38].

1.2.5 Electrocatalytic behaviour of metallophthalocyanines

The electrocatalytic activity of phthalocyanines mainly relies on the redox properties of the MPc hence tuning of phthalocyanine redox potentials by changing the metal,

substituents and axial ligand is a good strategy for optimizing their electrocatalytic activity.

1.2.5.1 Tuning of metallophthalocyanine redox potential

Phthalocyanine redox properties are highly influenced by the solvent, the nature and position of the substituents, the central metal and axial ligands [33]. MPcs are capable of coordinating to solvents and counterions, this binding highly influences the potential of the metal processes, for example the $\text{Fe}^{\text{III}}\text{Pc}^{-2}/\text{Fe}^{\text{II}}\text{Pc}^{-2}$ couple shifts positively with the nature of solvent in the sequence: dimethylformamide < dimethylsulfoxide < pyridine [33].

MPc metal redox potentials have been shown to be pH dependent when the Pcs have been attached on electrodes and cyclic voltammograms (CVs) are recorded in buffer solutions with varying pH. For example in acidic pH the $\text{Co}^{\text{II}}/\text{Co}^{\text{I}}$ couple shifts to more negative values and stabilizes in basic pH. The $\text{Co}^{\text{III}}/\text{Co}^{\text{II}}$ couple is stabilized in acidic media and shifts to less positive values in basic media. This observation has been attributed to the uptake of protons or hydroxides by the surface confined MPc species [39].

It has also been shown that the nature of the substituents greatly affects the metal redox potential, for instance the formal potential of the $\text{Co}^{\text{III}}\text{Pc}^{-2}/\text{Co}^{\text{II}}\text{Pc}^{-2}$ redox process shifts to less positive values with electron donating nature of substituents, such groups enhance the electron density of the metal making it easier to oxidize compared to the unsubstituted CoPc. Electron withdrawing substituents have the opposite effect; they decrease the

electron density of the metal making it easier to reduce and the formal potential is shifted to more positive values in comparison to the unsubstituted CoPc [40].

Many transition metal ions prefer a six-coordination and will bind to axial ligands or donor solvent if no ligand is present. This can have a major effect on the MPc redox activity because the redox chemistry of axially ligated MPc will be different from that of the same MPc with no axial ligand [41].

1.2.5.2 Mode of electrocatalysts

Metallophthalocyanines have extensive redox chemistry and when incorporated on electrode surfaces they are able to act as electron transfer mediators for several compounds. This lowers the activation energy. This is reflected in the lowering of the overpotential for a given reaction compared to the unmodified electrode. The effectiveness of MPcs containing transition metals as catalysts lies in the fact that they have unpaired *d* electrons and unfilled *d* orbitals that are available to form bonds with an analyte. The electrocatalytic activity is most often expressed as a function of the number of *d* electrons of the metal ion in the Pc ring [42].

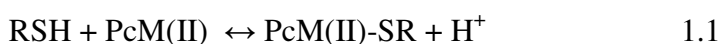
The nature of the central metal plays an important role in the electrocatalytic ability of metallophthalocyanines, this is because the catalytic reaction heavily relies on the MPc metal redox potential. Linear correlations have been found between phthalocyanine metal formal potential and the catalytic activity for the oxidation of analytes including thiols. It

is reported that in these correlations the rate constant of the catalytic reaction decreases with the driving force of the phthalocyanine i.e. the catalytic activity of oxidation reactions decreases with the oxidizing power of the catalyst and the reverse is observed for reduction reactions [43].

Often an MPc-analyte adduct is formed and this allows for the molecular orbitals of the MPc to interact with the molecular orbitals of the analyte, leading to a favorable electron transfer process [44].

Thiols (L-cysteine, 2-mercaptoethanol, glutathione, thionyl chloride) are known to be electrocatalysed by MPcs. The redox potential and electronic structure of the metal ion plays a crucial role in the electrocatalysis. For the electro-oxidation of cysteine the catalytic activity of MPcs varies in the order: Co>Fe>Mn>Ni>Cu. Co shows the best catalytic activity for this reaction. The high activity of the CoPc was attributed to the electronic coupling between the donor (thiol) and the acceptor (CoPc) [42, 43]. The interaction between the metal and the sulphur involves transfer of electron density from the sulphur p_z orbital to the d_z^2 and d_{xz} orbitals of the metals. It was observed that the energy of the MPc HOMO decreases almost linearly with the number of d electrons in the metal complex suggesting that a better match of orbital energies takes place between Co and the thiol compared to other metals [42].

The reported [40] reaction mechanism for the electrooxidation of L-cysteine in acidic media is as follows:





where RSH is a thiol and RSSR the disulphide.

Equation 1.1 is suggested since cysteine is known to coordinate to Co(II)Pc complex prior electron transfer [40]. Equations 1.2 and 1.3 are suggested since the oxidation of cysteine occurs in the stability range of $\text{Co}^{\text{III}}\text{Pc}^{-2}$ and hence the $\text{Co}^{\text{III}}\text{Pc}^{-2}/\text{Co}^{\text{II}}\text{Pc}^{-2}$ process is involved in the electrocatalytic process. Cysteine undergoes one electron oxidation to give cystine (equation 1.4). This mechanism is consistent with the electrooxidation of other thiols [42]. Cobalt and iron phthalocyanines have been commonly used as electrocatalysts because of their good catalytic abilities. However other metals such as Mn and Cr have been reported to have good catalytic ability [45, 46].

CoPc, MnPc and TiPc derivatives will be employed for nitrite and L-cysteine catalysis in this thesis. There are a wide variety of analytes, especially thiols that have been detected on CoPc [47]. The use of non-peripherally substituted CoPc in catalysis has not been fully explored. Hence in this work non-peripherally substituted CoPcs are employed and the types of electrodes used (Au disk, fiber, ultramicroelectrode) is novel.

TiPc complexes have not received much attention as electrocatalysts, while studies on MnPc are still limited. Thus Table 1.1 summarizes the use of TiPc [48, 49] and MnPc [50-53] as catalysts. Table 1.1 shows that TiPc complexes used in catalysis are limited and for both TiPc and MnPc the use of non-peripherally substituted Pcs is not known for catalysis hence this thesis will focus on non-peripherally substituted phthalocyanines.

Table 1. 1: Selected electrochemical data for the electro-oxidation of nitrite and L-cysteine using selected Ti and Mn phthalocyanine complexes.

MPc	Electrode	Mode of modification	Analyte	Ep/V vs. (Ag AgCl)	Medium	Reference
Ti(β)TAPc	GCE	Electro-Polymerization	Nitrite	0.60	pH 7.4	[48]
Ti(β)TTPhPc	GCE	Electro-deposition	Nitrite	0.64	pH 7.4	[49]
Ti(β)TBTPc	GCE	Electro-deposition	Nitrite	0.59	pH 7.4	[49]
Mn(β)TBM Pc	Au	SAM	Nitrite	0.76	pH 7.4	[50]
Mn(β)TSPc	OPG	Dip dry	Cysteine	0.19	0.2 M NaOH	[51]
Mn(β)TCA Pc	Au-ME	SAM	Cysteine	0.47	pH 4	[52]
MnPc	Au-MPy	SAM	Cysteine	0.20	pH 4	[53]

Abbreviations: TA = Tetraamino, TTPh = tetrathiophenyl, TBT= tetrabenzylthio, TBM = tetrabenzylmecarpto, TS = tetrasulphonated, TCA= tetracarboxy, TBM = tetrabenzylmecarpto, ME = 2-mecaptoethanol, MPy = 4-mecaptopyridine, SAM = self assembled monolayer.

As Table 1.1 shows, there are limited reports on the use of substituted alkylthio derivatized MPc as electrocatalysts. This may be due to the fact that alkylthio substituted MPc have lengthy synthetic routes which are often complicated. However simpler methods have been established [54]. The electron donating nature of alkylthio substituents would increase the electron density of the π -conjugated MPcs and non-peripheral substitution of such groups would greatly enhance this effect. This becomes a great advantage when the MPc is used as a catalyst in electro-oxidation reactions because the enhanced electron density would result in the metal ion being easier to oxidize hence overpotential lowering may be observed for oxidation reactions. This thesis aims to use non-peripherally substituted alkylthio derivatized CoPc, MnPc and TiPc for nitrite and L-cysteine electro-oxidation.

1.3 Modes of electrode modification for electrocatalysis

The electrode surface is a powerful device that is important in a number of applications. Electrochemical processes involve a variety of chemical and physical steps including electron transfer and mass transport [55]. A major aspect in electrochemical research is the control of electrochemical processes at the electrode/solution interface; this control greatly affects the field of electrocatalysis. The major problem with unmodified electrodes is their reduced analytical ability caused by fouling from unwanted precipitates/products and they show slow analyte electrochemical reaction rates where an overpotential has to be applied for the reaction to occur [56]. This is the cause for the pursuit of deliberately modified electrode surfaces as a means of controlling its processes. Through this process it is hoped that the electrode surface will take on the

physicochemical properties of the modifier making it more sensitive with desirable properties [56, 57]. The preparation of these chemically modified electrodes (CMEs) has been extremely popular. This is due to the structured and molecularly designed electrode surfaces that could give rise to better reactivity and novel devices for electrocatalytic purposes [58].

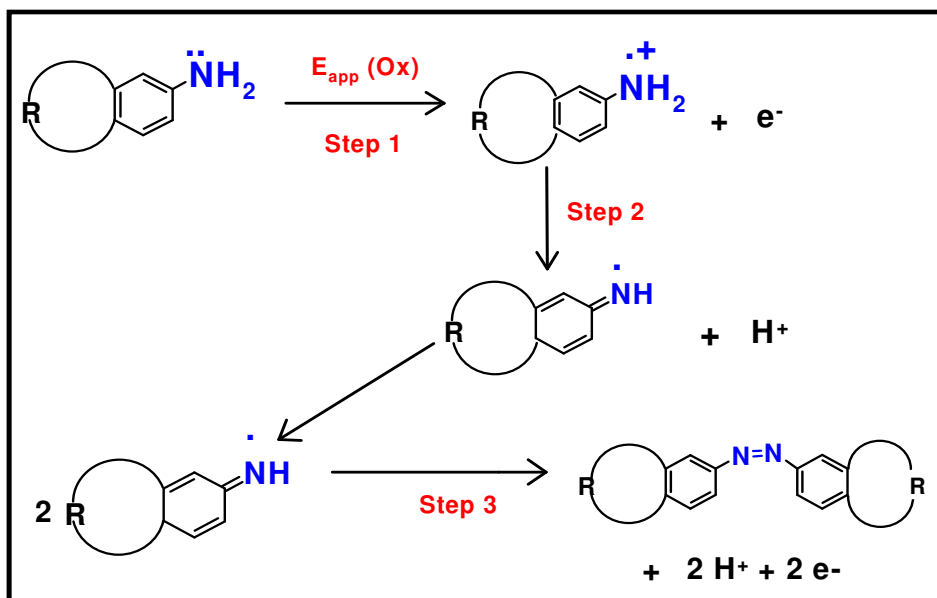
In this work a glassy carbon electrode (GCE) and gold (solid disk, ultramicro and textile) electrode was used as chemically modified electrodes for electrocatalysis hence their modification modes are discussed.

There are numerous methods of electrode modification, these methods are limited by the electrode material and the modifier (Pc) used. Such methods include spin coating [59], drop-dry/ dip coating adsorption [60], electro-deposition [46], electro-polymerization [46] and self-assembly [61].

1.3.1 Electropolymerization

In this work the GCE was modified with amino derivatized MPcs using electropolymerization. This method involves the repetitive oxidative or reductive cycling of a monomer to an activated form that will polymerize to form a polymer film on the electrode surface; less pinholes are formed by this process since polymerization at exposed (pinhole) sites on the electrode surface is accentuated. It is important for the polymer film to be redox active otherwise passivation will occur and further film growth will be prevented [56]. Cyclic voltammetry is used for electropolymerization in such a way that the potential window for the experiment is within the oxidation or reduction

potential of the polymerizable moiety of the monomer. Scheme 1.2 shows the polymerization process upon the oxidation of the amino group of the monomer.



Scheme 1. 2: Schematic diagram of electro-polymerization of an amino derivatized phthalocyanine monomer, where R represents the rest of the Pc molecule [62].

For tetraaminophthalocyanines electropolymerization occurs in three steps, the first step is the oxidation of the amino substituent followed by the loss of a proton from the radical cation (step 2) and lastly the N-N oxidative coupling of the phthalocyanine monomers occurs (step 3). This process is sustained by repeating step 1 via the NH_2 groups remaining on the R residue [62].

Electropolymerization is characterized by the first scan being different from the consecutive scans; there is usually an increase in peak currents, formation of new peaks and a shifting of peak potentials as shown on Figure 1.9.

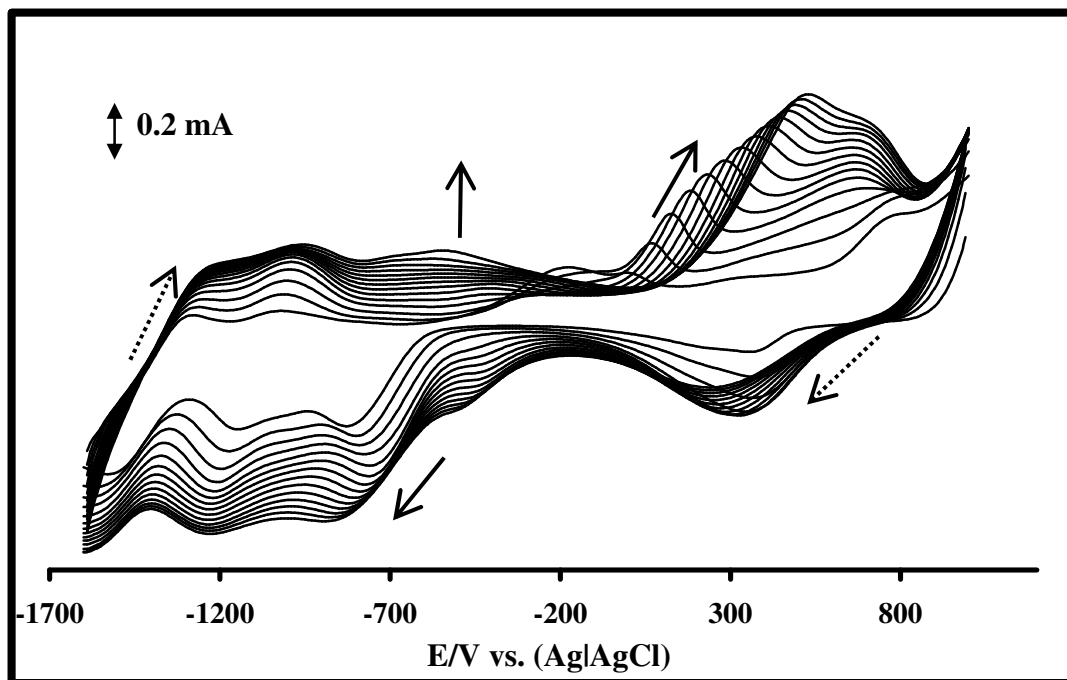


Figure 1. 9: Repeated cyclic voltammograms showing the electropolymerization of nickel tetraaminophthalocyanine on a glassy carbon electrode (unpublished work). Scan rate = 100mVs^{-1} .

1.3.2 Self assembled monolayers (SAMs)

Self assembled monolayers (SAMs) have gained a lot of interest because of the tremendous amount of effort that has focused on the construction and characterization of ordered, non-polymeric electrode films. SAMs are used as electrocatalysts due to their reproducibility. SAM formation depends on unique chemical interactions between a substrate and organic molecules, therefore specific pairs of a substrate and precursor are necessary. Sulfur has a distinct affinity for gold; hence thio derivatized phthalocyanines will chemisorb on gold surfaces and form an ordered monolayer assembly [63].

Phthalocyanines can act as structural building blocks in monolayer films and their redox properties indicate that such films can have interesting electrocatalytic properties.

1.3.2.1 Types of SAMs

Three methods for forming MPc-SAMs are known; the first approach involves the use of peripherally or non-peripherally substituted MPc complexes containing sulfur substituents [59]. The second strategy is to introduce a sulfur containing axial ligand on the metal of the Pc [53] and the third strategy involves the use of a coupling reaction between the MPc with functional groups complimentary to the terminal functional group of a pre-formed SAM [64]. These MPcs attach to the gold via the sulfur groups to form MPc-SAMs. The three strategies lead to three types of MPc SAM orientation on the gold electrode surface; the umbrella, octopus and vertical orientations (Figure 1.10).

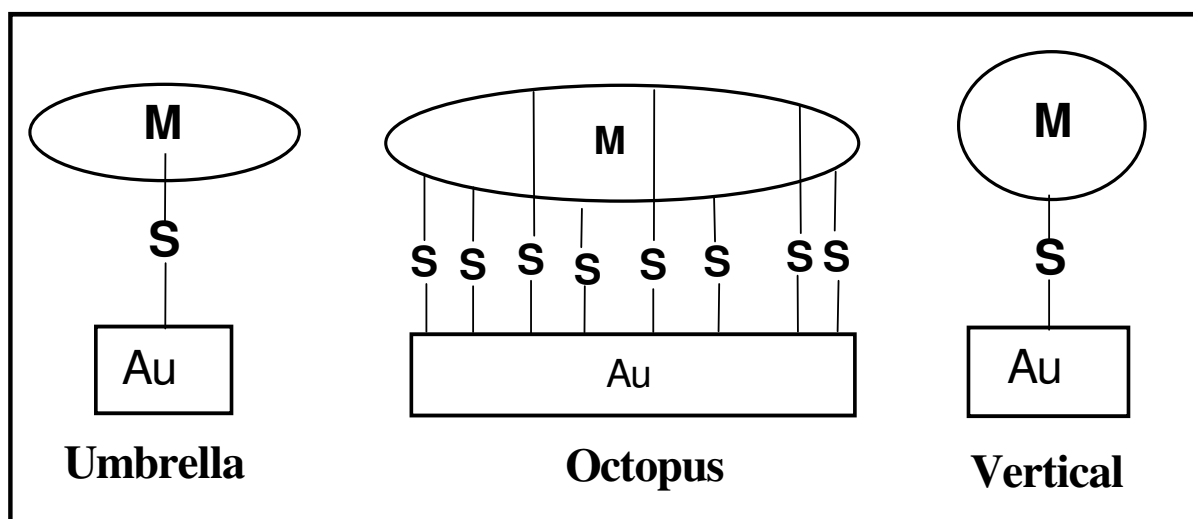


Figure 1. 10: Diagram showing the different orientations of MPc-SAMs on gold electrodes [63].

These orientations are governed by the number and position of thio substituents on the Pc molecule. The umbrella orientation is obtained when the SAM is formed through the axial ligand method [53]. The octopus orientation forms when the thio ring substituents bond to the gold in such a way that the octasubstituted MPc lies flat on the electrode surface [65] and a SAM vertical orientation is formed on gold electrodes when the pre-formed SAM method is employed [64] or when a Pc with a single thio substituent is in contact with the surface [66].

Defects or pinholes on the SAMs are influenced by the adsorption time, the longer the adsorption times the more well-ordered and defect-free the SAM becomes [63].

1.3.2.2 Electrodes used

In this work, three gold electrodes with different geometries were used for phthalocyanine SAM formation. The electrodes are: a gold disk, gold ultramicroelectrode (cylinder) and a gold coated fiber electrode. MPc-SAMs have been extensively studied on gold macroelectrode and not as intensely on ultramicroelectrodes. Using a coated textile fiber is a new way of making a gold electrode from textiles. Textiles have gained a lot of interest for use as electrotexiles due to their potential use for micro-filtration, medical and military uses [67-69]. Electrotexiles are fibers, yarns or garments that can conduct an electrical current. In this work MPc-SAMs were formed for the first time on gold coated fibers.

1.3.2.2.1 Textile electrodes

Textiles have over the century been used with great utility from the fashion industry to technical textiles. Presently there is a shift towards the incorporation of electronic systems into textile structures or coating fibers/fabrics with conductive polymers. Such fibers are classified as electrotiles and they display sensing capacities for external stimuli [67]. Researchers at the Georgia Institute of Technology introduced the Smart Shirt, a wearable platform for monitoring human vital signs where information from the electrically conducting fibers is sent to a transmitter at the base of the shirt where it is stored on a memory chip or sent to a doctor via a wireless network like Bluetooth [68]. This research has led to the development of wearable biomonitors systems [69].

There are physical factors that would greatly affect the sensing ability of a textile sensor; these include corrosion of the textile which would increase the resistance resulting in the sensors accuracy being significantly reduced. Another factor is fiber breakage which would also increase resistance, this breakage often occurs during laundry and this poses a big problem for all kinds of conductive materials. Textile deformation is a major disadvantage because it negatively affects sensor function [70].

The textile structure can be carefully designed in such a way that it allows for advanced sensing abilities, such textiles are referred to as smart or intelligent textiles. The basic mechanism is related to conductivity and current hence electrochemistry is an important subject for the development of electrochemically based textile sensors. It is important that the measuring conditions and the correct electrode and textile configuration (fiber diameter) are employed for the desired analysis [67].

An example of a textile electrode is shown in Figure 1.11 where a knitted fabric containing insulated conductive tracks connected with sensors and electrodes have been used to make the cloth. External stimuli or movement activity result in piezoresistive sensor signals that are transmitted to the electrode comprised of stain-less steel wire twisted around a textile yarn; this improves the electrical signal quality [70].

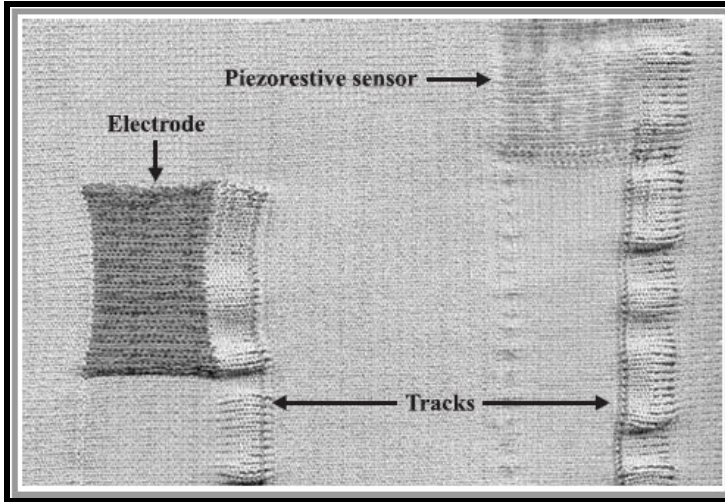


Figure 1. 11: Textile based electrode [70].

In this work para-aramide fiber was chemically deposited with conductive material (poly-pyrrole, copper and gold consecutively) such that the surface of the fiber became conductive [71]. Poly-pyrrole (Ppy) is a widely researched conducting polymer owing to its excellent electrical conductivity, good environmental stability in ambient conditions and it has few toxicological problems. However Ppy has mechanical problems as its fragility limits its practical uses hence Ppy is often blended with another polymer forming copolymers to improve the mechanical properties [72]. The gold coated fiber is a good sensing material because of its inertness and excellent electrical conductivity [71].

Textile electrodes have gained a lot of attention in health care monitoring and diagnostic system and hardly any attention in the field of electrocatalysis hence this work focuses on their use as potential sensors for biologically important compounds.

1.3.2.2.2 Ultramicroelectrodes (UMEs)

Electrodes are classified according to their sizes; ultramicroelectrodes have been defined as electrodes of any shape having at least one dimension called the critical dimension smaller than 25 μm . This critical dimension can be the width of a band or the radius of a disk. Electrodes with critical dimensions smaller than 10 nm are referred to as nanodes [73].

Electrochemical responses at UMEs differ significantly from those seen at macroelectrodes, this is based on the different mechanism for the transport of electro-active species toward the electrode surface. Macroelectrodes experience linear diffusion of species and for UMEs the main form of transport is spherical diffusion. This deviation leads to the steady state response often observed at UMEs and electrochemical data that is affected by the electrode shape as it affects diffusional fluxes [74]. Common ultramicroelectrode shapes are shown in Figure 1.12.

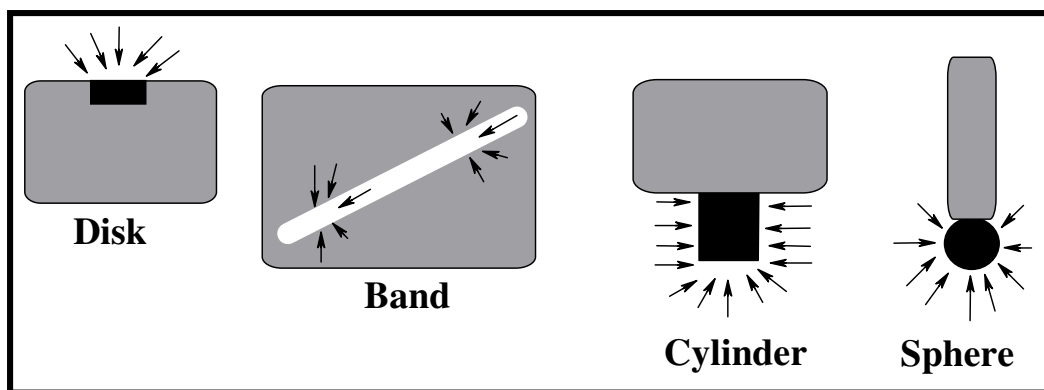


Figure 1. 12: Common ultramicroelectrode geometries with their associated diffusion fields.

Steady state at UMEs is reached shortly after the beginning of the experiment, thus if the time scale is long enough current-potential curves under cyclic voltammetry conditions show a plateau type shape whereas in faster experiments a peak still develops because under these conditions, the electrode behaves like a macroelectrode as mass transport is dominated by diffusion [75].

Large current densities due to spherical diffusion are observed at UMEs, this is very important for analytical purposes as it improves sensitivity and detection limits. The small size results in a decreased ohmic drop during voltammetric experiments; this characteristic has been greatly exploited for performing electrochemical experiments under conditions in which no or small concentration of supporting electrolyte is added, thus UMEs allow for the use of non-polar solvents (hexane, toluene etc) that cannot be used in convectional voltammertic experiments [74, 75].

The small electrode area reduces the double-layer capacity at the electrode surface as well as current outputs, this allows for experiments to be performed at high scan rates.

Ultrafast electrochemical techniques can provide kinetic information of redox processes that occur at micro or nanosecond timescales [76, 77].

Though they have many advantages, UMEs are tedious to fabricate and maintain.

In this work phthalocyanine self-assembled monolayers were formed on a gold cylinder ultramicroelectrode, this MPC-SAM modified UME was used for electrocatalysis.

1.3.3 Characterization of modified electrodes

Chemically modified electrodes (CMEs) are characterized in order to confirm the existence, orientation and coverage of the modifier on the electrode surface. There are a number of instrumental methods that are used for the analysis of CMEs and they are divided into two groups: *ex situ* and *in situ* methods. *In situ* methods are concerned with the analysis of the modified electrode while the electrode is immersed in an electrochemical solution with an electrochemical reaction occurring on the electrode surface. Such methods include electrochemical methods and quartz crystal microbalance. For *ex situ* instrumental methods the electrode has to be removed from the electrolytic solution for analysis, such methods include FT-Raman spectroscopy, atomic force microscopy and X-ray photo electron spectroscopy [78].

Cyclic voltammetry is a powerful tool that can be used to characterize modified electrodes. It can be used to determine the amount of surface confined species on a modified electrode surface. The presence of an MPC redox peak(s) would confirm the existence of this modifier on the electrode surface as well as the success of the modification process. From the CV of the MPC modified electrode, the area under a peak

(owing to the MPc) can be integrated to find the surface coverage of the MPc (Γ_{MPc}) on the electrode surface using equation 1.5:

$$\Gamma_{\text{MPc}} = \frac{Q}{nFA} \quad 1.5$$

where Q is the background corrected electric charge under the peak, n is the number of electrons transferred, F is the Faraday constant (96485 C/mol) and A is the surface area of the electrode. Another method involves recording CVs of the surface confined MPc, at different scan rates and using equation 1.6.

$$I_p = \frac{n^2 F^2 A v \Gamma_{\text{MPc}}}{4RT} \quad 1.6$$

where I_p is peak current, n is the number of electrons transferred, F is Faraday's constant, v is the scan rate, R is the gas constant and T is the temperature. It has been reported that for a Pc molecule lying flat on the surface, the monolayer coverage is approximately 1×10^{-10} mol/cm² [79].

A gold surface well covered with a self-assembled monolayer should block Faradic process that would easily occur at the bare gold surface. Such processes include the blockage of gold oxidation/reduction which occurs when oxygen is present in solution, the under-potential deposition (UPD) of copper and the $[\text{Fe}(\text{H}_2\text{O})_6]^{3+}/[\text{Fe}(\text{H}_2\text{O})_6]^{2+}$ redox process [63, 80]. In this work the gold electrode behavior in acid media (Na_2SO_4 solution in pH 4), basic media (KOH solution) and in $\text{Fe}(\text{NH}_4)(\text{SO}_4)_2$ was studied [65]. It is important to first characterize the unmodified gold surface, to determine the extent of occurrence for these Faradaic processes in order to compare them to the SAM modified electrode responses.

The ion blocking/barrier factor (Γ_{ibf}) may be calculated using equation 1.7 to give an indication of the solvent or ion permeability of the SAMs. The ideal value of $\Gamma_{ibf} = 1$, indicates the SAMs ability to block ions or solvent from penetrating the surface of the electrode [81].

$$\Gamma_{ibf} = 1 - \left(\frac{Q_{SAM}}{Q_{Bare}} \right) \quad 1.7$$

where Q_{SAM} and Q_{Bare} is the charge under the MPC-SAM and unmodified electrode peaks. This factor is determined using cyclic voltammograms that show the diminished Faradaic processes on the SAM modified electrode.

1.4 Overview of voltammetric methods employed

Electrochemical experiments are recorded using three electrodes (working, reference and counter) immersed in an electrolyte solution. The working electrode is the one where the reaction studied takes place; its potential is monitored and controlled with respect to the reference electrode which has a known potential. The counter electrode is added to complete the current circuit, this ensures that the reference electrode is protected from current flow that would cause its potential to vary [82, 83].

1.4.1 Cyclic voltammetry

Cyclic voltammetry together with linear sweep voltammetry were reported in 1938 and theoretically described by Randle and Sevcik in 1948 [82]. A number of important parameters can be obtained from the current-potential curve or cyclic voltammogram

produced. This method is used to determine redox couples of a given system as well as electrode reaction kinetics [84].

Figure 1.13 shows a CV where the potential is swept from the initial value (E_0), the current increases and as the species in solution become oxidized a concentration gradient is created. I_{pa} and E_{pa} indicate the highest current and potential values where all the reduced species have been oxidized. It is at this potential that the current will begin to drop if potential application is continued. The current drop is a result of the depleted reduced species. When E_f is reached the now oxidized species will get reduced to the original form on the reversal of the potential sweep [85] until E_0 is reached.

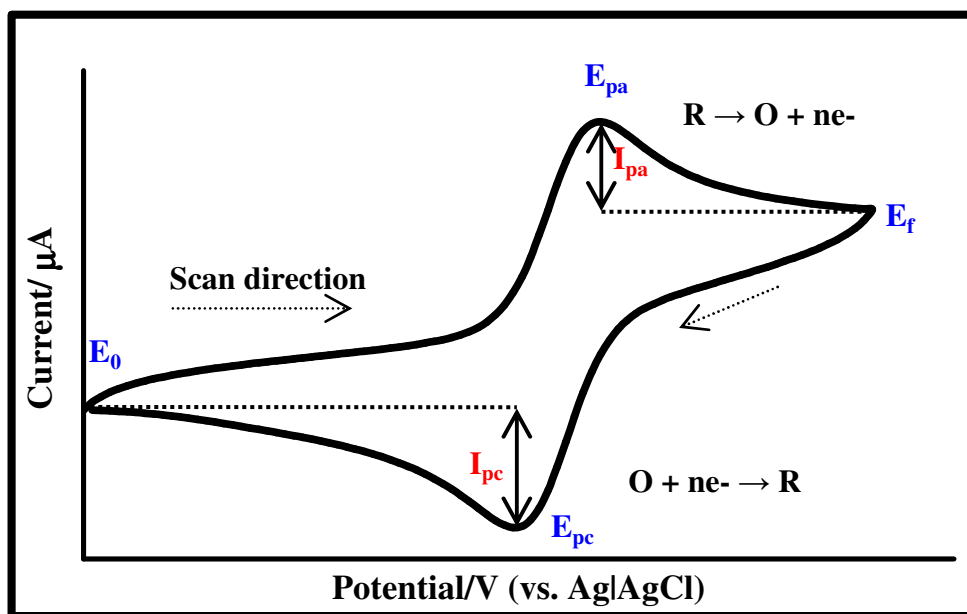


Figure 1. 13: A typical Cyclic voltammogram.

The current response is limited by the diffusion of redox active species to the electrode surface. The peak current is therefore proportional to the square root of the scan rate [73].

In cyclic voltammetric experiments mass transport (analyte movement from bulk to the

electrode) is governed by diffusion, this involves the movement of ions against a concentration gradient. This transportation mode is essential as the current response is related to the concentration of the redox active species under study. The dependence of peak current on the square root of the scan rate is indicative of diffusion control [77, 85].

1.4.2 Spectroelectrochemistry

Spectroelectrochemistry is a powerful technique that combines reaction-orientated electrochemistry with species-focused spectroscopy. A redox active compound is oxidized or reduced in a specially designed cell and the transformation of the compound is monitored *in situ* by spectroscopic techniques, consequently the mechanistic characterization of the redox process can be confirmed [78].

In phthalocyanine electrochemistry CVs are used to determine their redox processes, however this technique is often not suitable in identifying the nature of the redox process that is, if the redox process is metal or ring based hence spectroelectrochemistry is used as a tool to distinguish such processes.

An optically transparent thin layer electrode (OTTLE) is used in this study because of its appealing features which include high sensitivity [86]. When a potential is applied, the MPc redox couple is converted from one oxidation or reduction state to another and the spectral changes associated with the redox process are observed using a UV/Vis spectrometer. Metal based processes result in a shift of the Q-band wavelength and ring based processes are characterized by a decrease in Q-band intensity with a simultaneous increase in intensity in the 500-600 nm region [23, 38].

The number of electrons transferred during a redox process can be determined using equation 1.8

$$n = \frac{Q}{FVC} \quad 1.8$$

where Q is the amount of charge passed, V is the volume of the OTTLE cell, F is Faraday's constant and C is the concentration of the phthalocyanine solution.

1.4.3 Rotating disk voltammetry

Hydrodynamics is the study of liquids in motion, this method is used in electrochemistry in conjunction with voltammetry to study electrode reaction kinetics. Rotating disk electrode (RDE) involves the rotation of the working electrode around its axis in a liquid, the disk electrode is centered on the axis. As the disk rotates it drags the solution known as the hydrodynamic boundary layer (δ_H) at its surface at an angular velocity (ω) and the centrifugal force generated hurls the solution away from the center of the electrode. The surface of the disk is replenished by the solution through the laminar flow created (Figure 1.14). It is assumed that there are no special flow effects at the edge of the disk [73]. The reaction is monitored using linear sweep voltammetry.

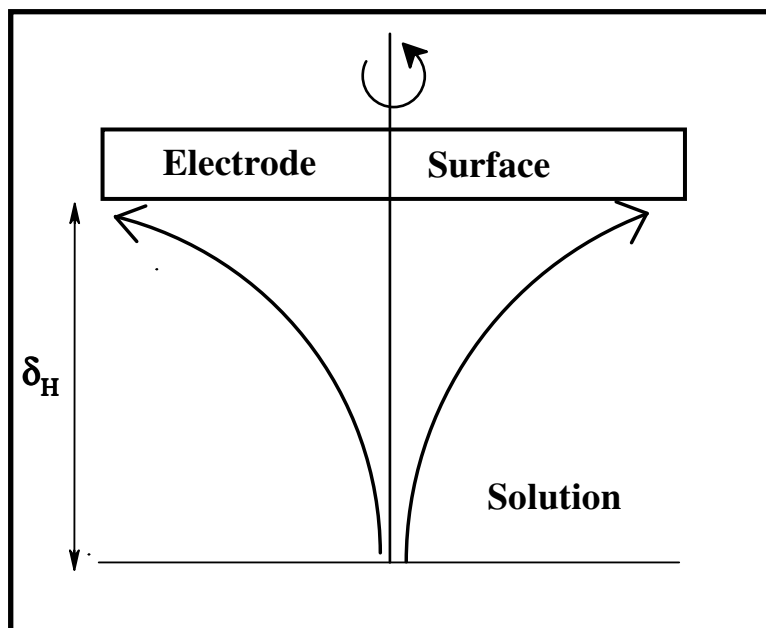


Figure 1. 14: Streamlines for a rotating disk electrode.

The electro-active species are transported to the electrode surface via two ways; the first mode is through convection as described above and the second mode is through diffusion.

The rotation speed of the electrode can be altered, thus at higher rotation speeds there is a large amount of electro-active species crossing a unit surface area per unit time.

A typical RDE voltammogram is shown in Figure 1.15, note that this curve is composed of three regions.

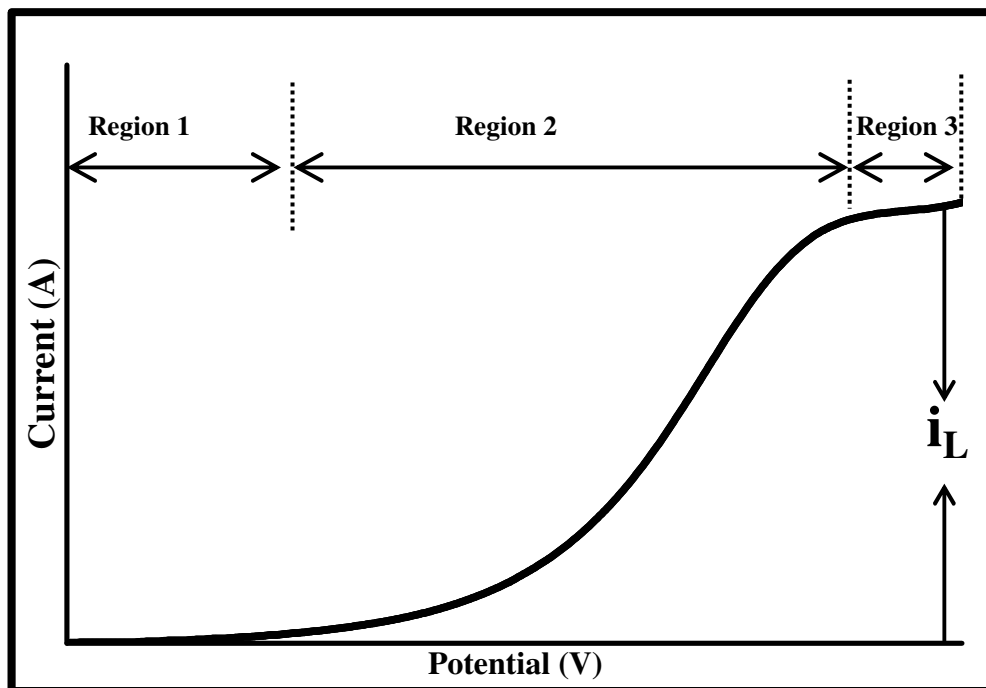


Figure 1. 15: Typical current-potential RDE voltammogram for an irreversible system.

Initially (Region 1) there is no significant current flow as the low potentials are not enough to drive the oxidation or reduction of the electro-active species in solution. At this stage the electrodic reactions are controlled by charge transfer and current densities are independent of rotation speed. In the intermediate potentials (Region 2) the current increases with potential due to electrochemical process occurring. At this stage the system enters a region of mixed control and the current density becomes gradually more dependent on convection. The third region is characterized by the leveling of the current which reaches a limiting value (i_L) independent of the potential, this occurs because at this point the electron transfer rates becomes so high that the rate determining step is the mass transport of the electro-active species to the electrode. This steady-state value results when all the electro-active species in solution have been completely oxidized or

reduced. The limiting current is given by the Levich equation (1.9) which takes into account both the convection and diffusion modes of transport of the electro-active species to the electrode surface.

$$i_L = 0.62nFAD^{2/3}\omega^{1/2}\nu^{-1/6}C \quad 1.9$$

where, ν is kinematic viscosity (cm^2/s), which is a ratio of solution's viscosity to its density, for pure water $\nu = 0.01 \text{ cm}^2/\text{s}$, ω is angular rotation rate of the electrode (radians/second); calculated from rotations per minute (f) using the relationship, $\omega = 2\pi f/60$, D is the diffusion coefficient of the analyte and the rest of the symbols have been described above. The total number of electrons transferred in the reaction (n) can be determined using the Levich equation and a linear plot of limiting current vs. $\omega^{1/2}$ indicates a diffusion controlled process [67].

RDE is a good system for measuring electrode kinetics of modified electrodes where mediated electron transfer to the substrate species in solution occurs through a surface immobilized redox couple. The uniform accessibility of the RDE ensures that the flux of substrate to the electrode is constant across the surface and the controlled hydrodynamics ensures a constant and reproducible substrate concentration at the surface of the electrocatalytic film [87].

The Tafel equation (1.10) describes the dependence of current on the overpotential [73].

$$\eta = a + b \log i \quad 1.10$$

where η is the overpotential, a is the exchange current density, i is current and b is the Tafel slope. For cathodic reactions the Tafel slope is given by equation 1.10a

$$b = -2.3 RT/\alpha_c nF \quad 1.10a$$

and for anodic reactions, the tafel slope is given by equation 1.10b [73, 82].

$$b = 2.3 RT/(1-\alpha_a)nF \quad 1.10b$$

Kinetic currents are used to plot the Tafel plot; a plot of logarithm of background corrected current ($\log i$) versus overpotential (η). The interpretation of the Tafel slope gives mechanistic information as the slope involves a combination of the transfer coefficient (α), the number of electrons transferred at the rate determining step (n) and it also identifies the rate determining step of the overall reaction [73, 88].

The transfer coefficient gives an indication of the symmetry of the activation barrier, values of α_a and α_c vary between 0 and 1. An α value of 0.5 means that the activated complex is exactly halfway between substrate and product on the reaction coordinate and a value of 1 indicate that the reaction activated transition state favors the product formation only. When $\alpha = 0.5$ the Tafel slope values becomes 120 mV/decade, this Tafel slope value implies that the rate determining step is an electrochemical step. Tafel slope values close to 60 mV/decade suggest that the rate determining step is a chemical step that is preceded by a fast one electron transfer process [73].

Tafel slope values as high as 300 mV/decade have been reported [89] and have been attributed to strong substrate-catalyst interactions.

1.5 Electrocatalysis of biologically important compounds by MPCs

1.5.1 An overview of nitrite catalysis

There are many factors that influence the flavor quality of meat products and such factors include the curing process. This process involves the addition of additives such as sodium nitrite which impart the characteristic properties of meat. Nitrite is formed through the biodegradation of nitrogenous organic matter such as nitrate and it is estimated that over 70% of pork is cured with nitrite. Not only does nitrite impart the characteristic pink color of cured meat it also reduces the oxidative nature of meat by preventing lipid oxidation. This results in increased shelf-life of the meat product. Nitrite has antimicrobial activity and is added to meat products in concentrations less than 150 ppm to prevent the outgrowth of *Clostridium botulinum* a bacteria that can cause food poisoning [90]. The danger of nitrite is that it is converted to carcinogenic compounds in the human digestive system called nitrosamines. This harmful impact on human health makes the detection of nitrite important [91].

The most popular method for nitrite detection in meat is the spectrophotometric method which proved to be inefficient as recovery was found to be less than 50% due to ascorbic acid interference. Other known methods for nitrite detection in meat include HPLC and ion chromatography. Electrochemistry gained much interest due to the development of ion selective electrodes that offered attractive features for nitrite detection leading to the development of nitrite selective electrodes [92].

Phthalocyanine based electrochemical sensors have been developed for nitrite oxidation because the direct hydrolysis of nitrite on bare electrodes is poor with high oxidation potentials [93]. Nitrite oxidation is often favored over reduction as nitrite reduction gives a number of products and the interference of oxygen is possible, while its oxidation is a straight forward reaction with nitrate being the product formed [94]. It has been shown that phthalocyanine modified glassy carbon, gold and vitreous carbon electrodes not only help reduce the overpotential of nitrite oxidation they also improve the electrode sensitivity [49,96]. Due to the rich redox nature of phthalocyanines, nitrite oxidation can be mediated by the central metal or by the ring.

Nitrite electro-oxidation on phthalocyanine modified electrodes is highly influenced by the nature of the central metal and substituents. Phthalocyanines that have been used for nitrite catalysis are shown on Table 1.2. Mainly CoPc [50,96], FePc [50, 60], CrPc [44], NiPc [97,98] and MnPc [50, 99] derivatives have been employed with limited reports on TiPc [49, 61]. All complexes employed have been peripherally substituted or unsubstituted. This work reports for the first time, non-peripherally substituted Ti, Co and Mn Pcs for nitrite detection.

Table 1. 2: Comparative peak potentials for nitrite oxidation in pH 7.4 buffer on MPc modified electrodes.

MPc	Electrode	Method of modification	E/V vs. (Ag AgCl)	Ref.
CoPc	VCE	Drop Dry	0.92	[96]
FePc	OPG	Drop-dry	0.8	[60]
TiTAPc	GCE	Electropolymerization	0.67	[49]
TiTBTPc	GCE	Electro-deposition	0.59	[49]
CrTAPc	GCE	Electropolymerization	0.8	[44]
NiTAPc	GCE	Electropolymerization	0.92	[97]
MnTBMPc	Au	SAM	0.76	[50]
MnTBTPc	Au	SAM	0.77	[99]
CoTBMPc	Au	SAM	0.75	[50]
FeTBMPc	Au	SAM	0.76	[50]
NiTBMPc	Au	Electropolymerization	0.83	[98]

Abbreviation: VCE = vitreous carbon electrode, OPG = ordinary pyrolytic graphite, GCE = glassy carbon electrode, Au = gold.

TA= tetraamino, TBT= tetrabenzylthio, TBM = tetrabenzylmecarpto, TTPh = tetrathiophenyl, TBM = tetrabenzylmecarpto, TBT = tetrabenzylthio.

1.5.2 An overview of L-cysteine catalysis

L-cysteine is a non-essential amino acid formed from serine and methionine in the body. It is one of the few amino acids that contain a sulfur group in its side chain. The nucleophilic nature of the thiol group allows L-cysteine to be easily de-protonated under physiological conditions, the resulting thiolate is highly reactive and often ionized thiolates form disulfides [100]. This reaction is important in protein synthesis and forms part of many cellular metabolism reaction [101]. The bioactivity of L-cysteine makes it a prospective antioxidant or free radical scavenger.

High levels of this amino acid results in diseases such as Alzheimer's and Parkinson's diseases [102, 103] as well as epileptic seizures [104] whereas low levels are linked to a high risk of cervical dysphasia [105]. Incorrect levels of the amino acid in the body may also cause an autoimmune deficiency syndrome [106]. The importance of this amino acid in biological systems makes its detection to be of paramount importance.

The electrochemical oxidation of L-cysteine at bare electrodes is kinetically slow and requires a large overpotential to occur [107, 108]. MPc modified electrodes have been used to reduce the overpotentials [109, 110] and Table 1.3 shows a selection of the catalytic responses of MPc modified electrodes for L-cysteine detection. This works aims at exploring and comparing the catalytic effect of GCE and Au electrodes modified with non-peripherally substituted MPcs with different central metals on electrodes. CoPc [40, 111-113], and FePc [51, 63, 113] have been extensively employed for L-cysteine catalysis, with limited reports on MoPc [109], RhPc, OsPc and RuPc [114] derivatives.

Even though cysteine oxidation on MPCs is known, the aim is to use MPCs that are non-peripherally substituted with thiols and gold fiber electrodes for the first time.

Table 1. 3: Comparative peak potentials for L-cysteine oxidation on MPc modified electrodes.

MPc	Electrode	Method of modification	Ep/V vs. (Ag AgCl)	Medium	Ref.
CoPc	GCE	Electro- deposition	0.58	pH 3.5	[111]
CoTNPc	GCE	Electro- deposition	0.65	pH 3.5	[40]
CoTETHpC	VCE	Adsorption	-0.11	pH 4	[112]
CoTETHpC	Au	SAM	0.39	pH 4	[113]
FeOHETPc	Au	SAM	0.38	pH 4	[113]
FeTCAPc	Au-ME	SAM	0.47	pH 4	[63]
FeTSPc	OPG	Drip dry	0.15	0.2M NaOH	[51]
MnTCAPc	Au-ME	SAM	0.47	pH 4	[52]
OMoPc	CPE		0.24	0.05 M H ₂ SO ₄	[109]
OMoTSPc	CPE		0.20	0.05 M H ₂ SO ₄	[109]
RhPc(Cl)(py)	GCE	Drop dry	1.05	pH 7.2	[114]
OsPc(py) ₂	GCE	Drop dry	0.94	pH 7.2	[114]
RuPc(py) ₂	GCE	Drop dry	1.10	pH 7.2	[114]

Abbreviations: TN = tetranitro, TETH = tetraethoxythiophene, OHET = octahydroxyethylthio,

TCA = tetracarboxy, TS = tetrasulphonated, Cl = chlorine, py = pyridine.

1.6 Summary of aims

1. To synthesize Co, Mn and Ti alpha substituted amino and alkylthio derivatized phthalocyanines shown in Figure 1.16
2. The characterization of these complexes will be carried out using UV/Vis. IR, NMR, elemental analysis, electrochemistry and spectroelectrochemistry.
3. These synthesized compounds will be used to modify GCE, Au, Au UMCE and gold coated fiber electrodes by electropolymerisation (GCE) and self assembly (Au electrodes).
4. The modified electrodes will be used for the electro-oxidation of nitrite and L-cysteine.
5. The modified electrode which shows the best performance in terms of overpotential reduction of nitrite and L-cysteine will be used as a sensor for the detection of nitrite in a meat sample and L-cysteine in a human urine sample.

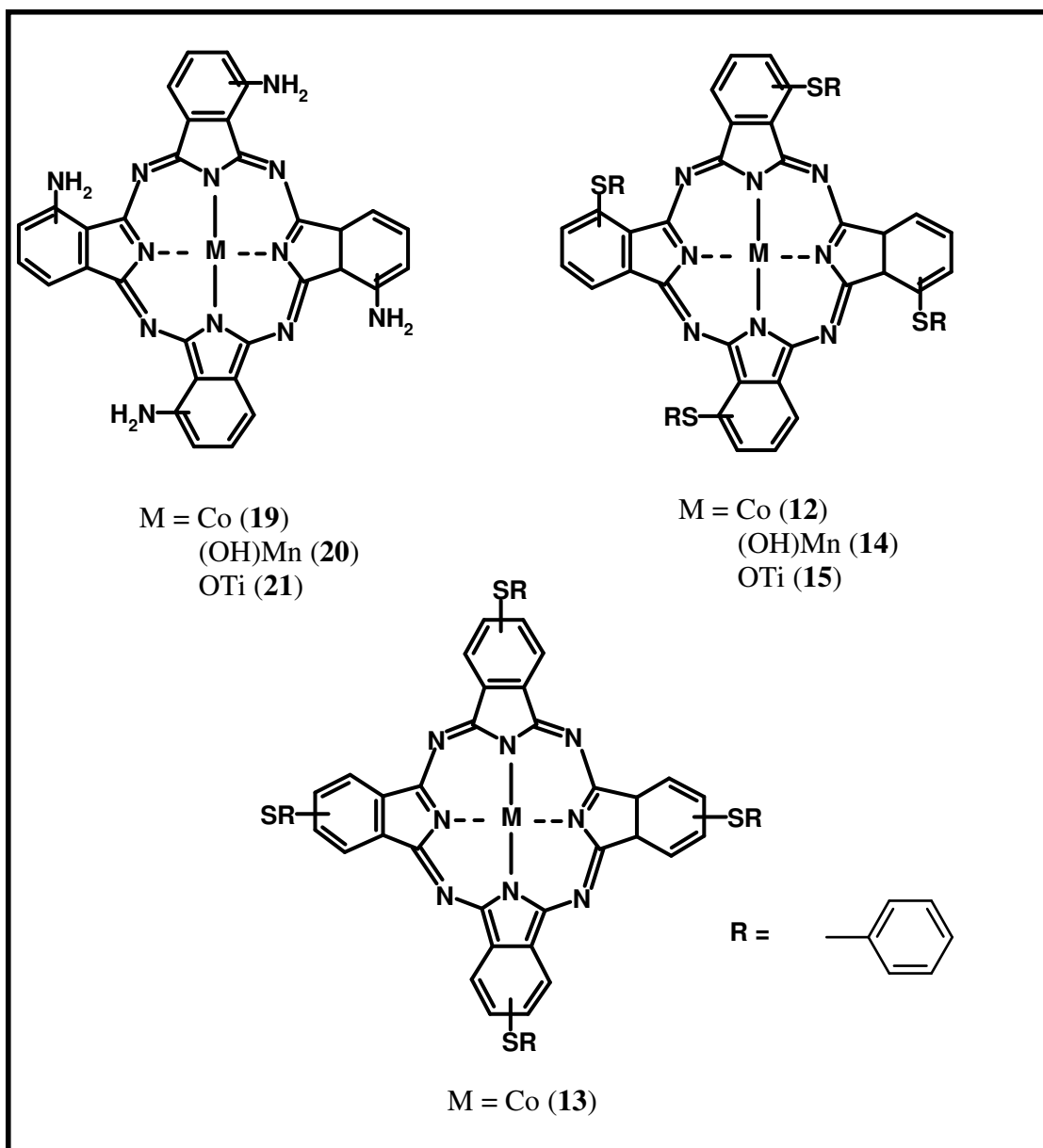


Figure 1. 16: Structures of Co, Mn and Ti phthalocyanines studied.

Chapter 2

Experimental

2. Experimental

2.1 Materials

Acetone, chloroform (CHCl_3), dichloromethane (DCM), N,N, dimethyl formamide (DMF), dimethylsulphoxide (DMSO), ethanol, methanol, 1-octanol, tetrahydrofuran (THF) were obtained from SAARChem or Aldrich. The solvents used for electrochemistry were distilled before use. Water collected from a nanopure Milli-Q water purification system of Millipore (Millipore Corp., Bedford, MA, USA) was used for all aqueous solutions. Buffer tablets (pH 4), Deuterated dimethylsulphoxide (d_6 -DMSO), acetic acid (Ac_2O), acetic anhydride, ammonia solution (NH_4OH) (25% or 32%), ammonium molybdate, cobalt acetate, formamide, manganese acetate, nitric acid, 3-nitrophthalic acid, potassium bromide, potassium ferrocyanide, potassium ferricyanide, sodium borate, sodium dihydrogen phosphate, sodium hydrogen phosphate, sodium hydroxide, sodium nitrite, sodium sulphide monohydrate, sulphuric acid, tetrabutylammonium tetrafluoroborate (TBABF_4), thionyl chloride, thiophenol, titanium butoxide, urea, were purchased from Sigma-Aldrich, SAARChem, or Merck. All reagents were used as received from suppliers. Column chromatography was performed on silica gel 60 (0.04 - 0.063mm).

Gold ultra-micro wire was purchased from Goodfellow Metals Ltd., UK, Teflon was purchased from Stokvis Plastics, Belgium and the gold coated fibers were prepared according to the in-house developed procedures at the Department of Textiles, Gent University.

2.2 Instrumentation

UV/Vis spectra were recorded on a Cary 50 or Cary 500 UV-Vis-NIR spectrometer or on the Shimadzu spectrometer. IR spectra (KBr pellets) were recorded on a Perkin-Elmer spectrum 2000 FTIR spectrometer. $^1\text{H-NMR}$ spectra were recorded using a Bruker EMX 400 MHz NMR spectrometer. Elemental analysis was performed at the University of Cape Town using a Thermo Flash EA 1112 series elemental analyzer and at Rhodes University using an Elemental Vario Microcube EL III. Electrochemical data were obtained using BioAnalytical systems (BAS) model 100B/W Electrochemical Workstation or using the Autolab potentiostat PGSTAT 30 (Eco Chemie, Utrecht, The Netherlands) using the General Purpose Electrochemical System data processing software (GPES, software version 4.9) or Advanced Electrochemical System (Princeton Applied Research) PAR-STAT 2273 equipment. Spectroelectrochemical data was obtained using a BAS CV 27 voltammograph connected to a Cary 500 UV-vis-NIR spectrometer or to a Cary 50 UV/Vis spectrometer. RamanScope images were taken using a Bruker Vertex 70-Ram II spectrometer.

2.3. Electrochemical methods

Cyclic voltammetry (CV), square wave voltammetry (SWV) and differential pulse voltammetry data were obtained using the three-electrode system: the working electrodes were either a glassy carbon (GCE, 3 mm diameter), a gold disk ($r = 0.2 \text{ mm}$), an ultramicro wire ($r = 0.25 \text{ }\mu\text{m}$) or gold coated fiber ($9 \text{ }\mu\text{m}$ diameter). Ag|AgCl wire pseudo-reference electrode and a platinum wire counter electrode, were employed. The

potential response of Ag|AgCl pseudo-reference in aqueous conditions was less than the Ag|AgCl (3M KCl) by 0.015 ± 0.003 V. The SWV settings were: step potential = 4mV, pulse height = 25mV, pulse frequency = 15 Hz. Rotating disk electrode voltammetry was carried out using a BioAnalytical System (BAS) model 100B/W Electrochemical Workstation. Electrochemical experiments were performed in stirred DMF containing ~ 0.1M tetrabutylammonium tetrafluoroborate (TBABF₄) as a supporting electrolyte.

The glassy carbon electrode was polished before use with alumina paste on a Buehler felt pad followed by washing with deionised water, sonicating in ethanol and then rinsing in DMF. The gold disk electrode was polished with slurries of 0.05 μm alumina on a SiC-emery paper, thereafter the electrode was sonicated in ethanol for one hour to remove residual alumina particles. The gold electrode was then immersed in a hot piranha solution (1:3, v/v, 30% H₂O₂ and concentrated H₂SO₄) to remove organic particles that may still be on the electrode surface. The electrode was then rinsed in Millipore water and then with distilled DMF.

The gold ultramicroelectrode was sonicated in ethanol for one hour and then it underwent oxidative cleaning using linear sweep voltammetry scans from -1.5 V to 1.5 V, the same was done for the gold coated fiber. The hot piranha solution could not be used as it would have destroyed the micro wire and the fiber. The fiber and the micro wire were then rinsed with Millipore water followed by distilled DMF.

The concentrations of the MPc complexes were maintained at $\sim 1 \times 10^{-3}$ M in DMF.

Argon or nitrogen gas was bubbled before recording voltammograms and an argon or nitrogen atmosphere was maintained during the electrochemical experiments.

Spectroelectrochemical data were recorded using a home-made optically transparent thin-layer electrochemical (OTTLE) cell. The OTTLE cell is made out of a platinum wire mesh as the working and counter electrodes with a silver wire as the pseudo-reference electrode. The OTTLE cell was connected to the BAS CV 27 voltammograph and UV/Vis spectra were recorded with Cary 50 or Cary 500 UV/Vis/NIR.

The glassy carbon electrode was modified using the electropolymerisation method, this was achieved by repetitive scanning (via cyclic voltammetry) of the 1mM MPc solution in DMF containing TBABF₄ at 100 mVs⁻¹. After polymerization, the modified GCE was rinsed with DMF and then with Millipore water. The gold working electrodes were modified using the self-assembled monolayer method by immersing the gold electrodes in a 1mM MPc solution for 48 hours. Millipore water was used for the electrocatalytic studies in aqueous solutions. Electrocatalysis was performed in solutions of nitrite in phosphate buffer (pH 7.4) prepared from sodium hydrogen phosphate (Na₂HPO₄) and sodium dihydrogen phosphate (NaH₂PO₄). L-cysteine electrocatalysis was performed in pH 4 buffer solutions prepared by dissolving pH 4 buffer tablets in distilled water.

2.4 Synthesis

2.4.1 Phthalonitriles

2.4.1.1 3-Nitrophthalonitrile (Scheme 3.1) [115]

3-Nitrophthalic anhydride (2):

3-Nitrophthalic acid (**1**) (30.0 g, 0.14 mol) was heated in the presence of acetic anhydride (27 ml) in a round bottom flask until the acid was dissolved, the reaction mixture was then refluxed for a further 10 minutes. The resulting yellow solution was poured in a

porcelain dish and left to cool. A yellow precipitate was formed and ground with a pistol. The solid mass was washed with diethyl ether until the unreacted acid could not be detected. The yellow solid mass was left to dry in air. Yield: 26 g (86 %). IR [(KBr) $\nu_{\max}/\text{cm}^{-1}$]: 1772 (-C=O-O-C=O-), 1538 (NO₂ asym), 1343 (NO₂ sym).

3-Nitrophthalimide (3):

A solution of 3-nitrophthalic anhydride (**2**) (25.0 g, 0.13 mol) in formamide (32 ml) was heated under reflux for 3 hours to get the title compound. The resulting mixture was cooled, filtered, washed with water and left to dry at 60°C. Yield: 22 g (88 %). IR [(KBr) $\nu_{\max}/\text{cm}^{-1}$]: 3484 (N-H), 1541 (NO₂ asym), 1324 (NO₂ sym), .

3-Nitrophthalamide (4):

3-Nitrophthalimide (**3**) (21.0 g, 0.11 mol) was stirred in 25% ammonium solution (138 ml) for 24 hours. The mixture was filtered and washed with cold water until excess ammonia was not detected. The title compound was dried at 110°C. Yield: 18 g (85 %). IR [(KBr) $\nu_{\max}/\text{cm}^{-1}$]: 3236 (N-H), 1543 (NO₂ asym), 1333 (NO₂ sym).

3-Nitrophthalonitrile (5):

Dry DMF (167 ml) was poured in a three-necked flask under argon and cooled to 0°C using an ice bath. Maintaining this temperature, thionyl chloride (17 ml) was added drop by drop while stirring, thereafter the solution was left to reach room temperature and stirring was continued for 30 minutes. The solution was again cooled to 0°C followed by the slow addition of 3-nitrophthalamide (**4**) (20.0 g, 0.10 mol) with stirring. The mixture

was stirred for 3 hours at room temperature, thereafter the mixture was poured onto crushed ice (~ 200 g), filtered and washed with cold water. The pale yellow title compound was dried at 110°C.

Yield: 17 g (85 %). IR [(KBr) $\nu_{\max}/\text{cm}^{-1}$]: 2240 (C≡N), 1546 (NO₂ asym), 1355 (NO₂ sym). ¹H-NMR (DMSO-*d*₆): δ ppm 8.64 (1-H, d, Ar-H), 8.48 (1-H, d, Ar-H), 8.12 (1-H, t, Ar-H)).

2.4.1.2 4-Nitrophthalonitrile (Scheme 3.1) [116]

4-Nitrophthalimide (7):

To 95% H₂SO₄, 55% HNO₃ was added (100 ml), the mixture was allowed to cool down to 15°C using an ice bath. Thereafter phthalimide (**6**) (30.0 g, 0.20 mol) was added portion wise to the acid solution while stirring maintaining the temperature between 10 and 15°C. The temperature was increased to 35°C and the mixture stirred at that temperature for an hour. After cooling to 0°C, the yellow reaction mixture was poured onto crushed ice (500 g) while stirring to yield a beige suspension. The mixture was filtered and the solid mass was thoroughly washed with cold water and the title compound was dried at 110°C.

Yield: 26 g (86 %). IR [(KBr) $\nu_{\max}/\text{cm}^{-1}$]: 3484 (N-H), 1541 (NO₂ asym), 1324 (NO₂ sym).

4-Nitrophthalamide (8) and *4-nitrophthalonitrile (9)* were synthesized by following methods similar to *3-nitrophthalamide (4)* and *3-nitrophthalonitrile (5)*.

4-Nitrophthalamide (8):

Yield: 26 g (87 %). IR [(KBr) $\nu_{\max}/\text{cm}^{-1}$]: 3331 (N-H), 1546 (NO₂ asym), 1349 (NO₂ sym)

4-Nitrophthalonitrile (9):

Yield: 26 g (85 %). IR [(KBr) $\nu_{\max}/\text{cm}^{-1}$]: 2241 (C≡N), 1542 (NO₂ asym), 1352 (NO₂ sym). ¹H-NMR (DMSO-*d*₆): δ ppm 7.75 (1-H, s, Ar-H), 7.63 (1-H, d, Ar-H), 7.58 (1-H, d, Ar-H).

2.4.1.3 Phenylthiosubstituted phthalonitriles (Scheme 3.2) [117]**3-(phenylthio)phthalonitrile (10):**

Under a stream of nitrogen, thiophenol (4.63 g, 42.0 mmol), and **5** (6.0 g, 35.0 mmol) were dissolved in dry DMSO (30 ml), the mixture was stirred at room temperature for 15 minutes. Thereafter, finely ground K₂CO₃ (15 g, 0.105 mmol) was added portion-wise for a 2 hour period and the reaction mixture was stirred for 12 hours. The resultant mixture was added to water (100 ml) and stirred for 30 minutes. The precipitate was filtered off, washed with water, dried and recrystallised from ethanol.

Yield: 5.5 g (91 %). IR [(KBr) $\nu_{\max}/\text{cm}^{-1}$]: 2229 (C≡N), 688 (C-S-C). ¹H-NMR (DMSO-*d*₆): δ ppm 7.92 (1-H, d, Ar-H), 7.73 (1-H, t, Ar-H), 7.63-7.58 (5-H, m, Ar'-H), 7.41 (1-H, d, Ar-H).

4-(phenylthio)phthalonitrile (11):

Synthesis and purification of **11** was as described for **10**, using **9** instead of **5**. Yield: g (6.5 g, 80 %). IR [(KBr) $\nu_{\max}/\text{cm}^{-1}$]: 2223 (C \equiv N), 693 (C-S-C). $^1\text{H-NMR}$ (DMSO- d_6): δ ppm 7.88 (1-H, d, Ar-H), 7.72 (1-H, s, Ar-H), 7.61-7.48 (5-H, m, Ar'-H), 7.39 (1-H, d, Ar-H).

2.4.2 Phthalocyanines**2.4.2.1 Phenylthio tetra-substituted phthalocyanines (Scheme 3.3) [54]*****Cobalt (1, (4)-(tetraphenylthiophthalocyaninato) (12):***

In anhydrous ethylene glycol (20.4 ml), 3-(phenylthio)phthalonitrile (**10**) (2.55 g, 10.7 mmol) and cobalt (II) acetate (0.64 g, 2.68 mmol) were stirred under reflux in a nitrogen atmosphere at 200°C for 5 hours. The reaction mixture was left to cool to room temperature, thereafter methanol (30 ml) was added to precipitate out the dark green crude product. The mixture was filtered and treated in a Soxhlet extraction apparatus with ethanol for 48 hours. The product was further purified by column chromatography, using THF as the eluting solvent. After evaporation of the solvent, the product was purified further by washing twice in methanol and lastly in acetone, to give a pure dark green product. Yield: 36%. UV-Vis (DMF): λ_{\max} nm (log ϵ) 326 (4.15), 626 (4.56), 693 (4.71). IR [(KBr) $\nu_{\max}/\text{cm}^{-1}$]: 668 (C-S-C). Calc. for $\text{C}_{56}\text{H}_{32}\text{N}_8\text{OS}_4\text{Co}$: C, 66.98; H, 3.21; N, 11.16; Found: C, 66.17; H, 3.20; N, 10.65.

Cobalt 2,(3)-(tetrphenylthiophthalocyaninato) (13):

Synthesis, purification and the amount of reagents used for **13** was the same as for **12** except **11** instead of **10** was used. Yield: 40%. UV-Vis (DMF): λ_{\max} nm (log ϵ) 331 (4.03), 608 (4.51), 671 (4.66). IR [(KBr) $\nu_{\max}/\text{cm}^{-1}$]: 686 (C-S-C). Calc. for $\text{C}_{56}\text{H}_{32}\text{N}_8\text{OS}_4\text{Co}$: C, 66.98; H, 3.21; N, 11.16; Found: C, 66.68; H, 3.36; N, 10.33.

Manganese 1,(4)-(tetrphenylthiophthalocyaninato) (14):

Synthesis, purification and the amount of reagents used for **14** was the same as for **12** except manganese acetate instead of cobalt acetate was used. Yield: 40%. UV-Vis (DMF): λ_{\max} nm (log ϵ) 352 (3.91), 510 (4.21), 680 (4.39), 770 (4.85). IR [(KBr) $\nu_{\max}/\text{cm}^{-1}$]: 689 (C-S-C).

Calc. for $\text{C}_{56}\text{H}_{32}\text{N}_8\text{OS}_4\text{Mn}$: C, 67.18; H, 3.32; N, 11.19; Found: C, 67.80; H, 2.79; N, 12.04.

Oxotitanium 1,(4)-(tetrphenylthiophthalocyaninato) (15):

Synthesis and purification of **15** was done in our group and reported [117].

2.4.2.2 Amino substituted phthalocyanines (Scheme 3.4) [118]***Cobalt 1, (4)-(tetrnitrophthalocyaninato) (16):***

A mixture of 3-nitrophthalimide (**3**) (4 g, 0.02 mmol) in the presence of excess urea (3 g, 0.05 mmol), ammonium molybdate (0.08 g, 0.8 mmol) and cobalt acetate (1.03 g, 4.12 mmol) in nitrobenzene (15 ml) was refluxed for 5 hours to give the title compound. The product was washed with methanol and water and dried at 110°C. Yield: 75%. UV-Vis

(DMF): λ_{max} nm 335, 412, 592, 654. IR [(KBr) ν_{max} /cm⁻¹]: 1527 (NO₂ asym), 1343 (NO₂ sym).

Compound **16** was immediately used to form **19** without further characterization.

Manganese 1, (4)-(tetranitrophthalocyaninato) (17) was synthesized as described for **16** except manganese acetate instead of cobalt acetate was used. Yield: 80%. UV-Vis (DMF): λ_{max} nm 470, 679, 760. IR [(KBr) ν_{max} /cm⁻¹]: 1557 (NO₂ asym), 1336 (NO₂ sym), 891 (Mn-OH).

Compound **17** was immediately used to form **20** without further characterization.

Oxotitanium 1, (4)-(tetranitrophthalocyaninato) (18):

A mixture of **5** (3g, 17.34 mmol), titanium butoxide (1.63g, 4.75 mmol), urea (0.52g, 8.67mmol), in 1-octanol (4.4 ml) was heated under argon atmosphere at 150°C for 6 hours. The reaction mixture was then cooled and refluxed in 15 ml of methanol for 30 minutes. The dark brown product was filtered and washed with distilled water and methanol then dried at 70°C to give the title compound. Yield: 75%. UV-Vis (DMF): λ_{max} nm 408, 611, 676. IR [(KBr) ν_{max} /cm⁻¹]: 1537 (NO₂ asym), 1316 (NO₂ sym), 736 (Ti=O).

Compound **18** was immediately used to form **21** without further characterization.

Cobalt 1, (4)-(tetraminophthalocyaninato) CoTAPc (19):

Addition of sodium sulphide nonahydrate (7.5g, 31.1 mmol) to complex **16** (1.5g, 1.98 mmol) in distilled water (45 ml) resulted in the conversion to amino-derivatised

complexes after 5 hours of stirring at 50 °C. The crude products were purified by repetitive washing with HCl (1 M), NaOH (1 M) and water to give the title compound. Yield: 70%. IR (KBr) ν (cm^{-1}): 3309 (N-H), 2360, 1623 (NH_2), 1308, 1157. UV-Vis (DMF): λ_{max} nm ($\log \epsilon$) 311 (5.01), 467 (4.53), 678 (4.67), 749 (4.99). Calc. for $\text{C}_{32}\text{H}_{20}\text{N}_{12}\text{Co}$: C, 60.85; H, 3.19; N, 26.62; Found: C, 59.38; H, 4.59; N, 26.59.

Manganese 1, (4)-(tetraminophthalocyaninato) (OH)MnTAPc (20) was synthesized as described for **19** except **17** instead of **16** was used. Yield: 84 %. IR (KBr) ν (cm^{-1}): 3415 (N-H), 1618, 1485, 1322, 1263, 1163, 1067, 894 (Mn-OH), 735, 617. UV/Vis/NIR (DMF): λ_{max} /nm ($\log \epsilon$) 354 (4.73), 547 (4.45), 763 (3.49), 871 (4.89). Calc. for $\text{C}_{32}\text{H}_{26}\text{N}_{12}\text{O}_6\text{MnNa}$: C, 45.55; H, 2.08; N, 19.90; Found: C, 46.95; H, 3.34; N, 20.65.

Oxotitanium 1, (4)-(tetraminophthalocyaninato) OTiTAPc (21) was synthesized as described for **19** except **18** instead of **16** was used. Yield: 75 %. IR (KBr) ν (cm^{-1}): 3365 (N-H), 2354, 1609 (NH_2), 1325, 1104, 954 (Ti=O), 735. UV/Vis/NIR (DMF): λ_{max} /nm ($\log \epsilon$) 330 (4.0) 525 (2.83), 740 (3.47), 830 (3.83). Calc. for $\text{C}_{32}\text{H}_{21}\text{N}_{12}\text{O}_2\text{TiNa}$: C, 56.81; H, 2.91; N, 24.80; Found: C, 55.06; H, 3.89; N, 21.73.

2.5 Nitrite sample preparation

A sausage sample was purchased at a local supermarket, 5g of the meat sample was treated according to the reported procedure [119]. Briefly the sample was mixed with 7.0 ml of saturated borax solution in a 100 ml beaker and stirred. After 15 minutes 30.0 ml of water (70°C) was added into the beaker and the mixture was left to boil for 30 minutes.

Afterwards 5 ml of potassium ferrocyanide (2.5 mM) and 5 ml 20% w/w zinc acetate solution were added to the beaker in order to precipitate out proteins. The mixture was cooled to room temperature, diluted to 100 ml with water and was left to settle for 30 minutes. The upper lipid layer was removed by quick centrifugation followed by filtration to remove small lipid particles.

Results and Discussion

The results presented in this section have been published in journals listed below:

1. Electrochemical and electrocatalytic properties of α substituted manganese and titanium phthalocyanines. **Nolwazi Nombona**, Prudence Tau, Nthapo Sehlotho, Tebello Nyokong, *Electrochim. Acta*, 53, (2008), 3139.

2. The synthesis, cyclic voltammetry and spectroelectrochemical studies of Co(II) phthalocyanines tetra-substituted at the α and β positions with phenylthio groups. **Nolwazi Nombona**, Tebello Nyokong, *Dyes and Pigments*, 80, (2009), 130.

3. Comparative electrocatalytic behavior of self-assembled monolayer of thiol derivatised Co(II) phthalocyanines on gold disk, ultramicro cylinder and fiber electrodes. **Nolwazi Nombona**, Daniela A. Geraldo, Jean Hakuzimana, Anne Schwarz, Phillipe Westbroek, Tebello Nyokong, *J. Appl. Electrochem.*, (2008), In press.

The results obtained in this section have been separated into three chapters:

Chapter 3:

Synthesis and characterization of MPc derivatives

Chapter 4:

Electrode modification and characterization

Chapter 5:

Electrocatalysis

Chapter 3

Synthesis and characterization of MPc derivatives

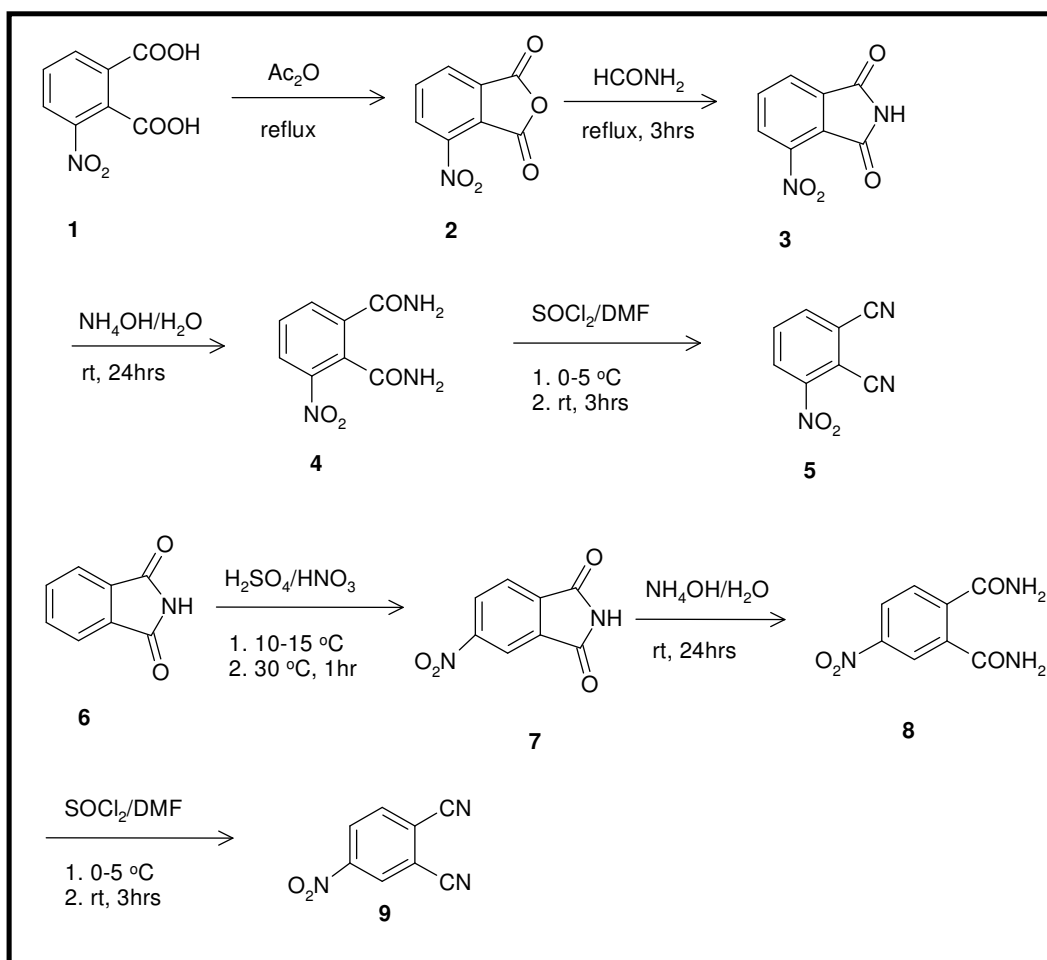
3. Synthesis and characterization of MPc derivatives

3.1 Synthesis and spectral characterization

3.1.1 Phthalonitriles

3.1.1.1 Nitro substituted phthalonitriles (Scheme 3.1)

Nitro substituted phthalonitriles were synthesized according to literature [115, 116] as shown in Scheme 3.1 using 3-nitrophthalic acid (**1**) and phthalimide (**6**) as starting materials to yield (**5**) and (**9**) respectively.



Scheme 3. 1: Synthetic pathway to 3-nitrophthalonitrile (**5**) and 4-nitrophthalonitrile (**9**).

High yields and satisfactory IR data were obtained for all the compounds. The appearance of the carboxylic acid anhydride (-C=O-O-C=O) band at 1772 cm^{-1} confirmed the conversion of **1** to **2**. Compound **3** was confirmed by the presence of the N-H stretch at 3484 cm^{-1} . An amide band at 3236 cm^{-1} was observed for compound **4**, the $\text{C}\equiv\text{N}$ stretch at 2240 cm^{-1} confirmed the conversion of **4** to **5**.

The conversion of compound **6** to compound **7** was achieved using concentrated HNO_3 as the reagent and concentrated H_2SO_4 as the acid catalyst. The appearance of the NO_2 bands at 1324 and 1541 cm^{-1} confirmed this conversion. The conversion of **7** to **8** was indicated by an amide stretch at 3331 cm^{-1} . The synthesis of 4-nitrophthalonitrile was confirmed by the $\text{C}\equiv\text{N}$ stretch at 2241 cm^{-1} .

The ^1H NMR data of **5** and **9** gave satisfactory results confirming the structure of the compounds. Shown in Figure 3.1 is the proton NMR of compound **5**, doublet peaks at 8.64 and 8.48 ppm correspond to proton a and b respectively and the deshielded triplet at 8.12 ppm corresponds to proton c that is split by proton a and b.

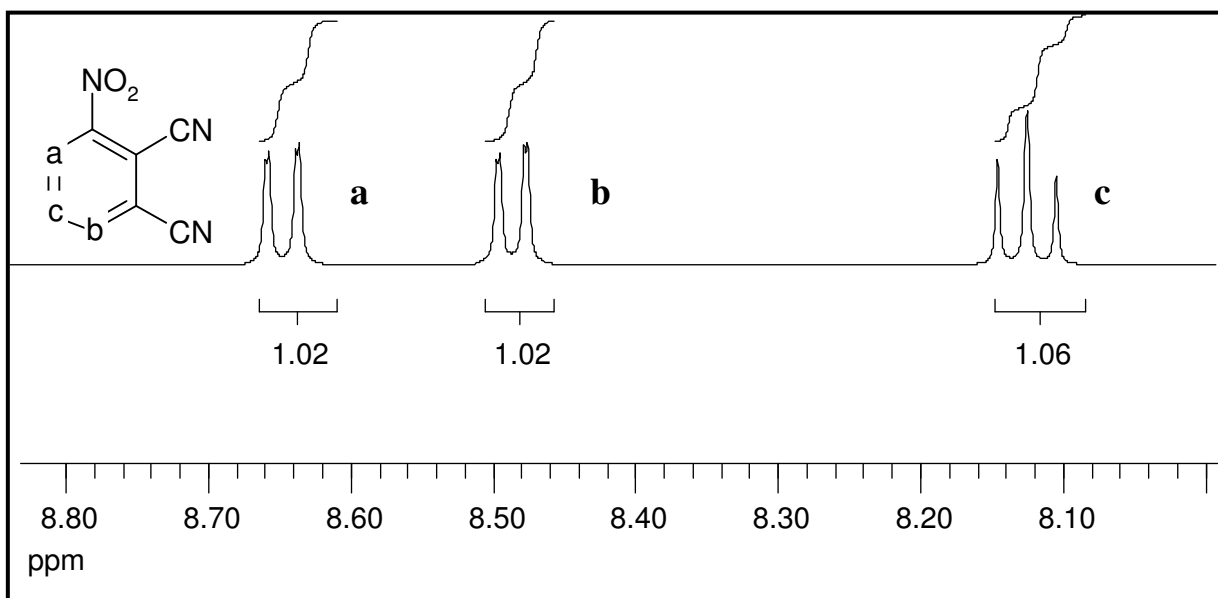
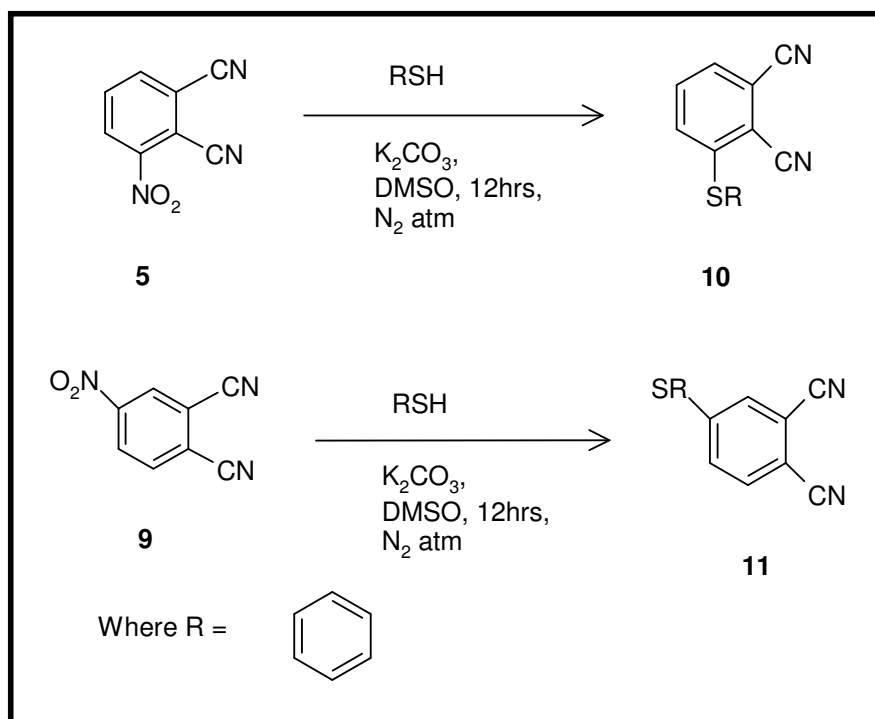


Figure 3. 1: ^1H NMR spectrum of 3-nitrophthalonitrile in $\text{DMSO-}d_6$.

3.1.1.2 Phenylthio derivatised phthalonitrile (Scheme 3.2)

The 3-nitro and 4-nitrophthalonitriles are susceptible to nucleophilic attack due to the electron-withdrawing capability of the dinitrile functionalities. The NO_2 is a good leaving group for nucleophilic aromatic substitution reactions and thiols are effective nucleophiles in nucleophilic substitution reactions [30]. This makes the synthesis of 3-(phenylthio)phthalonitrile and 4-(phenylthio)phthalonitrile shown in Scheme 3.2 relatively simple. The base (K_2CO_3) catalyzed nucleophilic substitution of the nitro groups was performed in dry DMSO at room temperature in inert nitrogen atmosphere.

Good yields were obtained for compounds **10** and **11**. IR data confirmed the presence of the C-S-C stretch at 688 and 693 cm^{-1} for the 3-(phenylthio)phthalonitrile and 4-(phenylthio)phthalonitrile respectively and the $\text{C}\equiv\text{N}$ stretch at 2229 and 2223 cm^{-1} . ^1H NMR data gave expected number of protons (details in the experimental section).

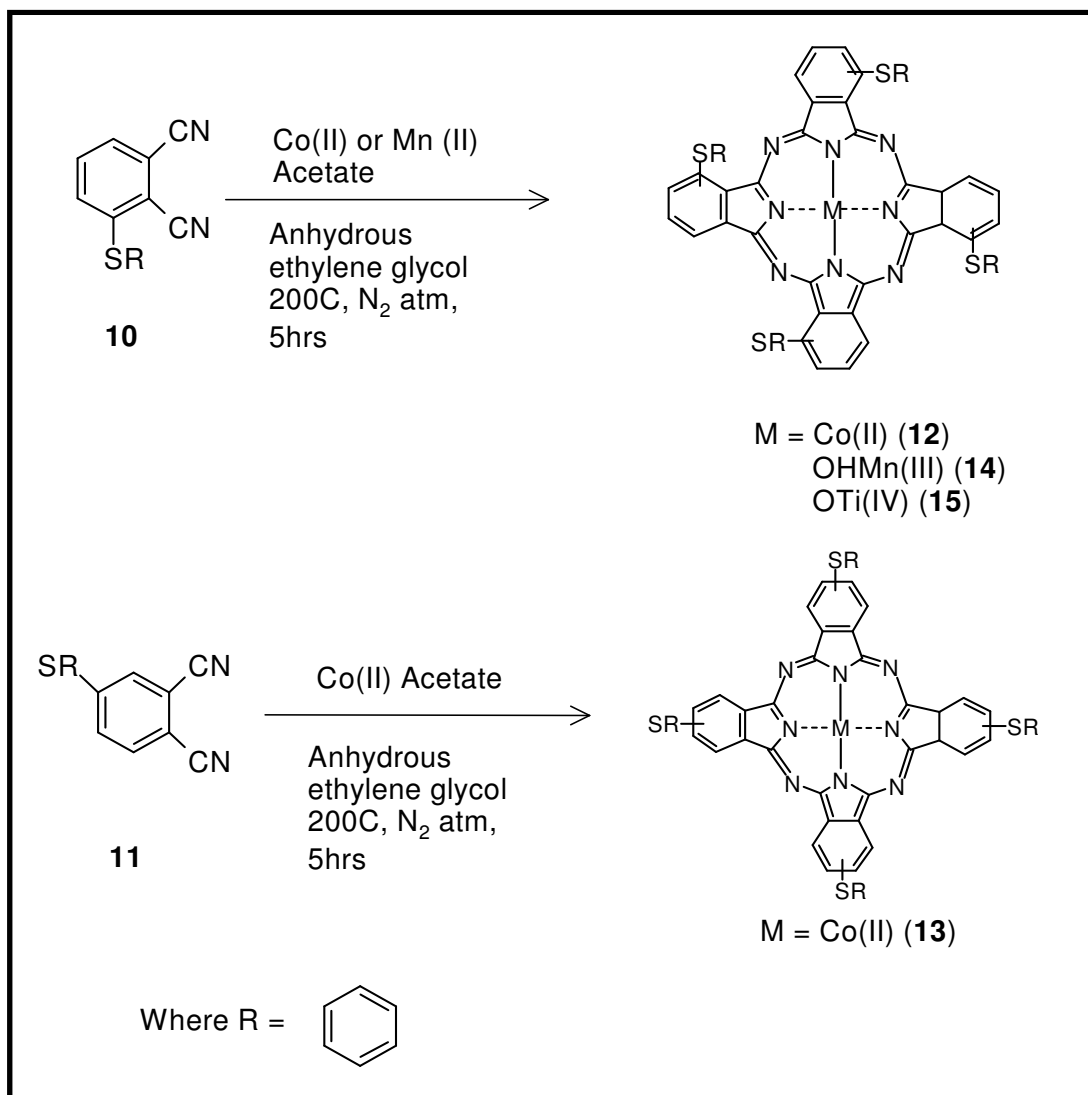


Scheme 3. 2: Synthetic pathway to thio derivatized phthalonitriles.

3.1.2 Phenylthio derivatized metallophthalocyanines (Scheme 3.3)

Synthetic routes used for the phthalocyanine complexes used for the electrocatalysis of nitrite and L-cysteine are shown in Scheme 3.3 and 3.4. Table 3.1 gives a summary of the main absorption bands for oxidized and reduced species for complexes **12-15** and **19-21**. Data for **15** was obtained from reference [117]

Thio derivatized phthalocyanines were synthesized according to the reported procedure (Scheme 3.3) [50]. This method involves the cyclotetramerisation of substituted phthalonitriles (**10** and **11**) when reacted with Co and Mn acetate salts in anhydrous ethylene glycol. Low yields varying from 36 to 40% were obtained. Complex **15** was reported before [117]. Characterization of these complexes was performed using classical methods such as UV/Vis, IR and elemental analyses.



Scheme 3. 3: Synthetic pathway for Co, Mn and Ti tetra substituted phthalocyanines.

Table 3. 1: Main absorption bands for complexes **12-15** and **19-21**.

Complex	Q-band absorption	Assignment	Solvent
12	695	Co(II)Pc	DMF
	726	Co(I)Pc	DMF/TBABF ₄
	709	Co(III)Pc	DMF/TBABF ₄
13	673	Co(II)Pc	DMF
	711	Co(I)Pc	DMF/TBABF ₄
	686	Co(III)Pc	DMF/TBABF ₄
14	770	Mn(III)Pc	DMF
	708	Mn(II)Pc	DMF/TBABF ₄
15^a	744	OTi(IV)Pc	DMF
	710	OTi(III)Pc	DMF/TBABF ₄
	706	OTi(II)Pc	DMF/TBABF ₄
19	749	Co(II)Pc	DMF
	765	Co(I)Pc	DMF/TBABF ₄
20	871	Mn(III)Pc	DMF
	762	Mn(II)Pc	DMF/TBABF ₄
21	830	OTi(IV)Pc	DMF
	757	OTi(III)Pc	DMF/TBABF ₄
	750	OTi(II)Pc	DMF/TBABF ₄

^a Data from reference [117]

3.1.2.1 CoPc derivatives (12, 13)

Peripherally (**12**) and non-peripherally (**13**) thio substituted CoPcs were synthesized as shown in Scheme 3.3. The complexes were soluble in common organic solvents such as DMF, DMSO, THF and DCM. The IR spectra of the complexes gave vibrational peaks at 668 cm^{-1} for **12** and 686 cm^{-1} for **13**, confirming the presence of a C-S-C stretch. Figure 3.2 shows the UV/Vis spectra of the synthesized complexes. Complex **12** has a Q-band absorption at 695 nm whereas complex **13** has a Q-band absorption at 673 nm. The 22 nm red-shift observed with complex **12** is due the electron density enhancement caused by the substitution at the non-peripheral (α) position. It is well known that α substitution results in red-shifting of the spectra in MPc complexes [23, 35].

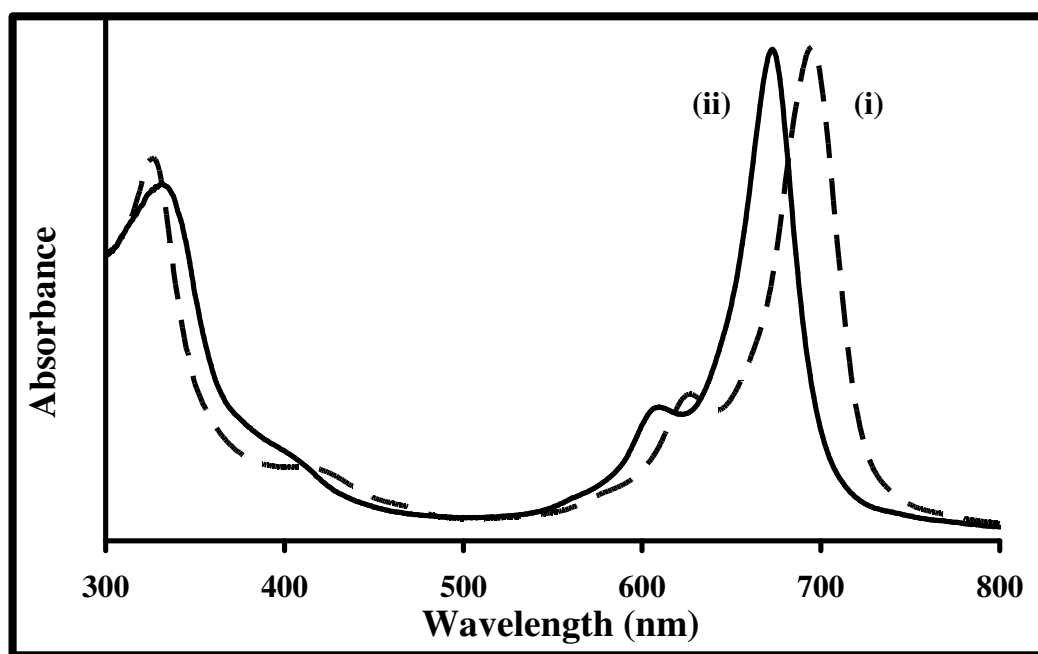


Figure 3. 2: UV/Vis spectra of complex **12**(i) and **13**(ii) in DMF. Concentration: $\sim 1 \times 10^{-6}$ M.

3.1.2.2 (OH)MnPc (**14**) and OTiPc (**15**) derivatives

The UV/Vis spectrum of **14** and **15** are shown in Figure 3.3. The Q-band at 770 nm is highly red shifted and no longer determines the color of **14**, this absorption is more red shifted compared to **12** and **15** [117]. This red shift of the Q-band is typical of $Mn^{3+}Pc$ complexes [36, 38]. The color of **14** is brown due to the absorption in the 400-500 nm region. Bands in this region are charge transfer bands between the metal and Pc ring, they usually occur when the central metal ion has *d* orbitals which lie within the HOMO-LUMO gap of the phthalocyanine ring. Transitions giving rise to these bands can be metal-to-ligand charge transfer or ligand-to-metal charge transfer, these absorption bands are often weak [23].

The IR spectrum of **14** gave a vibrational peak at 689 cm^{-1} confirming the presence of a C-S-C stretch.

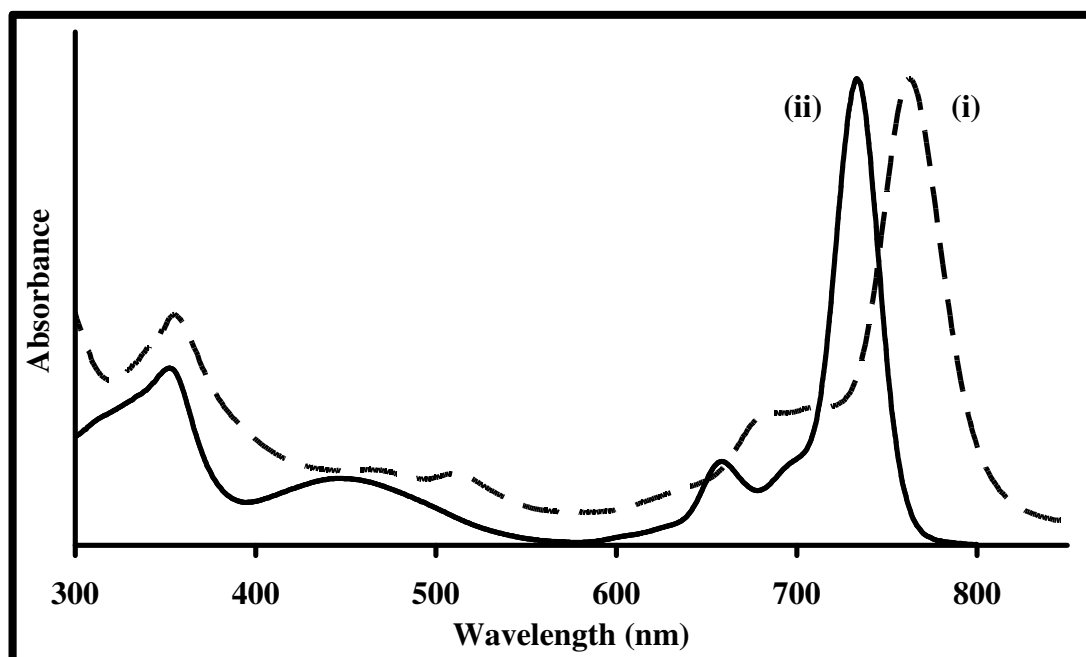
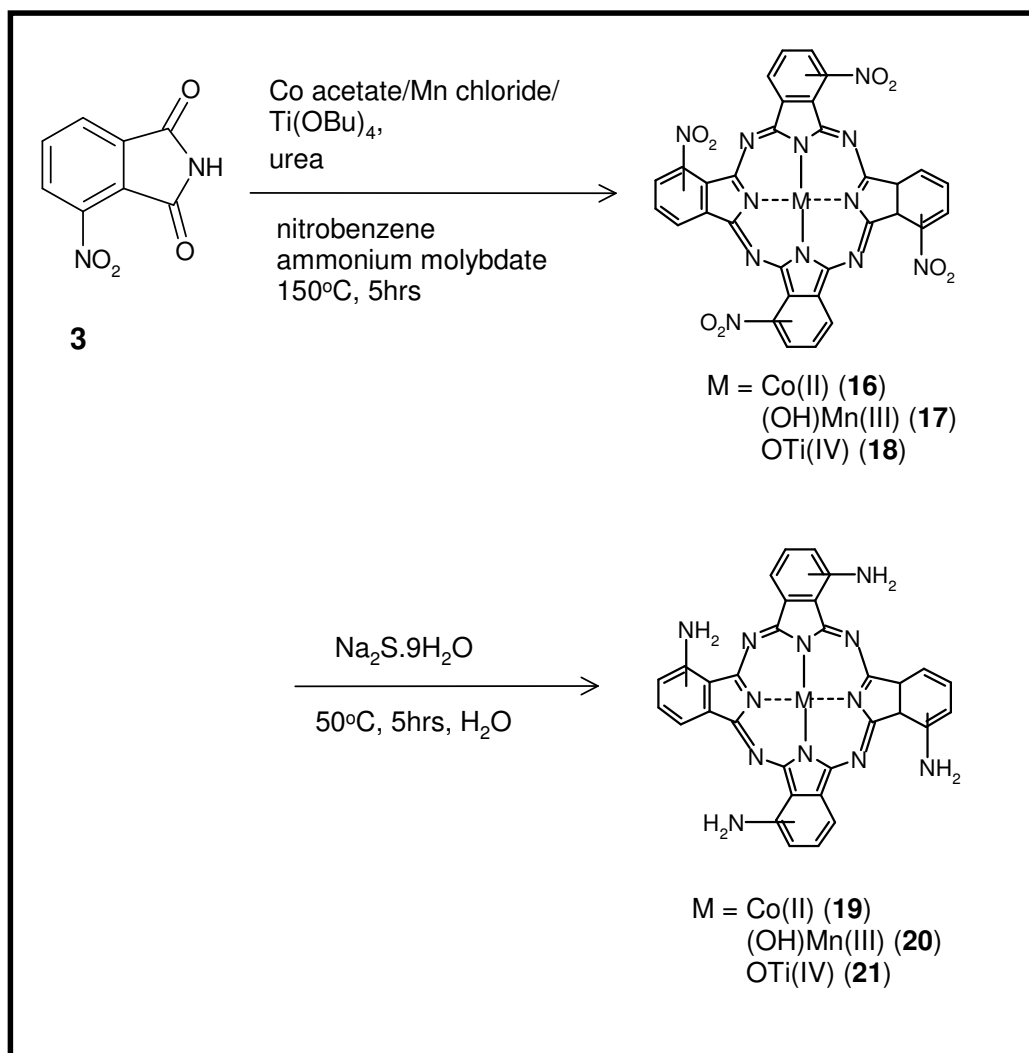


Figure 3. 3: UV/Vis spectrum of complex **14**(i) and **15**(ii) in DMF. Concentration $\sim 1 \times 10^{-6}$ M.

3.1.3 Amino-derivatised phthalocyanines (Scheme 3.4)

The amino-derivatised cobalt, manganese and titanium phthalocyanines were synthesized and characterised according to a method reported by Acher *et al.* [118] using 3-nitrophthalimide (**3**). Scheme 3.4 shows the synthesis of the amino-derivatised phthalocyanines, where **3**, in the presence of urea, ammonium molybdate and metal salt in nitrobenzene is transformed to metallated tetranitrophthalocyanine complexes (MTNPc). Metal salts employed were cobalt (II) acetate, manganese (III) chloride and titanium (IV) butoxide to yield the corresponding **16**, **17** and **18** complexes, respectively. Addition of sodium sulphide nonahydrate to the nitro-derivatised complexes resulted in the conversion to amino-derivatised complexes after 5 hours of stirring at 50 °C. The crude products were purified by repetitive washing with HCl (1 M), NaOH (1 M) and water to give **19**, **20** and **21**.



Scheme 3. 4: Synthetic pathway for Co, Mn and Ti tetraaminophthalocyanines.

The facile preparation of non-peripherally substituted cobalt, manganese and titanium tetraaminophthalocyanine (MTAPc) complexes was afforded from the reduction of the nitro derivatives in good yields. The disappearance of nitro group vibrations and observation of characteristic amino vibrations at $\sim 3400\text{ cm}^{-1}$ confirmed the formation of MTAPc complexes.

3.1.3.1 Cobalt tetraaminophthalocyanine (CoTAPc) (19)

Figure 3.4 shows the electronic absorption spectra of nitro and amino phthalocyanine complexes (**16** and **19**, respectively) in DMF. Typical phthalocyanine absorption bands were observed with the Q-bands observed at 653 and 749 nm for **16** and **19**, respectively. The Q-band of the amino phthalocyanine is more red shifted compared to the nitro phthalocyanine, this is due to the electron donating ability of the amino groups.

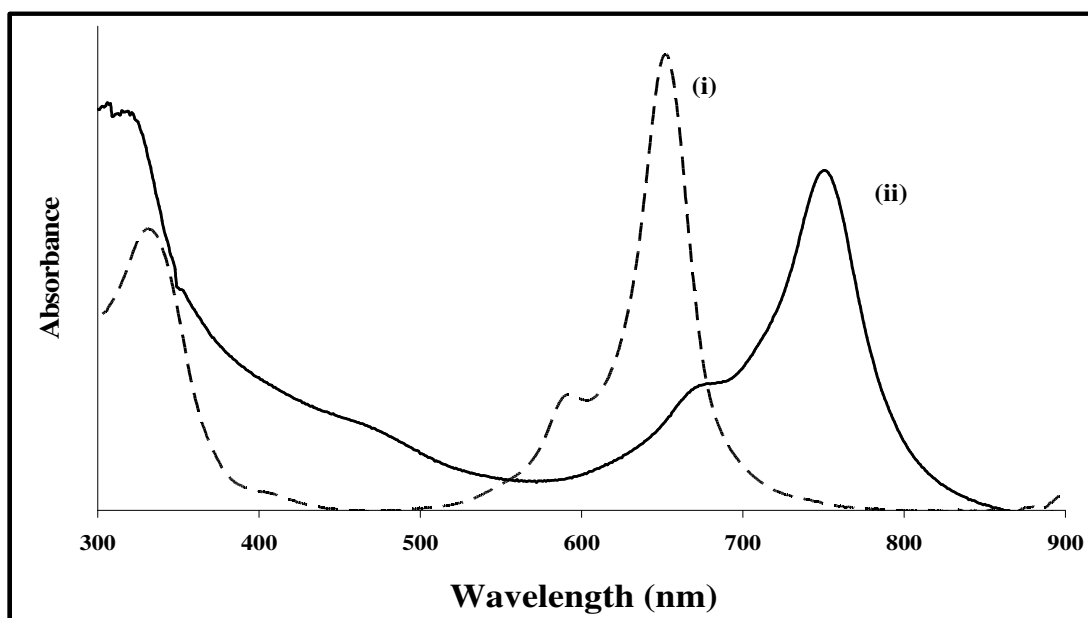


Figure 3. 4: UV/Vis spectra of **16** (i), and **19** (ii) in DMF. Concentrations $\sim 1 \times 10^{-6}$ M.

3.1.3.2 Manganese tetraaminophthalocyanine ((OH)MnTAPc) (20)

Complex **20** exhibits a typical B-band at 354 nm and a Q-band at 871 nm as shown in Figure 3.5. An absorption band at 547 nm is due to charge-transfer from the electron rich amino groups to the electron deficient central metal ion [120]. The presence of hydroxy as an axial ligand is an artefact of purification which included treatment with NaOH. The

presence of OH as an axial ligand was confirmed by IR. Substitution of the MnPc framework with amino groups causes a red-shift into the near-IR in comparison with electronic absorption spectrum of the unsubstituted manganese phthalocyanine (706 nm) in DMF [121] and the nitro substituted manganese phthalocyanine (**17**). The hypsochromic shift of the Q-band is even more pronounced for this non-peripherally (α) substituted complex (871 nm in DMF) in contrast to the peripherally (β) substituted (OH)MnTAPc (784 nm) [46]. Moreover, **20** is purple in solution while the β -substituted derivative is brown.

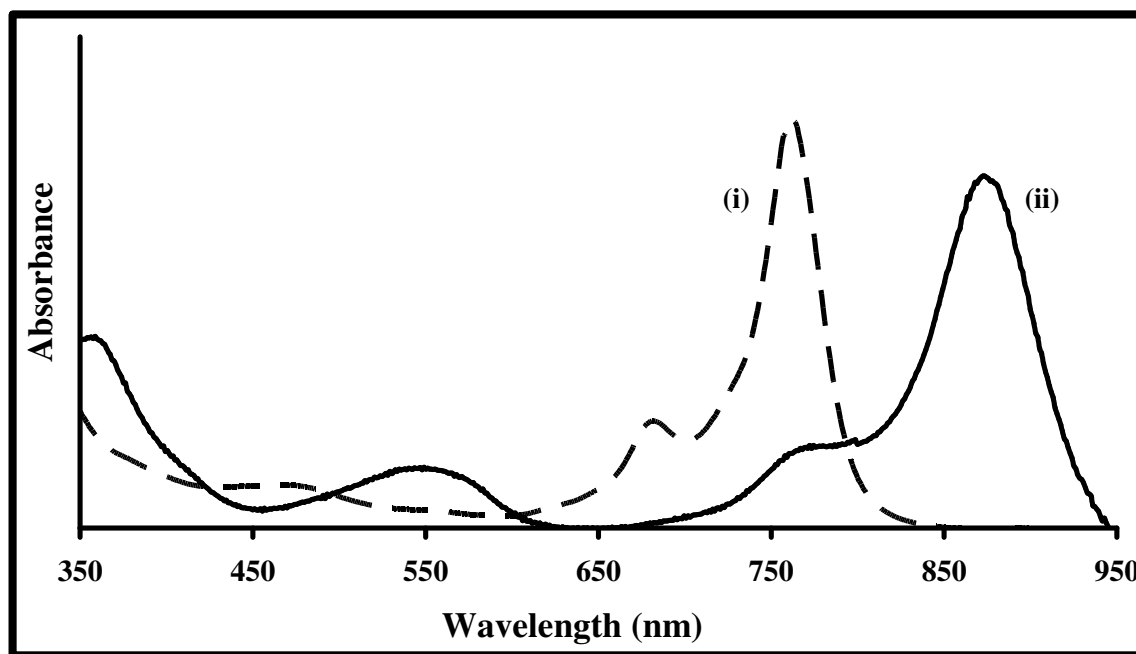


Figure 3. 5: UV/Vis spectra of **17**(i), and **20**(ii) in DMF. Concentrations $\sim 1 \times 10^{-6}$ M.

3.1.3.3 Titanium tetraaminophthalocyanine (OTiTAPc) (**21**)

The UV/Visible spectra of **18** and **21** are shown in Figure 3.6. The nitrophthalocyanine is blue-green in color and the amino phthalocyanine is brown in solution. The Q-band of the

amino phthalocyanine is shifted to the NIR region and no longer determines the color of the phthalocyanine, the brown color is due to absorption between the 500-550 nm region. The Q-band of **18** is at 677 nm whereas for **21** it is observed at 830 nm. The Q-band of β -substituted OTiTAPc was reported [48] at 755 nm in DMF. It is expected for the Q-band of **21** (α -substituted) to be more red shifted compared to the β -substituted complexes, as explained above.

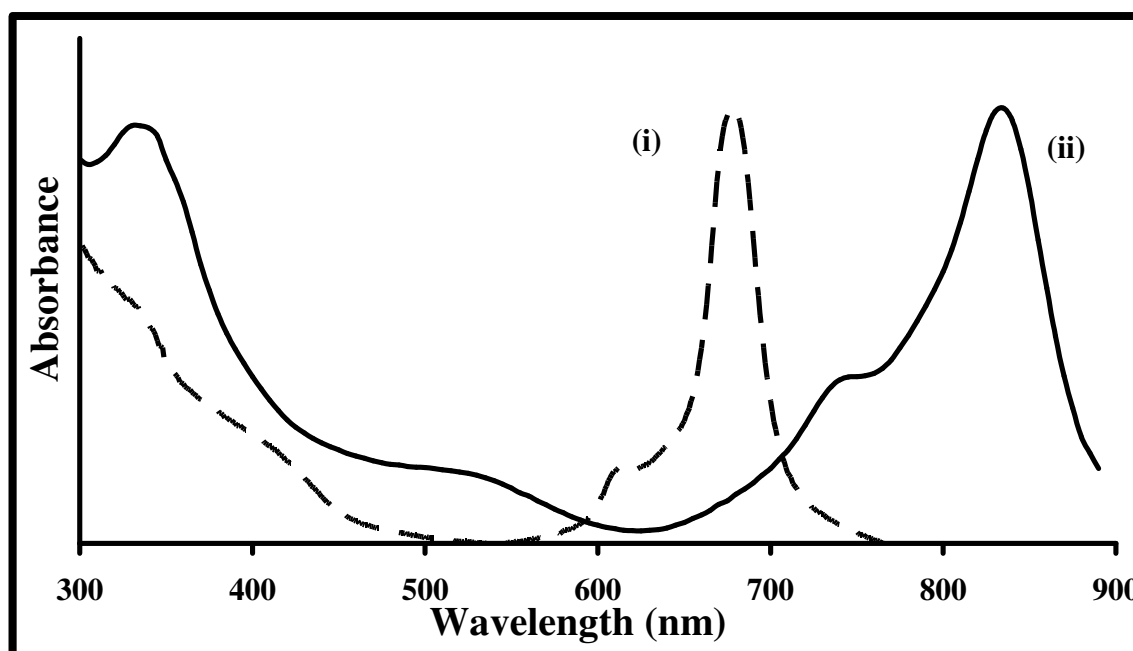


Figure 3. 6: UV/Vis spectra of **18**(i) and **21**(ii) in DMF. Concentrations $\sim 1 \times 10^{-6}$ M.

3.2 Electrochemical characterization

The redox properties of the complexes were probed using cyclic voltammetry and square wave voltammetry in distilled DMF using 0.1 M TBABF₄ as the supporting electrolyte and a glassy carbon electrode as the working electrode. Tables 3.2 and 3.3 show a summary of the potential values and assignments obtained for the phenylthio and amino derivatized phthalocyanine complexes respectively. Data for complex **15** was obtained from reference [117].

Table 3. 2: Summary of redox potentials ($E_{1/2}$ vs. Ag|AgCl) of Co, Mn and Ti phenylthio derivatized Pc complexes in DMF containing 0.1 M TBABF₄ as the supporting electrolyte.

Complex ^a	$E_{1/2}$ /V (vs. Ag AgCl)					
	I (Co ^I Pc ⁻² / Co ^I Pc ⁻³) or (Mn ^I Pc ⁻² / Mn ^I Pc ⁻³) or (Ti ^I Pc ⁻² / Ti ^I Pc ⁻³)	II (Co ^{II} Pc ⁻² / Co ^I Pc ⁻²) or (Mn ^{II} Pc ⁻² / Mn ^I Pc ⁻²) or (Ti ^{III} Pc ⁻² / Ti ^{II} Pc ⁻²)	(Ti ^{IV} Pc ⁻² / Ti ^{III} Pc ⁻²)	III (Co ^{III} Pc ⁻² / Co ^{II} Pc ⁻²) or (Mn ^{III} Pc ⁻² / Mn ^{II} Pc ⁻²)	IV (Co ^{III} Pc ⁻¹ / Co ^{III} Pc ⁻²)	V (Co ^{III} Pc ⁰ / Co ^{III} Pc ⁻¹)
12 Co(II)	-1.44	-0.39	-	0.37	0.78	1.15
13 Co(II)	-1.42	-0.57,-0.39	-	0.27	0.79	1.10
14 Mn(III)	-1.37	-0.76	-	- 0.057	~0.88 too weak for analysis	-
15^b Ti(IV)	-1.33	-0.46	-0.07	-	-	-

^a Central metals in brackets, ^b data from reference [117]

Table 3. 3: Summary of redox potentials ($E_{1/2}$ vs. Ag|AgCl) of Co, Mn and Ti amino derivatized Pc complexes in DMF containing 0.1 M TBABF₄ as the supporting electrolyte.

Complex ^a	$E_{1/2}/V$ (vs. Ag AgCl)					
	I (Co ^I Pc ⁻² / Co ^I Pc ⁻³) or (Mn ^{II} Pc ⁻² / Mn ^{II} Pc ⁻³) or (Ti ^{II} Pc ⁻² / Ti ^{II} Pc ⁻³)	II (Co ^{II} Pc ⁻² / Co ^I Pc ⁻²) or (Mn ^{III} Pc ⁻² / Mn ^{II} Pc ⁻²) or (Ti ^{III} Pc ⁻² / Ti ^{II} Pc ⁻²)	III (Co ^{III} Pc ⁻² / Co ^{II} Pc ⁻²) or (Mn ^{III} Pc ⁻¹ / Mn ^{III} Pc ⁻²) or (Ti ^{IV} Pc ⁻² / Ti ^{III} Pc ⁻²)	IV (Co ^{III} Pc ⁻¹ / Co ^{III} Pc ⁻²) (Ti ^{IV} Pc ⁻¹ / Ti ^{IV} Pc ⁻²)	V (Ti ^{IV} Pc ⁰ / Ti ^{IV} Pc ⁻¹)	NH₂
19 Co(II)	-1.58	-0.48	0.31	0.48	-	~1
20 Mn(III)	-1.06	-0.31	0.56	0.79 decomposition	-	1.05
21 Ti(IV)	~ -1.3	-0.84	-0.45	0.75	0.91	1.28

^a Central metals in brackets

3.2.1 Phenylthio derivatised phthalocyanines

3.2.1.1 CoPc derivatives (**12** and **13**)

Voltammetry

Figures 3.7(a) and (b) and 3.8(a) and (b) show the square wave and cyclic voltammograms of complexes **12** and **13** respectively on a wide (-1500 to + 1400 mV) potential window. Within this potential window two reductions and three oxidations are observed. Complex **12** shows redox processes at $E_{1/2} = -1.44$ V (**I**), -0.39 V (**II**), $+0.37$ V (**III**), $+0.78$ V (**IV**) and 1.15 V (**V**) versus Ag|AgCl, which are assigned as outlined in Table 3.2. Processes **I** and **II** are reversible with anodic to cathodic peak separation (ΔE) of 60 and 80 mV (ΔE value for the ferrocene standard was 85 mV), respectively, and the ratio of anodic to cathodic peak currents of near unity. Processes **III** and **IV** are quasi-reversible in that both had weak return peaks (even though ΔE for **III** was 60 mV). Process **V** was near the limits of the medium and electrode, hence is not well resolved. When a narrower scan window (between +1000 and -1000 mV) was employed for complex **12**, Figure 3.7(c) there was not much improvement in the reversibility of processes **III** and **IV**, confirming that observed behaviour was not due to the use of the limits of the system. Ring oxidation of alkylthio substituted MPc complexes often results in decomposition [122] hence the lack of reversibility of the oxidation processes was not surprising. Process **V** may be due to the oxidation of the thio substituents on the ring in addition to the ring itself.

For complex **13** the redox processes (Figure 3.8 (a) and (b)) were observed at $E_{1/2} = -1.42$ V (**I**), -0.57 , -0.39 V (**II**), $+0.27$ V (**III**), $+0.79$ V (**IV**) and $+1.10$ V (**V**) versus Ag|AgCl, which are assigned as outlined in Table 3.2. All processes were not completely

reversible in terms of both ΔE and the ratio of anodic to cathodic peak currents. In addition, process **II** showed a complicated behaviour consisting of overlapping peaks. Such behaviour is usually associated with aggregation in MPc complexes [33]. Using a narrower range, Figure 3.8(c), did not improve the behaviour of couple **II**, however the cathodic currents of process **III** improved.

The difference in the behaviour of the two complexes could be related to the fact that substitution at the non-peripheral positions prevents aggregation more than at the peripheral positions, hence complex **12** (non-peripherally substituted) shows less complicated behaviour than **13** (peripherally substituted). The effects of aggregation will be pronounced for cyclic voltammetry due to the high concentrations ($\sim 10^{-3}$ M) employed compared to UV-Visible spectra (Figure 3.2), where low concentrations ($\sim 1 \times 10^{-6}$ M) are used.

In terms of redox potentials, both **12** and **13** had the same potentials except for the ease of oxidation of **13** to $\text{Co}^{\text{III}}\text{Pc}$.

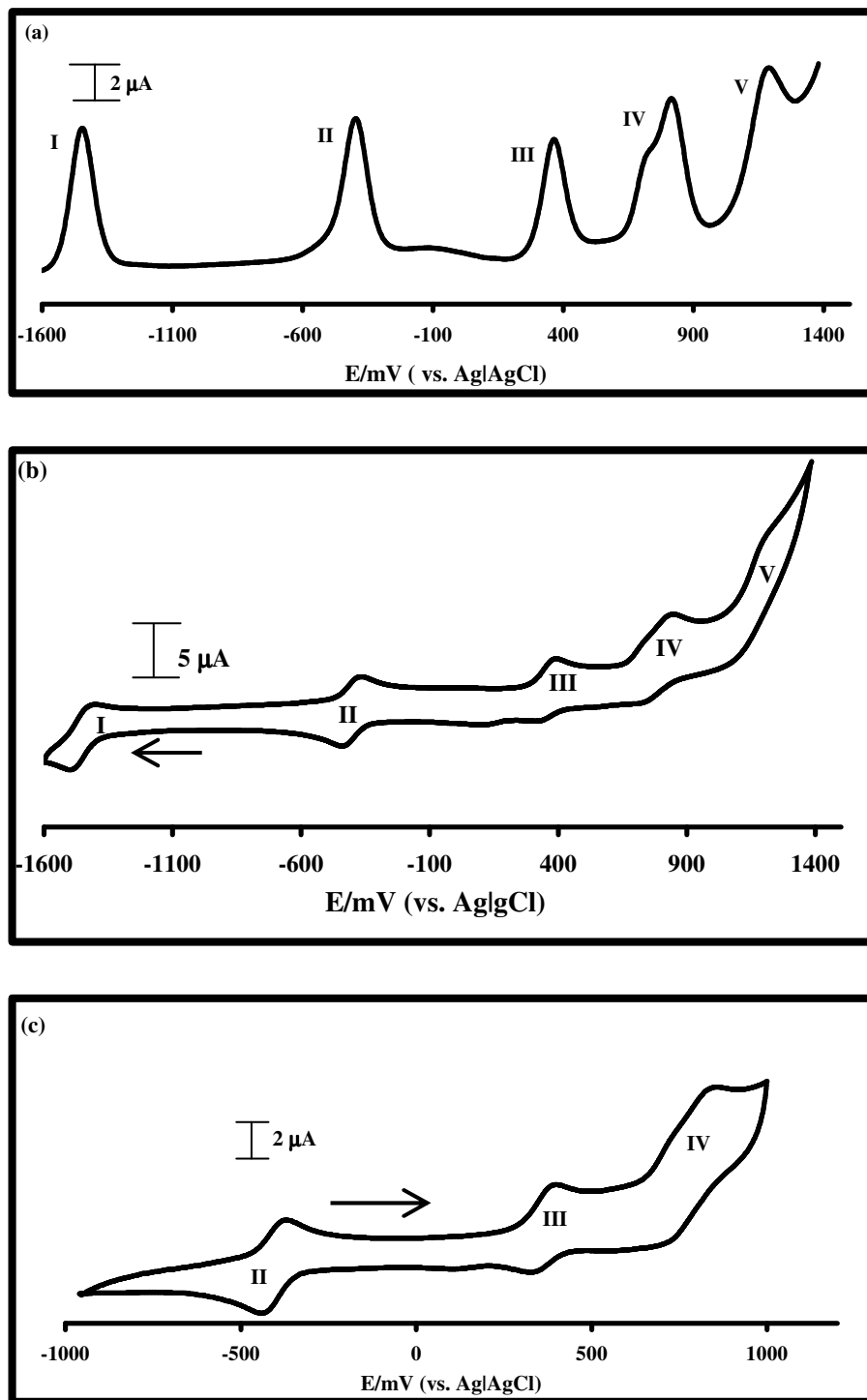


Figure 3. 7: Osteryoung square wave voltammogram (a) and cyclic voltammogram of complex **12** for a wide (b) and narrow (c) potential range in distilled DMF containing 0.1 M TBABF₄. Scan rate = 100 mVs⁻¹.

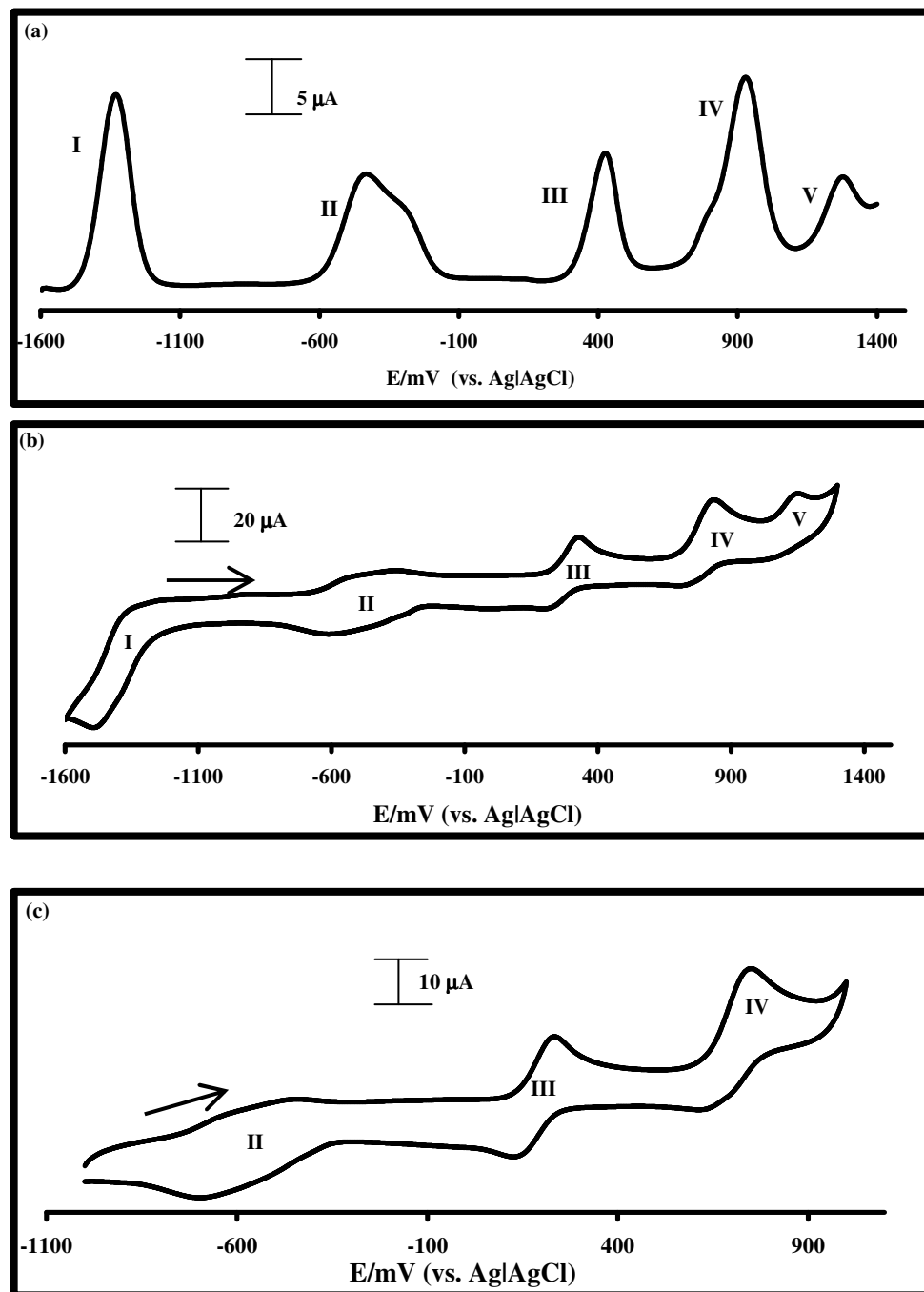


Figure 3. 8: Osteryoung square wave voltammogram (a) and cyclic voltammogram of complex **13** for a wide (b) and narrow (c) potential range in distilled DMF containing 0.1 M TBABF₄. Scan rate = 100 mVs⁻¹

Spectroelectrochemistry

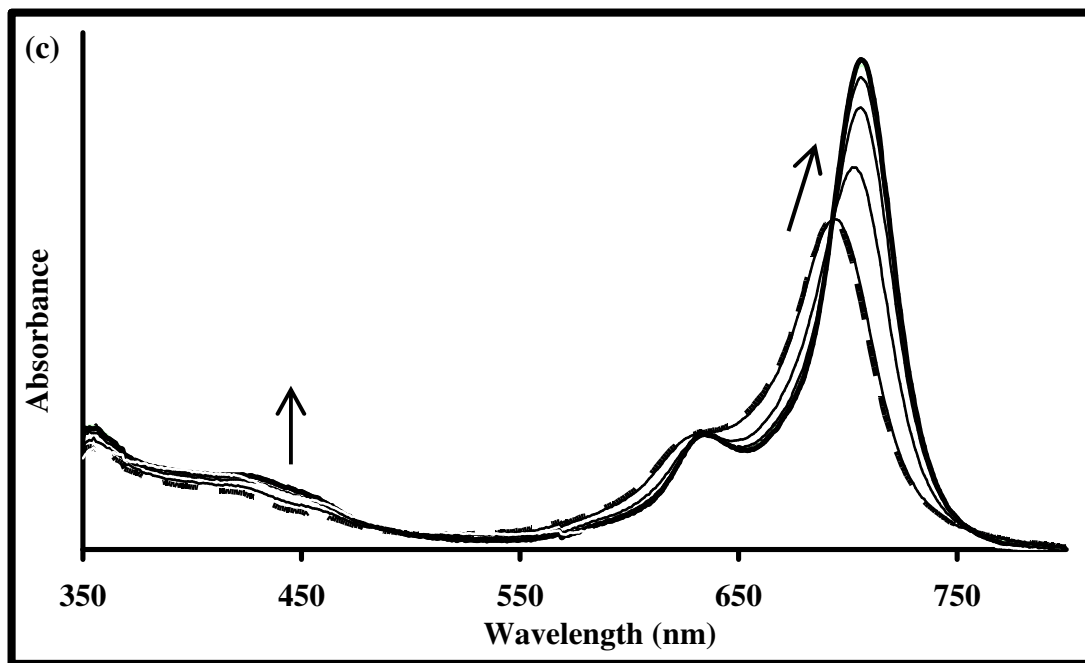
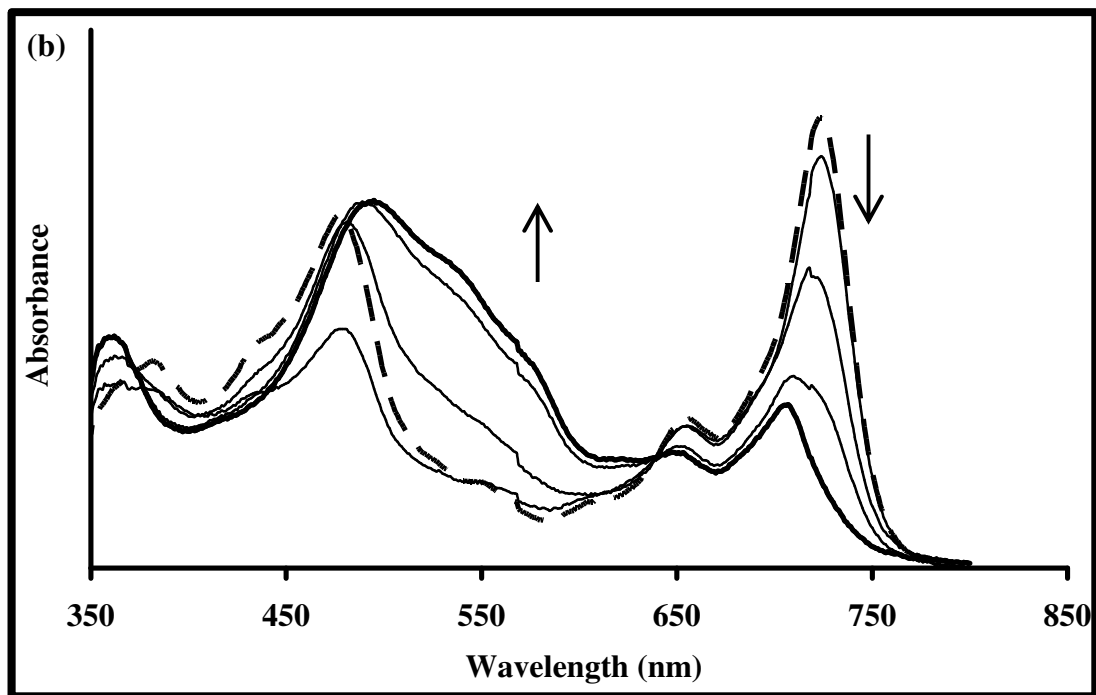
Spectroelectrochemistry was performed using an optically transparent thin layer electrode (OTTLE) cell in order to determine the nature of the redox processes occurring. Figure 3.9 (a) shows the spectral changes observed when the potential for couple **II** (complex **12**) was applied. There was a shift of the Q-band from 695 nm to 726 nm and a new band was formed near 482 nm. The latter band is characteristic of $\text{Co}^{\text{I}}\text{Pc}^{-2}$ complexes [23]. Thus the presence of this band coupled to the shifting of the Q-band to low energy, is typical behaviour for formation of $\text{Co}^{\text{I}}\text{Pc}^{-2}$ species [23]. Clear isosbestic points observed at 756 nm, 710 nm and 547 nm confirmed the presence of only two species. When the potential was increased to potentials for couple **I**, Figure 3.9 (b), there was a drastic decrease in Q-band absorbance at 726 nm with a simultaneous increase of absorption between 480 nm and 636 nm, typical of ring reduction in MPc complexes [32,38], forming $\text{Co}^{\text{I}}\text{Pc}^{-3}$. The absorption band at 482 nm shifted to 497 nm and the Soret band from 387 to 365 nm following the reduction at potentials of process **I**. An isosbestic point was observed at 636 nm. The original species could be completely regenerated upon application of 0 V following reduction at potential for couple **I** and **II**, confirming the reversible nature of the couples.

Oxidation of the complex at potentials of couple **III** Figure 3.9 (c) showed a shifting of the Q-band from 695 to 709 nm, with an isosbestic point at 693 nm. The shift in the Q band accompanied by an increase in intensity is typical behaviour [23] for the formation of the $\text{Co}^{\text{III}}\text{Pc}^{-2}$, thus couple **III** is assigned to $\text{Co}^{\text{III}}\text{Pc}^{-2}/\text{Co}^{\text{II}}\text{Pc}^{-2}$. Further oxidation at the potentials of process **IV** in Figure 3.9 (d) showed spectral changes typical of ring based processes, there was a large decrease in the absorbance of the Q-band with an isosbestic

point at 522 nm and a broad band near 500 nm typical [32, 38] of ring oxidation, hence confirming that process **IV** is due to $\text{Co}^{\text{II}}\text{Pc}^{-2}/\text{Co}^{\text{II}}\text{Pc}^{-1}$. The regeneration of original species (~50%) could be observed by reversal of the applied potential for couple **IV**, confirming the lack of complete reversibility of this process. Applications of potentials of process **V** continued the degradation process. For all processes for complex **12**, the number of electrons transferred was calculated using the equation $Q = nFVC$ and n was found to be close to one.

Spectroelectrochemical studies on complex **13** were also carried out in order to assign the cyclic voltammetry peaks. Reduction at potentials of couple **II** resulted in lowering in intensity and a hypsochromic shift of the Q-band from 673 nm to 711 nm Figure 3.10 (a) with a simultaneous increase of the band at 478 nm. These spectral changes are typical of the formation of $\text{Co}^{\text{I}}\text{Pc}^{-2}$ as discussed above for complex **12**. Isosbestic points were observed at 693 nm, 568 nm and 399 nm. The spectra could be regenerated to ~80% on potential reversal following application of potential for couples **II**. On application of potential for couple **I**, (figure not shown), there was a decrease in Q-band absorption intensity and an increase in absorption in the 500 nm region, as observed above for complex **12**, typical [38] of ring-based reduction process ($\text{Co}^{\text{I}}\text{Pc}^{-2}/\text{Co}^{\text{I}}\text{Pc}^{-3}$). When the potential for process **III** was applied, Figure 3.10 (b), a gradual red shifting of the Q-band from 673 nm to 686 nm with increasing intensity occurred. Isosbestic points were observed at 507 nm and 681 nm, these spectral changes confirm a metal based oxidation process to form the $\text{Co}^{\text{III}}\text{Pc}^{-2}$ species. Increasing the potential to values of couple **IV**, Figure 3.10 (c), resulted in a considerable decrease in Q-band absorption with a slight increase in absorption at the 500 nm region, an isosbestic point was observed at 530 nm.

The weakness of the peak in the 500 nm region shows possible degradation of the complex. The spectra could be regenerated to ~50% on potential reversal following application of potential for couple **IV**, showing the lack of complete reversibility of this process observed in the cyclic voltammogram. Again applications of potentials of process **V** continued the degradation process.



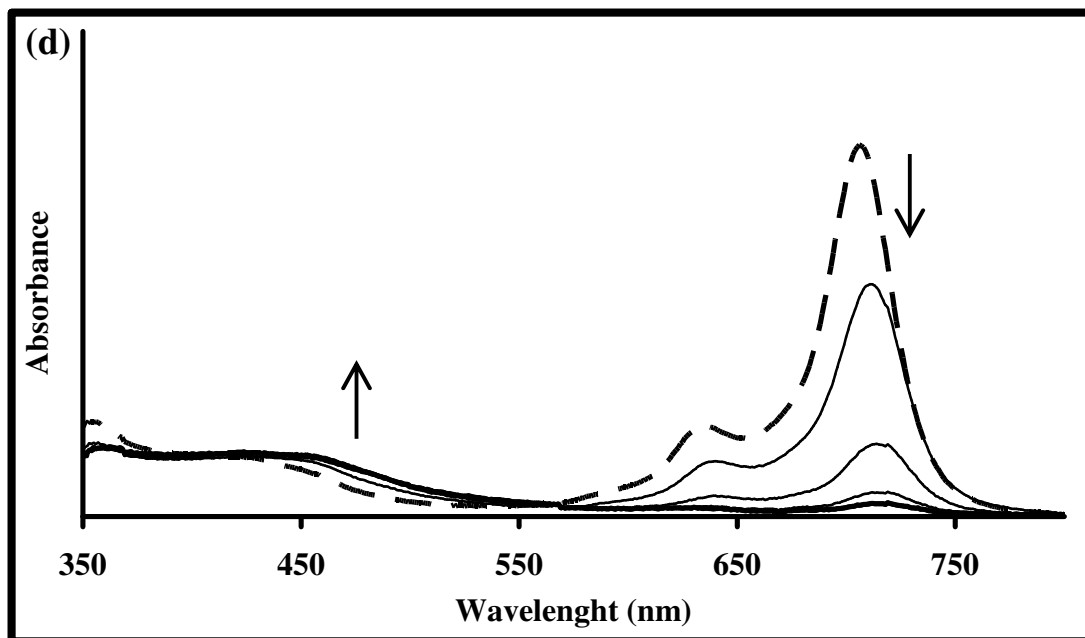
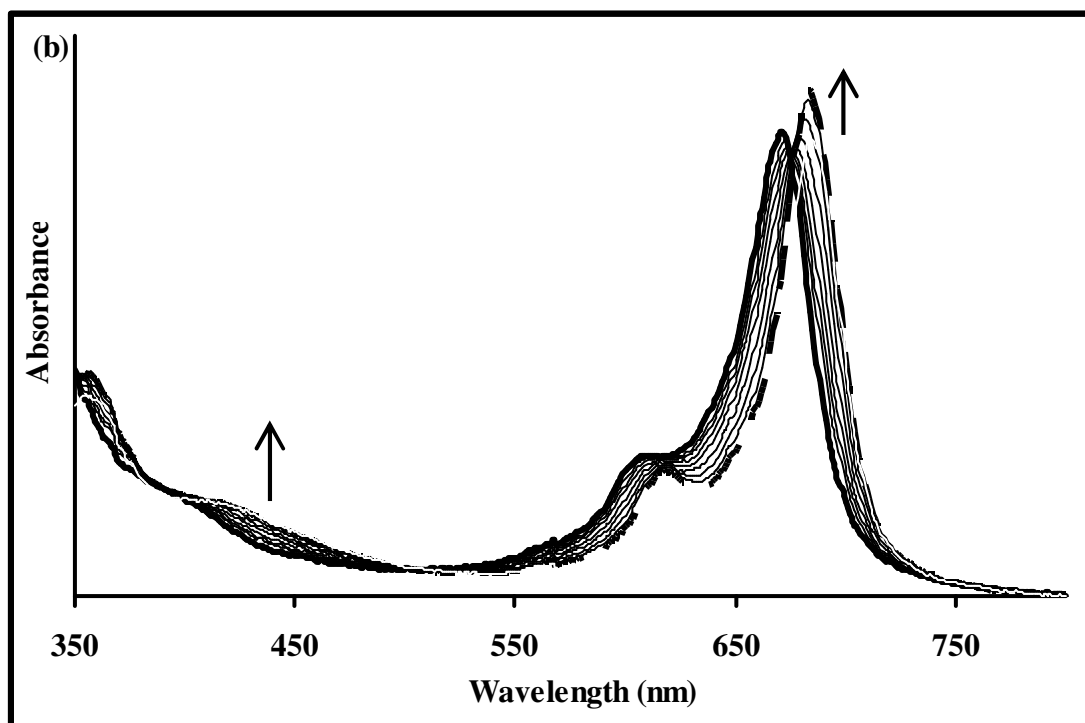
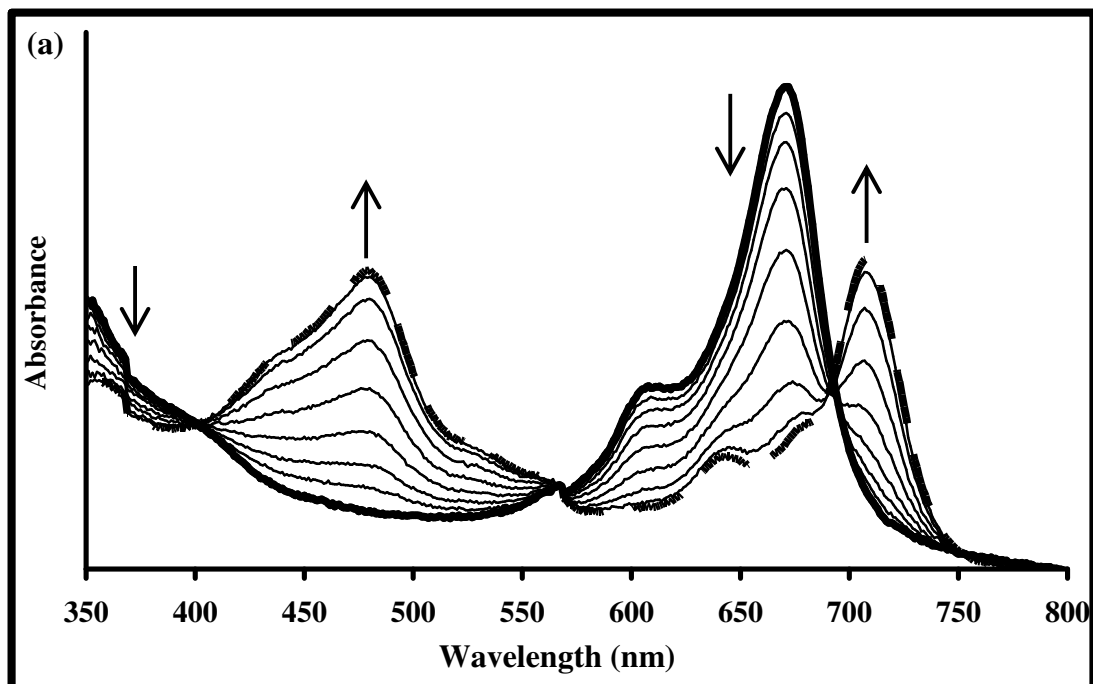


Figure 3. 9: UV/Vis/NIR spectral changes of complex **12** in DMF containing 0.1 M TBABF₄ observed during application of controlled potential at potentials of the following processes; (a) **II** (-0.5 V), (b) **I** (-1.5 V), (c) **III** (+0.4 V) and (d) **IV** (+0.8 V). The first scan in (b) is the same as the last scan in (a). The first scan in (d) is the same as the last scan in (c).



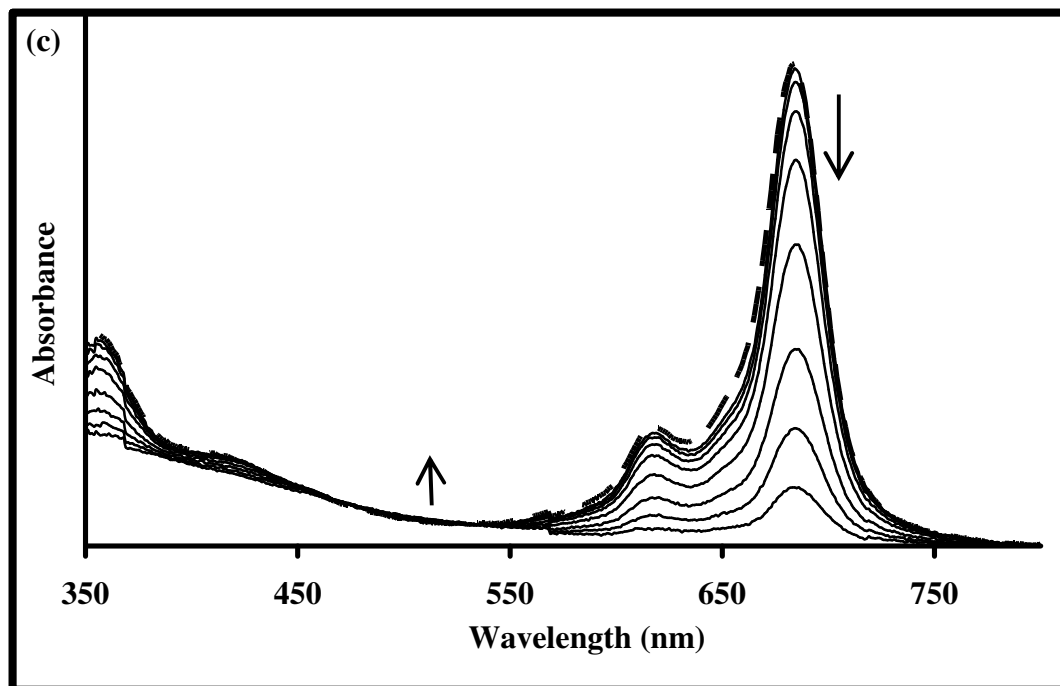


Figure 3. 10: UV/Vis/NIR spectral changes of complex **13** in DMF containing 0.1 M TBABF₄ observed during application of controlled potential at potentials of the following processes; (a) **II**(-0.6 V), (b) **III** (+0.4 V) and (c) **IV**(+0.8 V). The first scan in (c) is the same as the last scan in (b).

Based on the cyclic voltammetry and spectroelectrochemistry data, the redox processes (**I-IV**) for both complexes (**12** and **13**) are assigned as shown on equations 3.1-3.4:



3.2.1.2 MnPc derivatives (14)

Voltammetry

Voltammetry experiments of complex **14** were performed in deaerated DMF containing 0.1 M TBABF₄ as electrolyte, and the data is given in Table 3.2. Figure 3.11(a) shows the square wave voltammogram and Figure 3.11 (b) shows the cyclic voltammogram. The complex exhibited three reduction processes at $E_{1/2} = -1.37\text{V}$ (**I**), -0.76V (**II**), -0.057V (**III**) and one weak oxidation process labeled **IV** at $\sim 0.88\text{V}$. Couples **I** and **III** were quasi reversible with ΔE values of 101mV and 111mV respectively. Couple **III** was reversible with a ΔE value of 81mV (ΔE value for the ferrocene standard was 85 mV). The I_{pc}/I_{pa} ratios were near unity for process **I** to **III**. Process **IV** was too weak to be analysed reliably.

Compared to **12** and **13**, **14** is more difficult to reduce from Mn^{II} to Mn^{I} , Table 3.2.

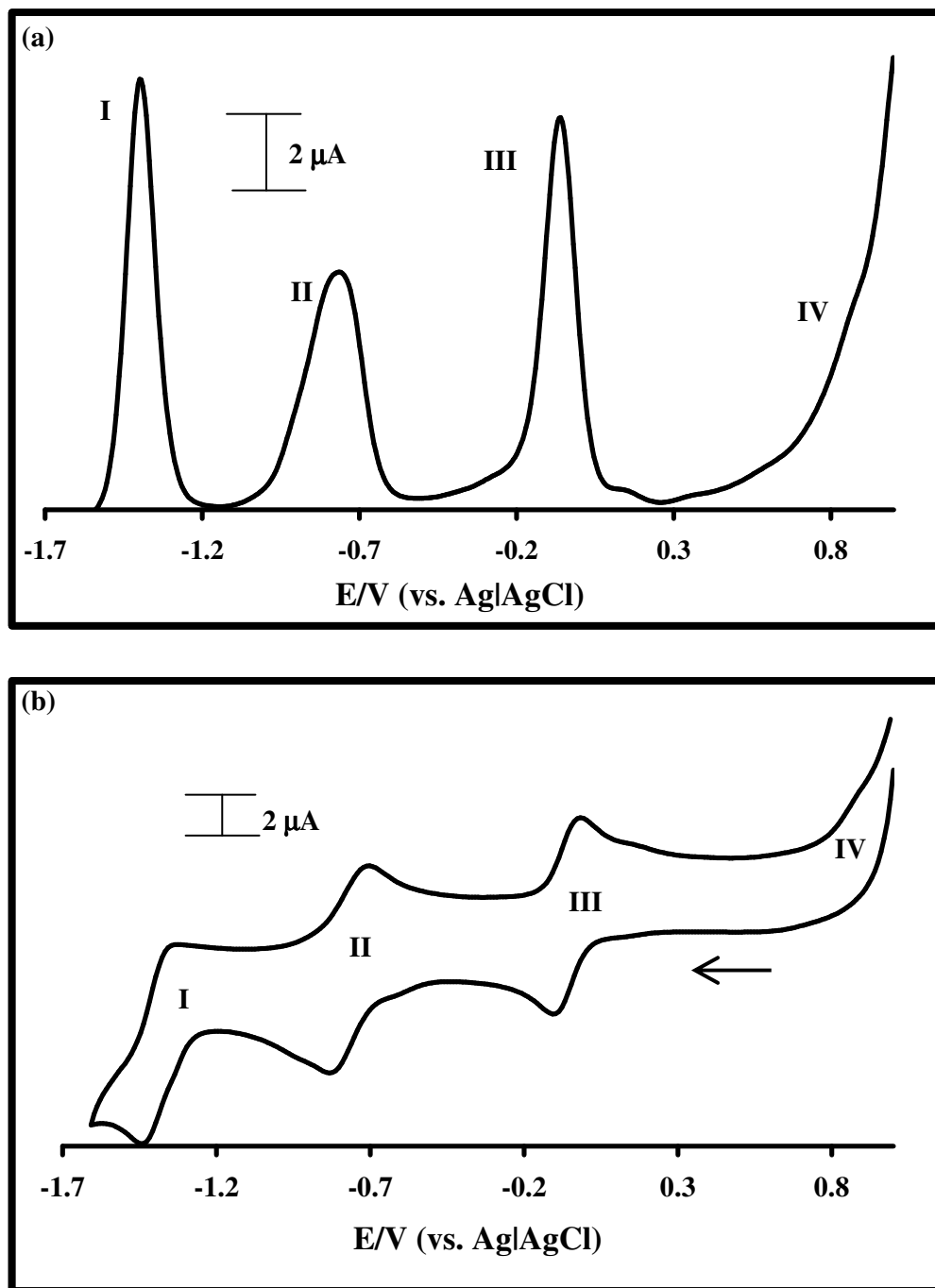
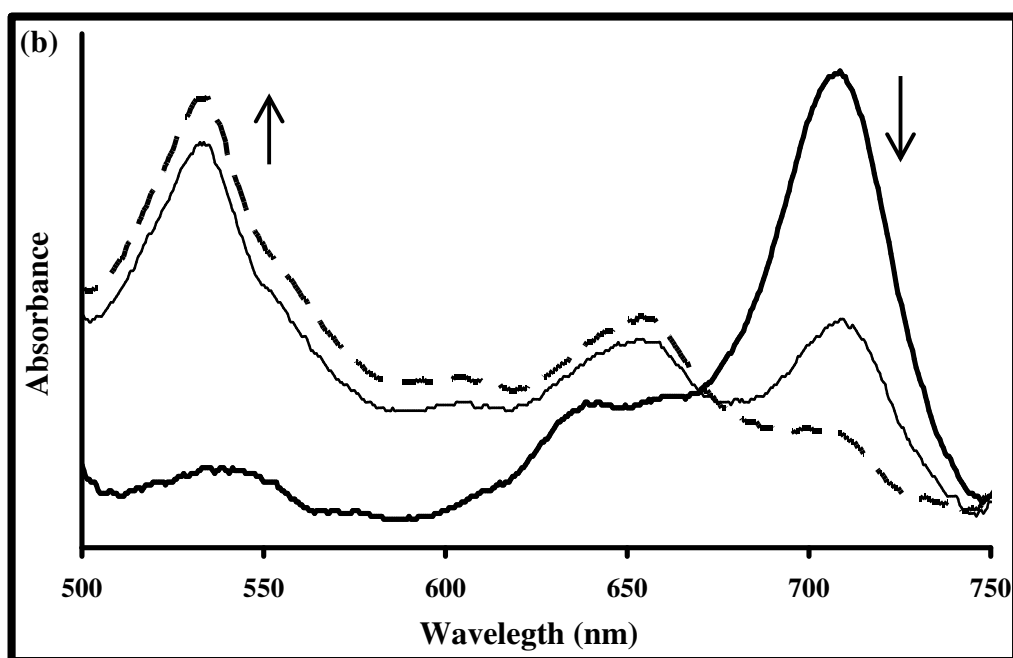
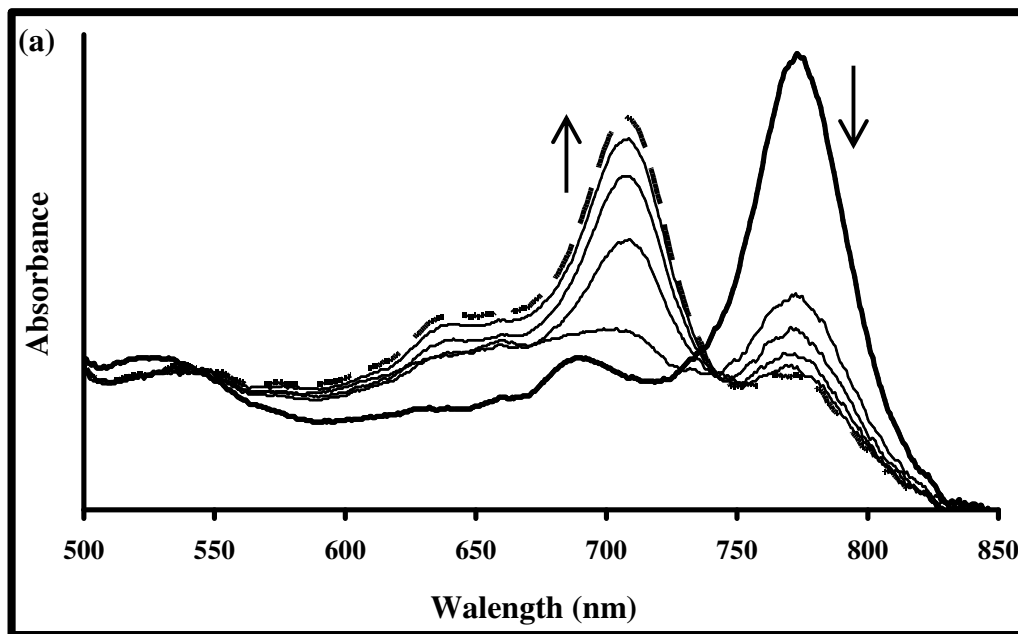


Figure 3. 11: (a): Osteryoung square wave voltammogram and (b) cyclic voltammogram of complex 14 in distilled DMF containing 0.1 M TBABF₄. Scan rate = 100 mVs⁻¹.

Spectroelectrochemistry

Figure 3.12 (a) shows the spectral changes observed during the reduction of **14** at potentials of process **III**. The Q-band shifted from 770 to 708 nm with a diffuse isosbestic point at 742 nm. The lack of a clear isosbestic point could be due to exchange of axial ligands to electrolyte ligands. The spectral changes in Figure 3.12(a) are due to $\text{Mn}^{\text{III}}\text{Pc}^{-2}$ to $\text{Mn}^{\text{II}}\text{Pc}^{-2}$ reduction [23]. The potential applied was increased to potentials of process **II**, and Figure 3.12 (b) shows the spectral changes observed. The Q-band at 708 nm decreased in intensity and a new band was observed at 654 nm with a simultaneous increase in intensity in the 500-600 nm region, and an isosbestic point at 672 nm. The sharp peak at 534 nm is typical of $\text{Mn}^{\text{I}}\text{Pc}$ species [123]. Thus process **II** was assigned to the $\text{Mn}^{\text{II}}\text{Pc}^{-2}$ to $\text{Mn}^{\text{I}}\text{Pc}^{-2}$ process. Reduction at potentials of process **III** resulted in very short lived spectral changes shown in Figure 3.12 (c). The peak at 654 nm shifted to 660 nm, while decreasing in intensity and the peak at 543 nm also decreased in intensity. The 708 nm peak increased. The decrease in intensity of peaks is typical of ring based processes [38], the changes are assigned to $\text{Mn}^{\text{I}}\text{Pc}^{-3}$ formation. There was no regeneration of the original spectra. A reduction at this potential is at the limits of the electrodes-electrolyte systems.



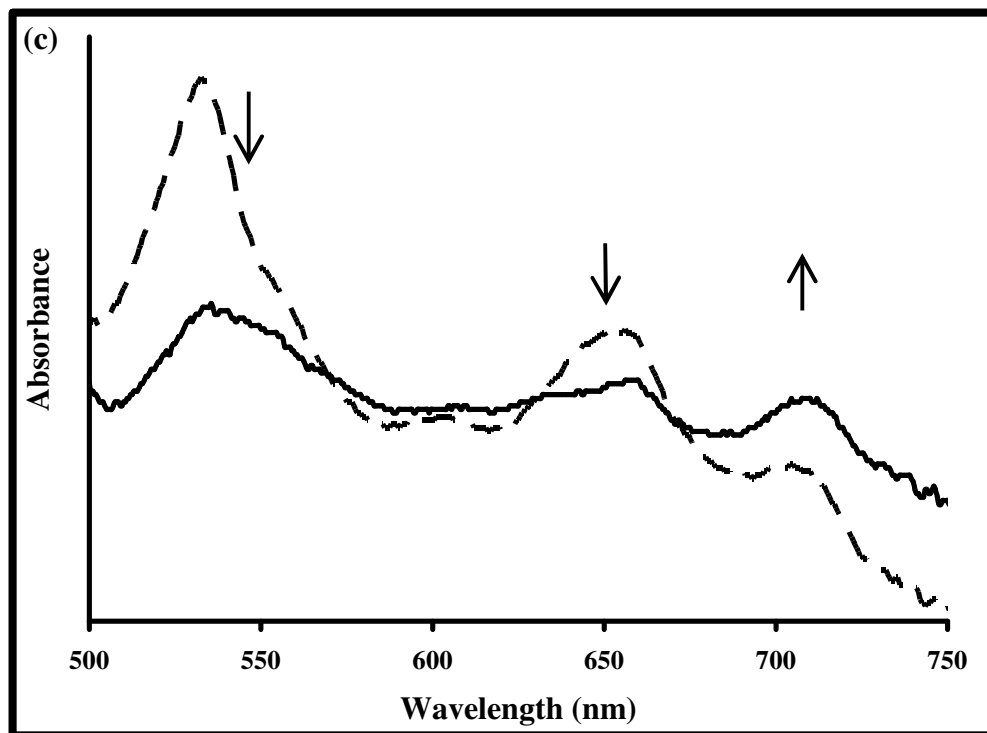


Figure 3. 12: UV/Vis/NIR spectral changes of complex **14** in DMF containing 0.1 M TBABF₄ observed during application of controlled potential at potentials of the following processes; (a) **III**(-0.3 V), (b) **II** (-1 V) and (c) **I** (- 1.7 V). The first scan in (b) is the same as the last scan in (a), the first scan in (c) is the same as the last scan in (b).

Based on the cyclic voltammetry and spectroelectrochemistry data, complex **14** redox processes (**I-III**) are assigned as shown on equations 3.5-3.7.



The formation of $\text{Mn}^{\text{I}}\text{Pc}^{-2}$ rather than $\text{Mn}^{\text{II}}\text{Pc}^{-3}$ has been a subject of controversy with most reports being on the formation of $\text{Mn}^{\text{II}}\text{Pc}^{-3}$. This work is one of the few examples of $\text{Mn}^{\text{I}}\text{Pc}^{-2}$ species formation [123].

3.2.2 Amino-derivatised phthalocyanines

3.2.2.1 CoTAPc (**19**)

Voltammetry

Cyclic (Figure 3.13(b) and (c)) and square wave (Figure 3.13(a)) voltammetric studies were carried out in deaerated distilled DMF solution containing complex **19** and 0.1 M TBABF₄ as the supporting electrolyte to understand the electrochemical behavior of the complex in solution. In Figure 3.13(b) shows the CV scan of complex **19** was carried out between -1.9V and 1.5V. The weak CVs are typical of MTAPc derivatives, but SWV shows well resolved peaks [45, 46]. Weak redox processes have also been observed for the β substituted CoTAPc [130]. Two reduction redox peaks were observed with formal potentials at -1.58V (**I**) and -0.48V (**II**) respectively. Process **I** and **II** were both quasi-reversible with anodic to cathodic current ratios which deviated from unity. Process **I** is at the limits of the system but is still clear. Oxidation redox processes were extremely weak and occurred at 0.31V (**III**), 0.48V (**IV**) and ~ 1 V (**NH₂**). The NH₂ oxidation has been reported at 1V [46, 62]. Figure 3.13(c) shows the oxidation redox process at a narrow range with no improvement. Comparing Tables 3.2 and 3.3 shows that **19** containing NH₂ at the non-peripheral position is easier to oxidize and more difficult to reduce than **12** containing thiophenyl groups also at the α positions, due to more electron donating ability of the NH₂ group group.

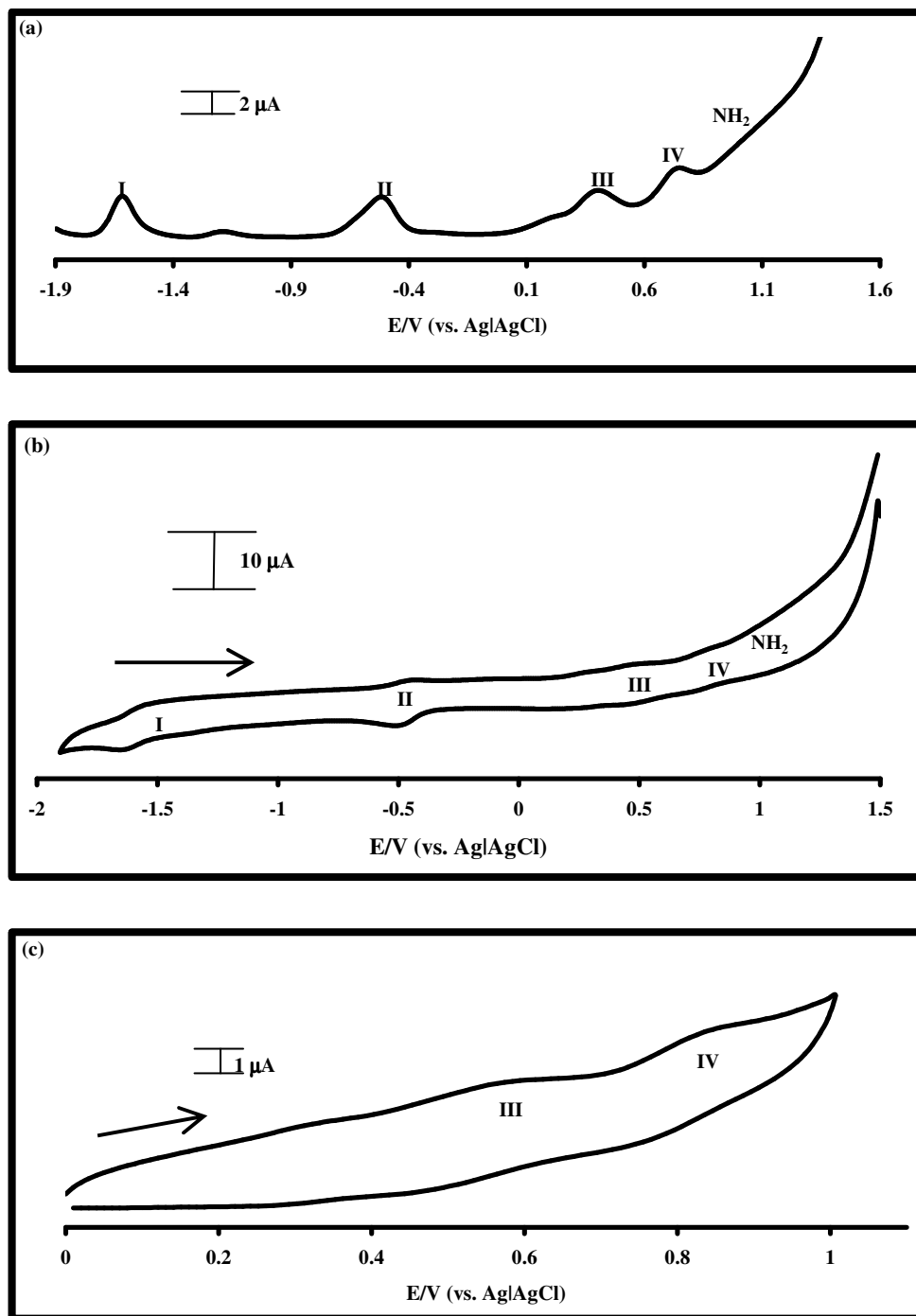


Figure 3. 13: Osteryoung square wave voltammogram (a) and cyclic voltammogram of complex **19** at a wide (b) and narrow (c) potential range in distilled DMF containing 0.1 M TBABF₄. Scan rate = 100 mVs⁻¹.

Spectroelectrochemistry

Figure 3.14 (a) shows spectral changes observed when potentials of process **II** was applied, there was a 16 nm shift of the Q-band from 749 to 765 nm typical of $\text{Co}^{\text{I}}\text{Pc}$ species. There was an increase in absorption between 450 nm and 550 nm also typical of $\text{Co}^{\text{I}}\text{Pc}$ species thus process **II** was assigned to $\text{Co}^{\text{II}}\text{Pc}^{-2}$ to $\text{Co}^{\text{I}}\text{Pc}^{-2}$ process. An increase in reduction potential to potentials of process **I** shown in Figure 3.14(b) resulted in the Q-band collapsing with a simultaneous decrease in the 500-600 nm region and an isosbestic point at 629 nm. Process **I** was assigned to the $\text{Co}^{\text{I}}\text{Pc}^{-2}$ to $\text{Co}^{\text{I}}\text{Pc}^{-3}$ process. There was a 34% regeneration of the original peak in Figure 3.14 (a) when 0 V was applied confirming the processes lack of total reversibility.

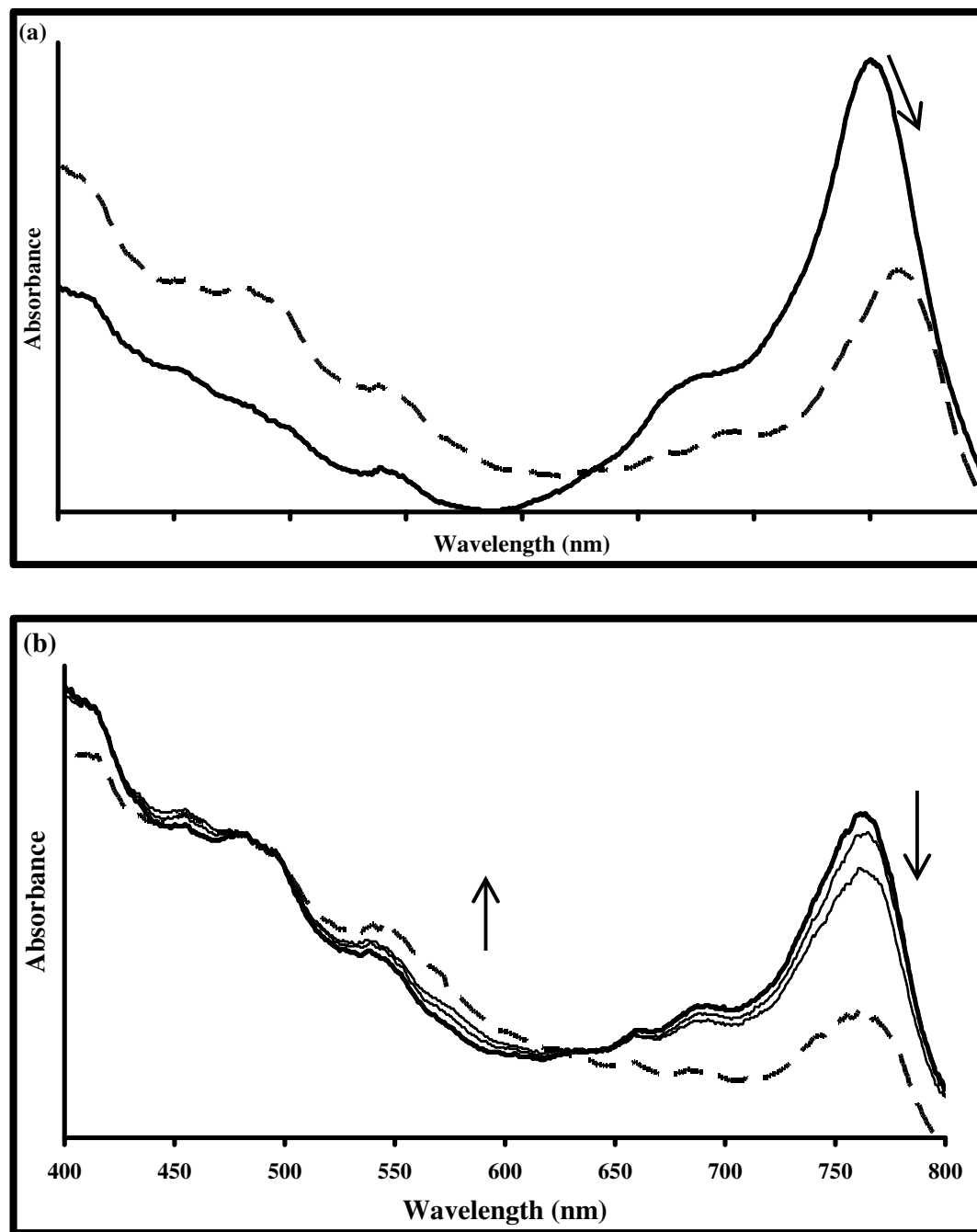


Figure 3. 14: UV/Vis/NIR spectral changes of complex **14** in DMF containing 0.1 M TBABF₄ observed during application of controlled potential at potentials of the following processes; (a) **II** (-0.8 V) and (b) **I** (-1.8 V) . The first scan in (b) is the same as the last scan in (a).

Based on the cyclic voltammetry and spectroelectrochemistry and comparing with literature [33], assignments for **19** are the same for **12** and **13**.

3.2.2.2 (OH)MnTAPc (**20**)

Voltammetry

The electrochemical properties of the peripherally substituted (OH)MnTAPc have been reported [46]. The square wave and cyclic voltammograms (Figure 3.15(a) and (b)) of complex **20**, were obtained in deaerated DMF containing TBABF₄ as electrolyte. Within the potential window in Figure 3.15, two reduction processes (labelled **I** and **II**) and three oxidation processes (labelled **III**, **IV** and **NH₂**) were observed. The redox processes are weak as was observed [46] for peripherally substituted (OH)MnTAPc. When a narrower scan window was employed in Figure 3.15(c), there was not much improvement in the reversibility of processes **III** and **IV**. Couple **II** was well-resolved and reversible with anodic to cathodic peak separation (ΔE) of 70 mV. The second reduction process (**I**) showed overlapping bands, and the peak labelled **I*** which may be related to aggregation, due to the concentrations employed for the voltammetric studies. This peak disappeared on dilution of the solution.

The redox potentials were observed at: $E_{1/2} = -0.31$ V (**I**), $E_{1/2} = -1.06$ V (**II**), $E_{1/2} = 0.56$ V (**III**), $E_{1/2} = 0.79$ V (**IV**) and $E_p = 1.05$ V (**NH₂**) vs. Ag|AgCl. In comparison with peripherally substituted (OH)MnTAPc and other MnPc complexes [46], the reduction processes **II** and **I** in Figure 3.15(a) are assigned to metal ($\text{Mn}^{\text{III}}\text{Pc}^{-2}/\text{Mn}^{\text{II}}\text{Pc}^{-2}$) and ring ($\text{Mn}^{\text{II}}\text{Pc}^{-2}/\text{Mn}^{\text{II}}\text{Pc}^{-3}$) reductions, respectively. Spectroelectrochemical experiments below were employed to further confirm the identities of the redox processes in Figure 3.15.

Oxidation processes **III** and **IV** are respectively in the range of metal $\text{Mn}^{\text{IV}}\text{Pc}^{-2}/\text{Mn}^{\text{III}}\text{Pc}^{-2}$ and ring-based ($\text{Mn}^{\text{IV}}\text{Pc}^{-2}/\text{Mn}^{\text{IV}}\text{Pc}^{-1}$) oxidations in comparison with peripherally substituted (OH)MnTAPc. However as will be discussed below, spectroelectrochemistry did not show evidence of metal oxidation. The amino group oxidation was observed at ~ 1.05 V vs. Ag|AgCl, which is within the range of the reported tetraamino substituted metallophthalocyanine complexes [46,61].

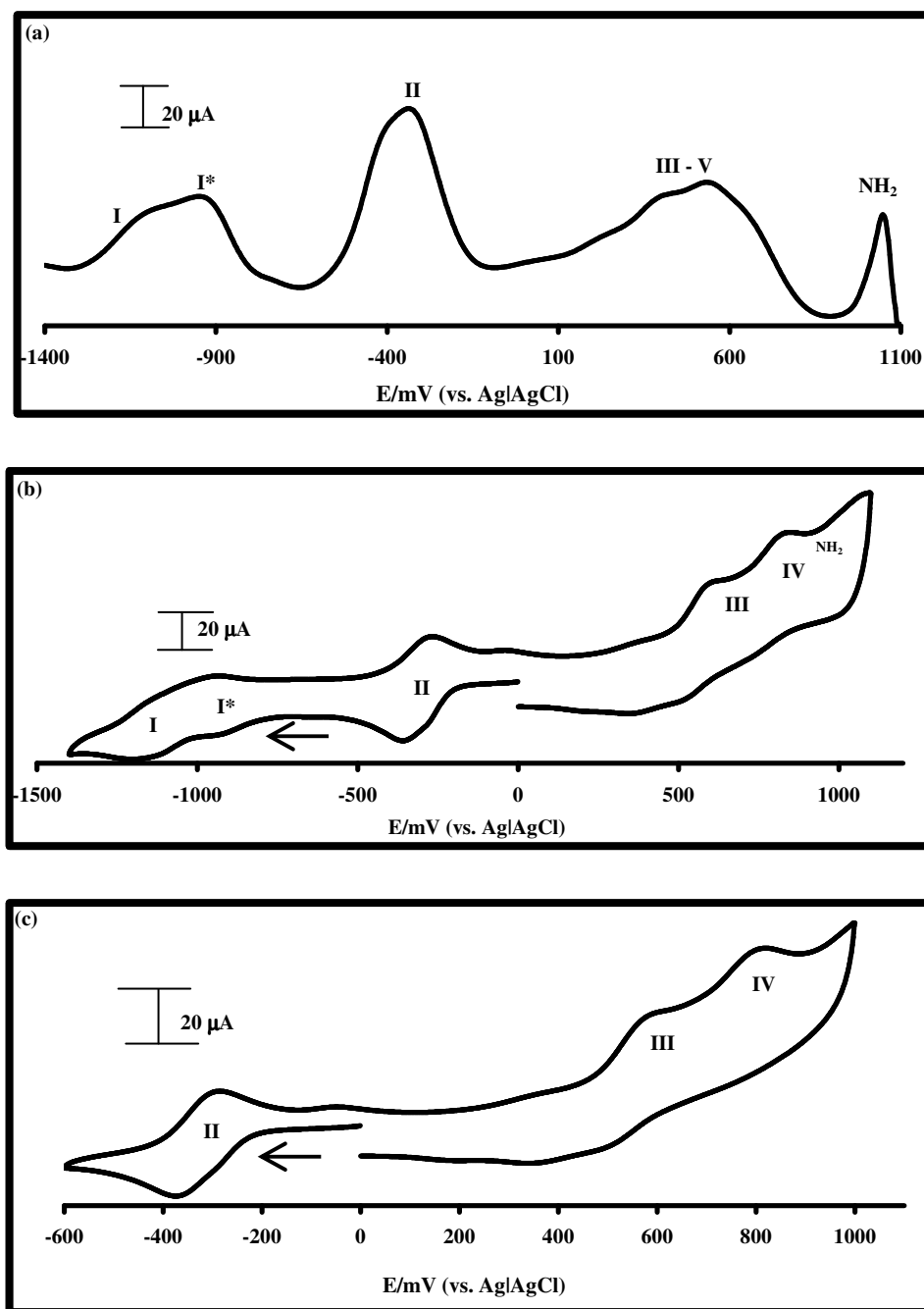


Figure 3. 15: Osteryoung square wave voltammogram (a) and cyclic voltammogram of complex **20** in distilled DMF containing 0.1 M TBABF₄ at a wide (b) and narrow (c) potential range. Scan rate = 100 mVs⁻¹.

Spectroelectrochemistry

The nature of the processes in Figure 3.15 for complex **20** were further probed by spectroelectrochemistry using the optically transparent thin-layer electrode (OTTLE) cell. The reduction at potentials of process **II** resulted in the spectral changes observed in Figure 3.16(a) which consisted of a bathochromic shift of the Q-band from 871 to 762 nm. The 109 nm shift in Q-band on reduction is much larger than that observed for reduction the peripherally substituted (OH)MnTAPc complex, i.e. 70 nm [46]. Simultaneously, the charge transfer band at 547 nm gradually disappeared and was replaced by a broad band near 450 nm. Moreover, the MPc solution colour changed from purple to deep green. Clear isosbestic points were observed at 809, 624, 484 and 423 nm, further suggesting that only two species are present during the electroreduction of the MPc. These spectral changes are typical of a metal-based reduction in MPc complexes in general, and for MnPc complexes in particular [46], and consist of a Q-band shift without much change in intensity [23], and thus are consistent with the metal reduction from $\text{Mn}^{\text{III}}\text{Pc}^{-2}$ to $\text{Mn}^{\text{II}}\text{Pc}^{-2}$. Coulometry confirmed that the number of electrons transferred was ~ 1 .

Further reduction at potentials of process **I** resulted in the decrease in the Q-band (at 762 nm) intensity which was accompanied by an increase in intensity in the 450 and 650 nm region, Figure 3.16(b). These spectral changes are typical of a ring-based process in MPcs and therefore suggest reduction of $\text{Mn}^{\text{II}}\text{Pc}^{-2}$ to $\text{Mn}^{\text{II}}\text{Pc}^{-3}$ [38]. Reduction of $\text{Mn}^{\text{II}}\text{Pc}^{-2}$ to $\text{Mn}^{\text{I}}\text{Pc}^{-2}$ has been reported [23], however for MnTAPc and for other MnPc complexes [46] reduction of $\text{Mn}^{\text{II}}\text{Pc}^{-2}$ to $\text{Mn}^{\text{II}}\text{Pc}^{-3}$ has been observed. The above assignments are different from those proposed for **14** in that $\text{Mn}^{\text{II}}\text{Pc}^{-2}$ reduction leads to $\text{Mn}^{\text{II}}\text{Pc}^{-3}$ for **20**

and $\text{Mn}^{\text{I}}\text{Pc}^{-2}$ for **14** showing that the reduction process is dependant on the ring substituent. Tables 3.2 and 3.3 show that the first reduction for **20** occurs at less negative values than the reduction in **14** and as reported before [123]. The formation of $\text{Mn}^{\text{II}}\text{Pc}^{-3}$ occurs when reduction is easy [123].

Oxidation of process **III** resulted in the spectral changes observed in Figure 3.16(c), which consisted of a decrease in the Q-band intensity with simultaneous increase in the intensity in the 500 to 600 nm region. The spectral changes are typical of a ring-based oxidation process and thus confirm the oxidation of $\text{Mn}^{\text{III}}\text{Pc}^{-2}$ to $\text{Mn}^{\text{III}}\text{Pc}^{-1}$. There was no evidence of $\text{Mn}^{\text{IV}}\text{Pc}$ formation reported before for other MnPc complexes [36, 47]. As with reduction of $\text{Mn}^{\text{II}}\text{Pc}^{-2}$, discussed above the observation of metal oxidation in $\text{Mn}^{\text{III}}\text{Pc}$ (to $\text{Mn}^{\text{IV}}\text{Pc}$) complexes seems to be dependent on ring substituents and the position of substitution (peripheral versus non-peripheral). Further oxidation at the potential of process **IV** degraded the MPc as judged by Q band diminishing without formation of any new bands. But this process is expected to be due to further ring oxidation and the formation of $\text{Mn}^{\text{III}}\text{Pc}^0$.

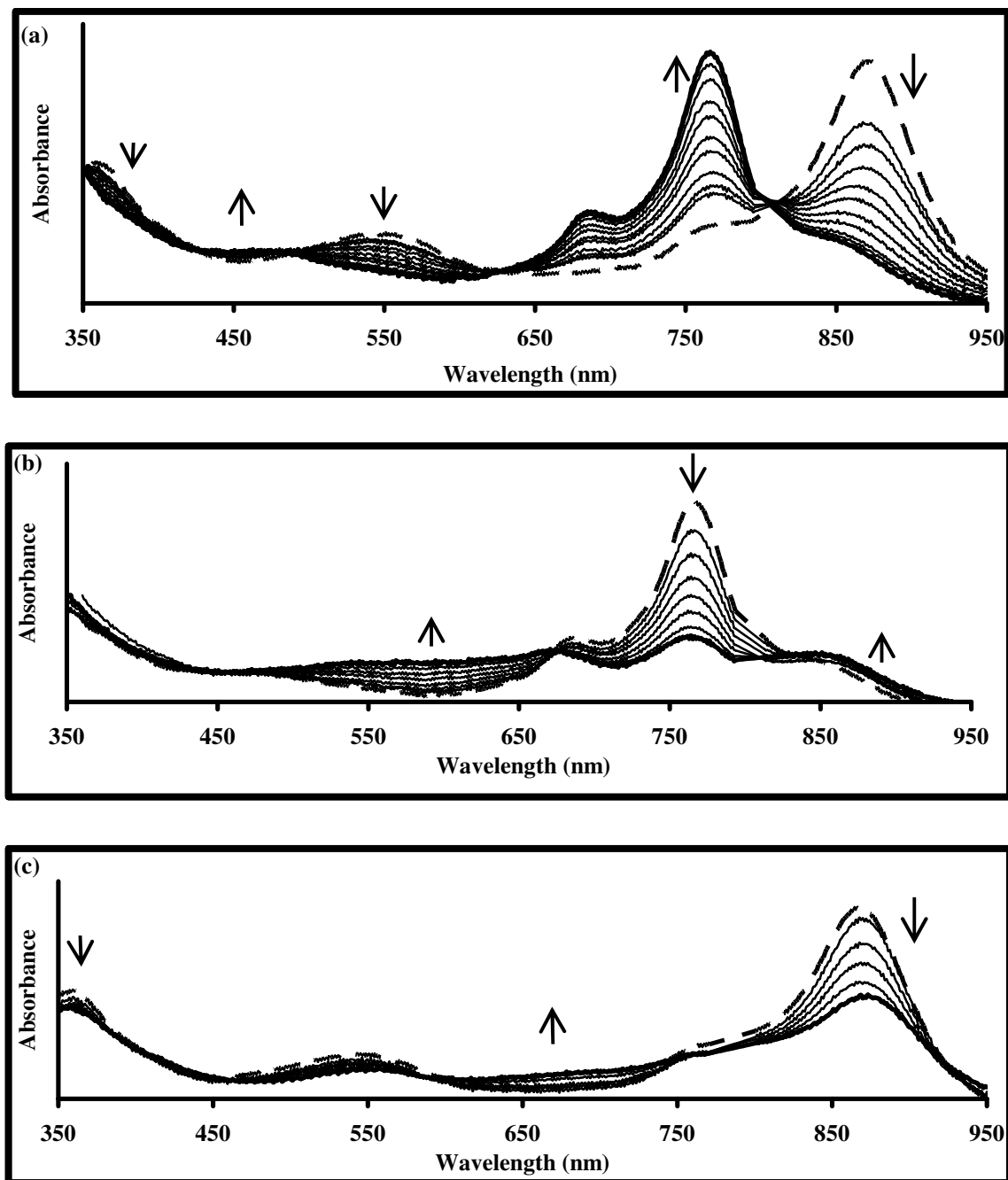


Figure 3. 16: UV/Vis/NIR spectral changes of complex **20** in DMF containing 0.1 M TBABF₄ observed during application of controlled potential at potentials of the following processes; (a) **II** (-0.6 V), (b) **I** (-1.5 V) and (c) **III** (0.7 V). The first scan in (b) is the same as the last scan in (a).

Based on the electrochemistry data obtained and discussed above, the following mechanism for the reduction and oxidation of the non-peripherally substituted (OH)MnTAPc is proposed, eqs. 3.8 –3.11:



3.2.2.3 OTiTAPc (21)

Figure 3.17(a) and (b) shows the square wave and cyclic voltammograms of complex **21** in deaerated DMF containing 0.1 M TBABF₄. Reversible reduction couples labelled **III** and **II** were observed at -0.45 V and -0.84 V (vs. Ag|AgCl) and are assigned to Ti^{IV}Pc⁻²/Ti^{III}Pc⁻² and Ti^{III}Pc⁻²/Ti^{II}Pc⁻² respectively in comparison with peripherally substituted OTiTAPc [48]. A further reduction peak labelled **I** was observed at -1.3 V vs. Ag|AgCl, and is attributed to the first ring reduction (Ti^{II}Pc⁻²/Ti^{II}Pc⁻³). Two ill-defined oxidation processes labelled **IV** and **V** are observed at ~ 0.8V and 0.9V (overlapping processes) vs. Ag|AgCl are respectively attributed to Ti^{IV}Pc⁻¹/Ti^{IV}Pc⁻² (in comparison with peripherally substituted OTiTAPc) and Ti^{IV}Pc⁰/Ti^{IV}Pc⁻¹. The last peak is in the range for NH₂ oxidation. Ill-defined oxidation processes were also observed for peripherally substituted TiTAPc [48]. The electrochemistry of TiPc derivatives is highly dependent on the substituents. The overlap of voltammograms for tetraphenoxy substituted TiPc, whereby two 1-electron reductions resulted in one couple has been reported [124].

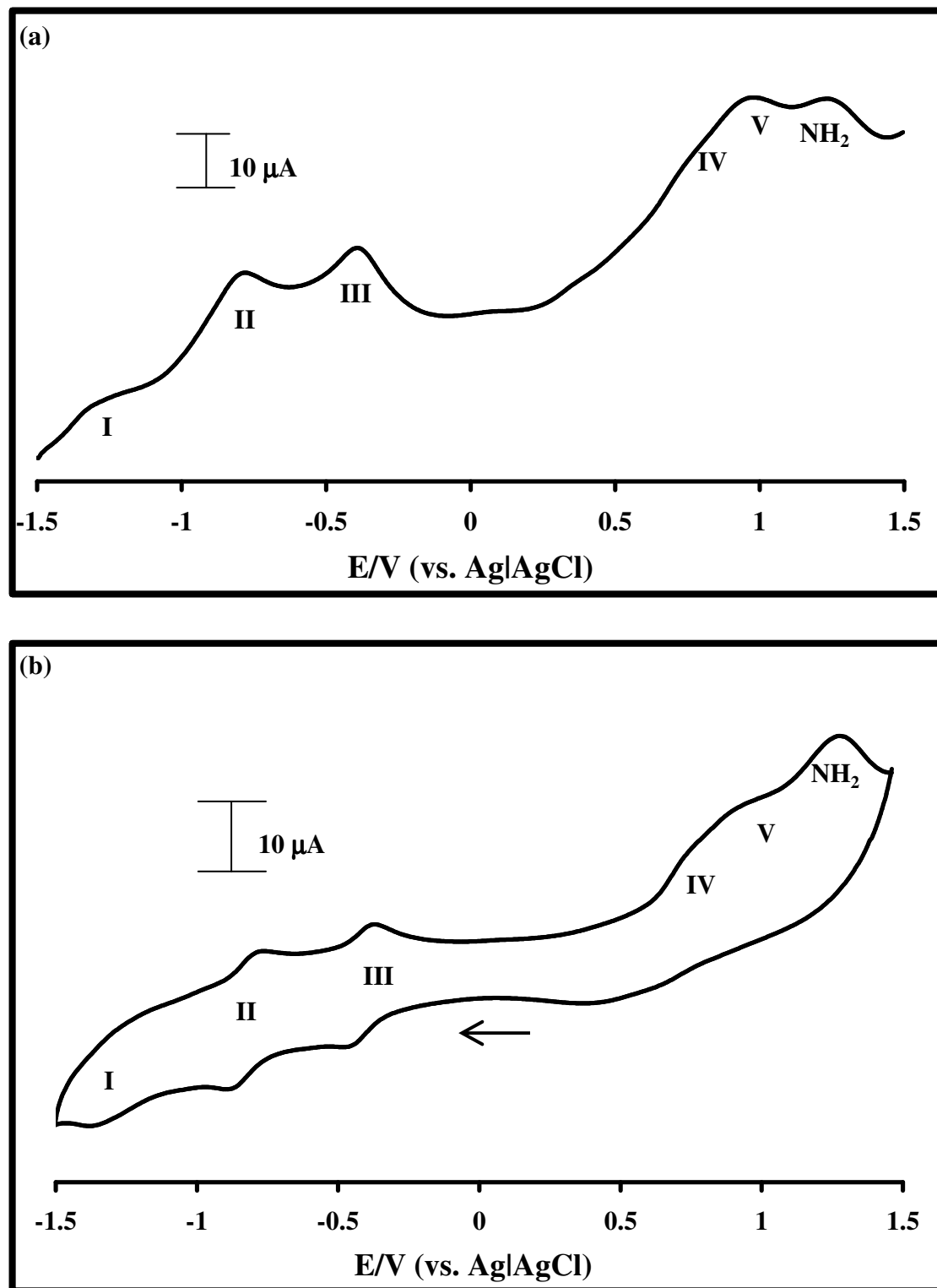


Figure 3. 17: (a): Osteryoung square wave voltammogram and (b) cyclic voltammogram of complex **21** in distilled DMF containing 0.1 M TBABF₄. Scan rate = 100 mVs⁻¹.

Spectroelectrochemistry

Spectroelectrochemical studies of **21** were carried out in order to confirm the assignments of the redox couples. Reduction at potentials of couple **III**, resulted in the decrease in intensity of the Q-band at 830 nm and an increase in intensity of the peak at 757 nm (Figure 3.18(a)). These spectral changes are typical [23] of metal-based reduction processes (and of $\text{Ti}^{\text{IV}}\text{Pc}^{-2}/\text{Ti}^{\text{III}}\text{Pc}^{-2}$ process [117,124]), and are assigned to reduction of $\text{Ti}^{\text{IV}}\text{TAPc}$ species to $\text{Ti}^{\text{III}}\text{TAPc}$. On close examination of the MPc solution in the OTTLE cell, it was found that the solution turned green from an initial brown colour. Applied potential was increased to potential of process **II**, the peak at 757 nm shifted to 750 nm accompanied by continued decrease of the peak at 830 nm, with diffuse isosbestic points at 670 and 485 nm (Figure 3.18(b)). These spectral changes are associated [23] with metal-based reduction and the formation of a $\text{Ti}^{\text{II}}\text{Pc}^{-2}$ species. Further reduction at potentials of process **I**, was expected to occur at the ring ($\text{Ti}^{\text{II}}\text{Pc}^{-2}/\text{Ti}^{\text{II}}\text{Pc}^{-3}$) in comparison with other TiPc complexes [49, 117]. However, no further changes were observed on application of potentials of process **I**.

Oxidation at potentials of process **IV** (~ 1.0 V) resulted in the decrease in intensity of the Q-band at 830 nm and of the charge transfer band at 520 nm, and the formation of a broad and weak feature near 600 nm, Figure 3.18(c). The changes occurred with isosbestic points at 917 and 583 nm (Figure 3.18(c)). These spectra changes indicate phthalocyanine ring oxidation [38] hence confirmation that process **IV** corresponds to $\text{Ti}^{\text{IV}}\text{Pc}^{-1}/\text{Ti}^{\text{IV}}\text{Pc}^{-2}$. No further changes were observed, on increasing the potential to values beyond process **V**. Since oxidation can only occur at the ring in $\text{Ti}^{\text{IV}}\text{Pc}$ complexes, it is expected that further oxidation to the Pc^0 species would occur.

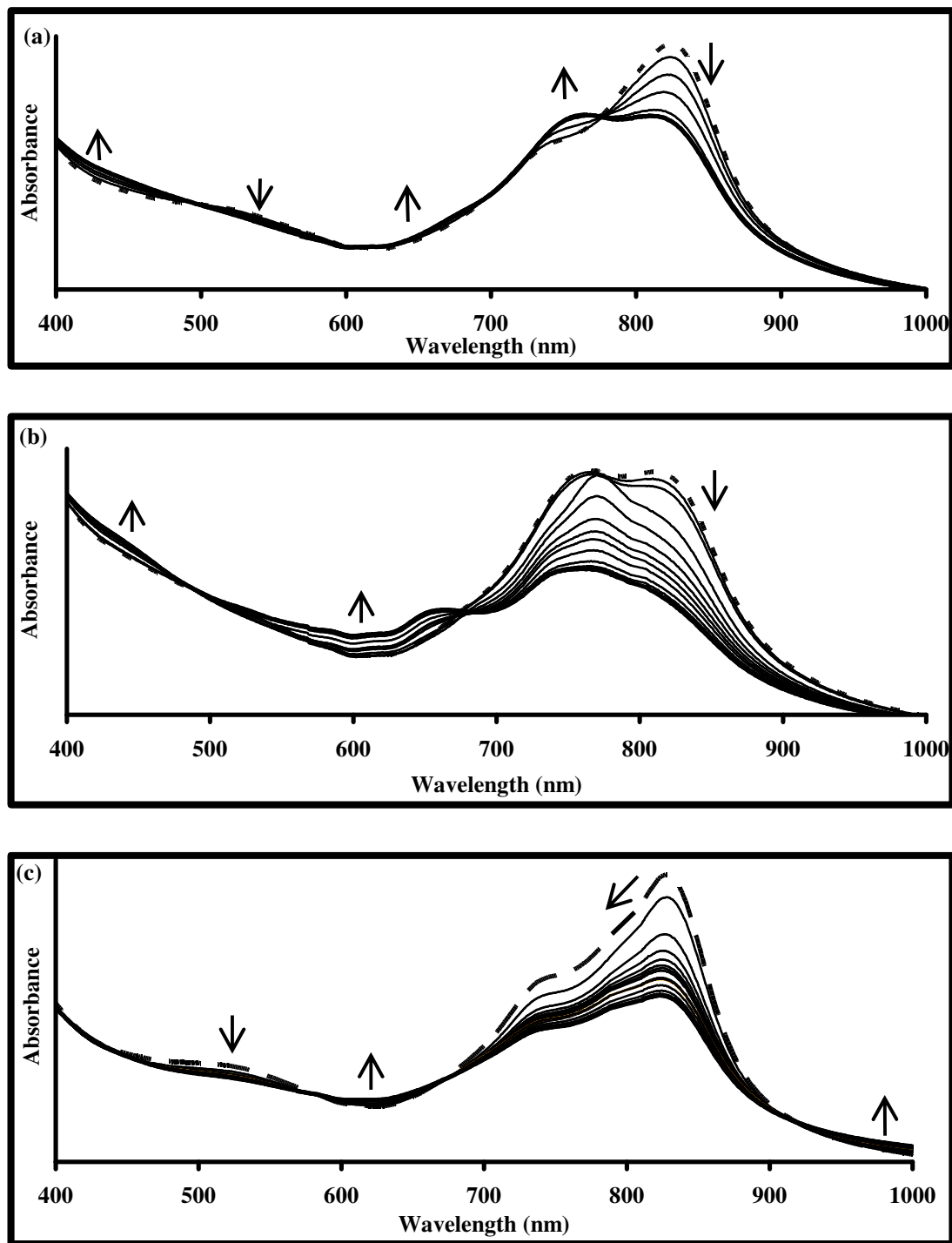
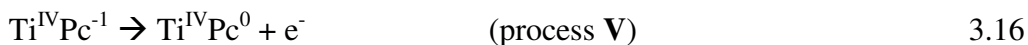
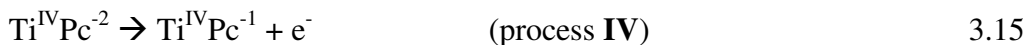
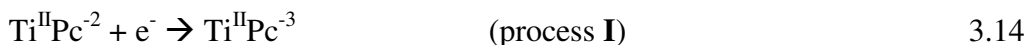
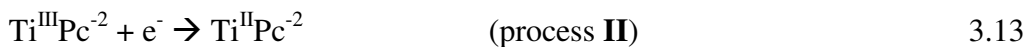
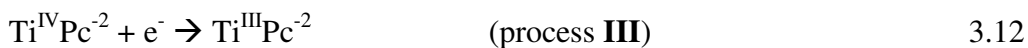


Figure 3. 18: UV/Vis/NIR spectral changes of OTiTAPc in DMF containing 0.1 M TBABF₄ observed during application of controlled potential at potentials of the following processes; (a) **III** (-0.6 V) (b) **II** (-1.2 V) and (c) **IV** (0.8 V). The first scan in (b) is the same as the last scan in (a).

The redox processes that complex **21** underwent during voltammetry are outlined below based on the spectroelectrochemical studies, eqs. 3.12-3.16:



Conclusion

Non-peripherally substituted Mn and Co phthalocyanines with phenylthio groups (**12-14**) were newly synthesized and characterized using various methods. Amino (**19-21**) derivatized Ti, Mn and Co phthalocyanines were also newly synthesized and characterized. The non-peripheral substitution of electron donating groups such as sulphur and amino resulted in phthalocyanines that absorb in the near-IR region.

Chapter 4

Electrode

modification and

characterization

4. Electrode modification and characterization

4.1 Self assembled monolayers

4.1.1 Fabrication of gold ultramicrocylinder and fiber electrodes

The gold ultramicro cylinder electrode (UMCE) was constructed by using a 3 cm long and 0.5 cm wide Teflon block (Figure 4.1). A 1 mm gap was made along the width at the bottom end of the block. A small hole was made 0.5 cm from the top of the plate to allow for the insertion of a copper wire which served as a connection to the electrochemistry system. The ultramicro wire or the gold coated fiber was then coiled around the copper wire (for contact) and the sides of the block, and then positioned over the gap at the bottom of the block, exposing 1 mm fiber or wire (the working part of the electrode). The electrodes were used for SAM formation. After the SAM had been formed the UMCE or gold coated fiber was rinsed in DMF followed by Millipore water. Once dry, epoxy glue was used to cover the UMCE or gold coated fiber only exposing the 1mm surface on which the SAM was formed.

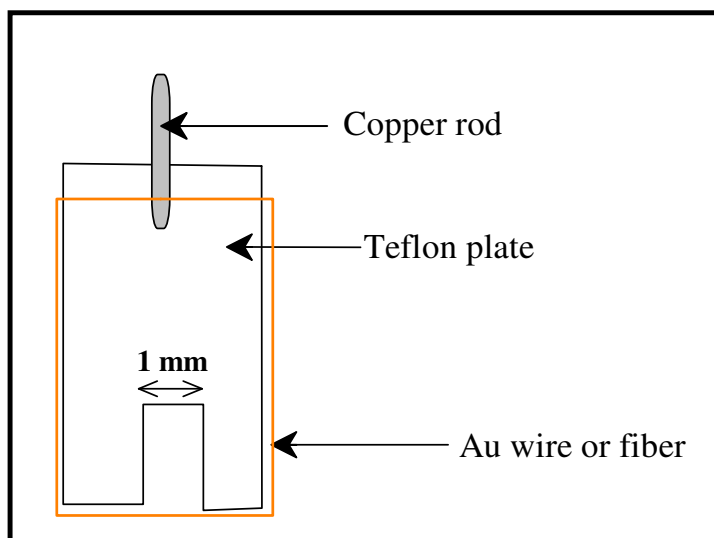


Figure 4. 1: The ultramicroelectrode configuration

4.1.2 SAM formation on gold electrodes

Gold electrodes (disk, UMCE and fiber) were modified with phenylthio derivatized phthalocyanines through the formation of self assembled monolayers. This method was achieved by immersing gold electrodes in argon-purged solutions of MPC complexes (complexes **12** - **15**). Electrochemical methods were used to characterize the monolayers formed on the gold surfaces.

Cyclic voltammetry was used to characterize the SAM modified gold electrodes using the well established Faradaic processes [65, 125-127]. These processes are based on the idea that a gold surface well covered with a self-assembled monolayer should have the ability to block Faradic process that would easily occur at the bare gold surface. Such processes include the blockage of gold oxidation/reduction which occurs when oxygen is present in solution, the blockage of the $[\text{Fe}(\text{H}_2\text{O})_6]^{3+}/[\text{Fe}(\text{H}_2\text{O})_6]^{2+}$ couple and the under potential deposition of copper. In this work the gold electrode (disk, UME and fiber) behavior was

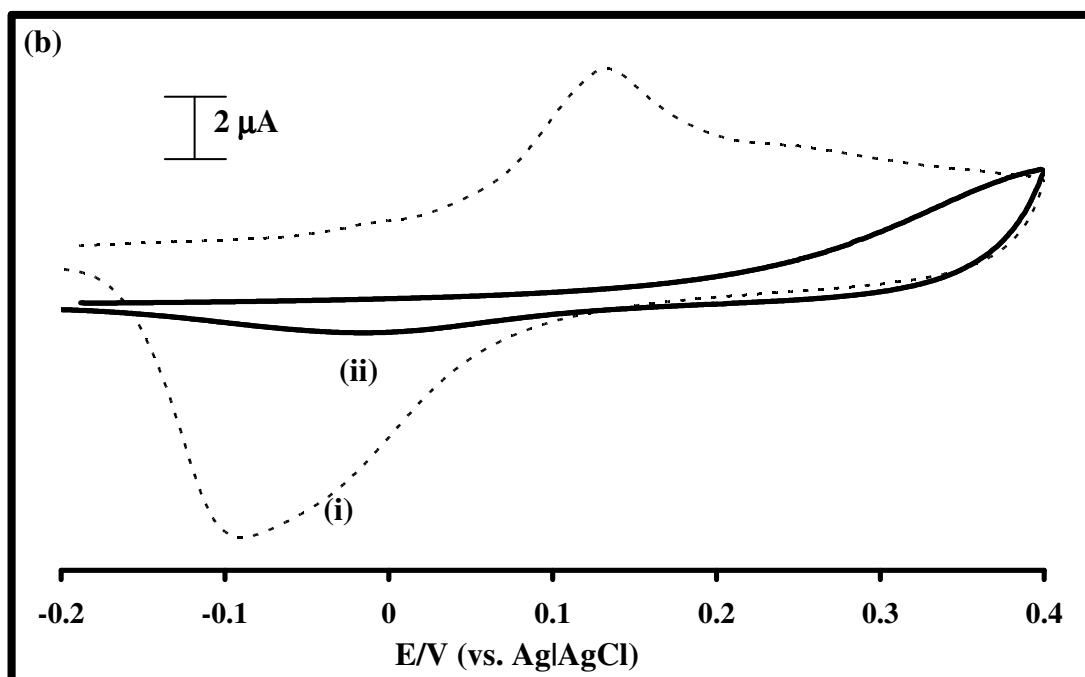
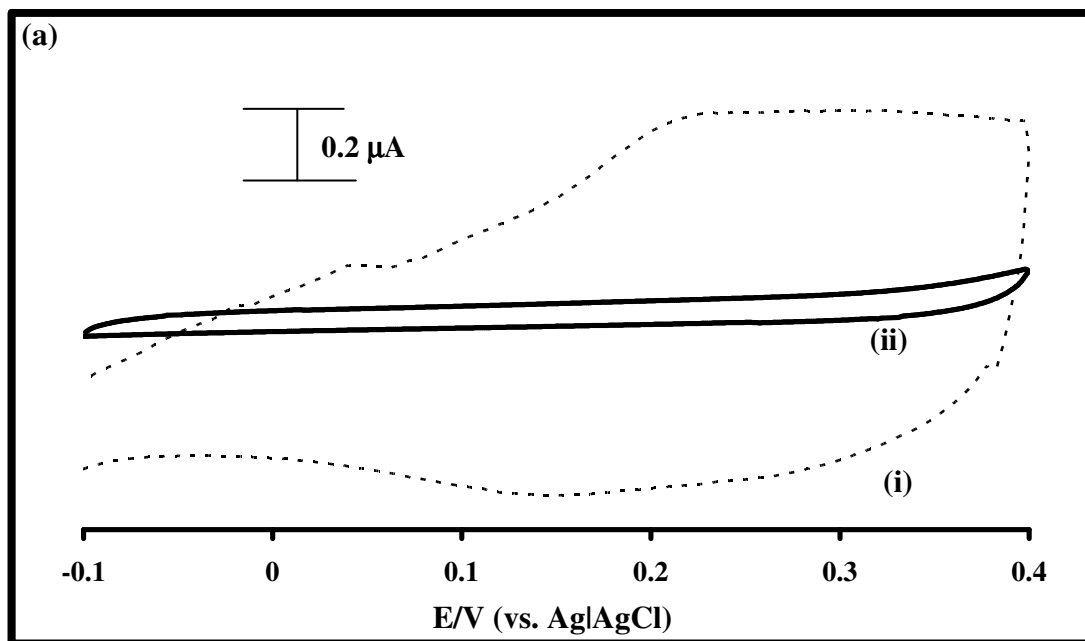
studied in acid media (Na_2SO_4 , pH 4) (Figure 4.2 (a), Figure 4.3(a) and Figure 4.4(a)), basic media (0.01M KOH) (Figure 4.2(b), Figure 4.3(b) and Figure 4.4(b)), in 1mM $\text{Fe}(\text{NH}_4)(\text{SO}_4)_2$ in 2 M HClO_4 (Figure 4.2(c) and Figure 4.3(c)) and in 1mM $\text{K}_3\text{Fe}(\text{CN})_6$ in 2 M KCl (Figure 4.2(d) and Figure 4.3(d)). For simplicity, only SAM of complex **12** is shown on Figures 4.2 to 4.4.

4.1.2.1 SAM characterization of the gold disk electrode

Figure 4.2(a) shows the CV of the bare gold disk electrode and the MPc-SAM modified gold disk electrodes in 1mM Na_2SO_4 (pH 4). The SAM modified electrode show reduction in charging currents; this is linked to the presence of a layer with a low dielectric constant between the electrode and electrolyte [127] confirming modification of the electrode. Figure 4.2(b) shows that complex **12** SAM exhibits blockage of the gold oxidation/reduction process in 0.01M KOH. The broad peak at 0.35V is most probably due to the $\text{Co}^{\text{III}}\text{Pc}^{-2}/\text{Co}^{\text{II}}\text{Pc}^{-2}$ process, in comparison with literature for adsorbed thio substituted CoPc complexes [128,129]. Figure 4.2(c) shows the inhibition of the $[\text{Fe}(\text{H}_2\text{O})_6]^{3+}/[\text{Fe}(\text{H}_2\text{O})_6]^{2+}$ redox process in the presence of SAMs. The peak near 0.7 V is due to MPc based redox process, the shifting of the peak is due to differences in media compared to Figure 4.2(b). The $[\text{Fe}(\text{H}_2\text{O})_6]^{3+}/[\text{Fe}(\text{H}_2\text{O})_6]^{2+}$ redox process is a known reversible process of $\text{Fe}(\text{NH}_4)(\text{SO}_4)$ solution at bare gold electrodes, SAM modification of gold electrodes results in this process being inhibited.

The fast electron transfer of the $[\text{Fe}(\text{CN})_6]^{3-}/[\text{Fe}(\text{CN})_6]^{4-}$ redox couple is not inhibited by the SAMs as shown in Figure 4.2(d) as compared to the $[\text{Fe}(\text{H}_2\text{O})_6]^{3+}/[\text{Fe}(\text{H}_2\text{O})_6]^{2+}$ redox process, but the cathodic to anodic peak potential separation (ΔE) for this couple

increases for SAM modified electrodes. The lack of inhibition of $[\text{Fe}(\text{CN})_6^{3-}] / [\text{Fe}(\text{CN})_6^{4-}]$ redox couple has been observed before using adsorbed cobalt tetra-aminophthalocyanine films on vitreous carbon electrodes. It was reported that both modified and unmodified electrodes showed the same redox potential and almost equal peak current intensities for the $[\text{Fe}(\text{CN})_6^{3-}] / [\text{Fe}(\text{CN})_6^{4-}]$ redox reaction, and that the modified electrodes act as electronic conductors which allow rapid electron transfer to the solution species [130]. The lack of inhibition for this couple was also observed for complex **13**, **14** and **15** SAMs.



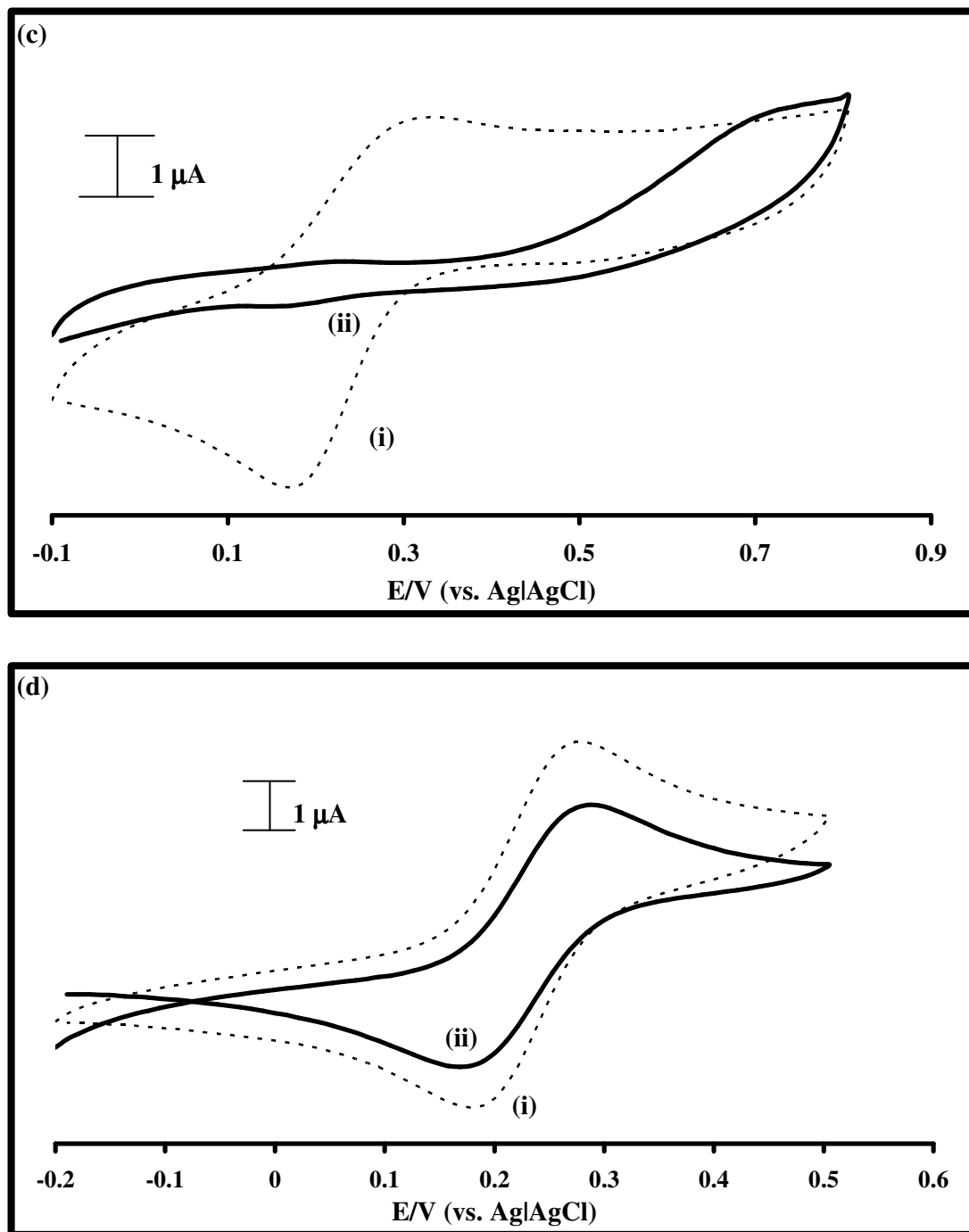
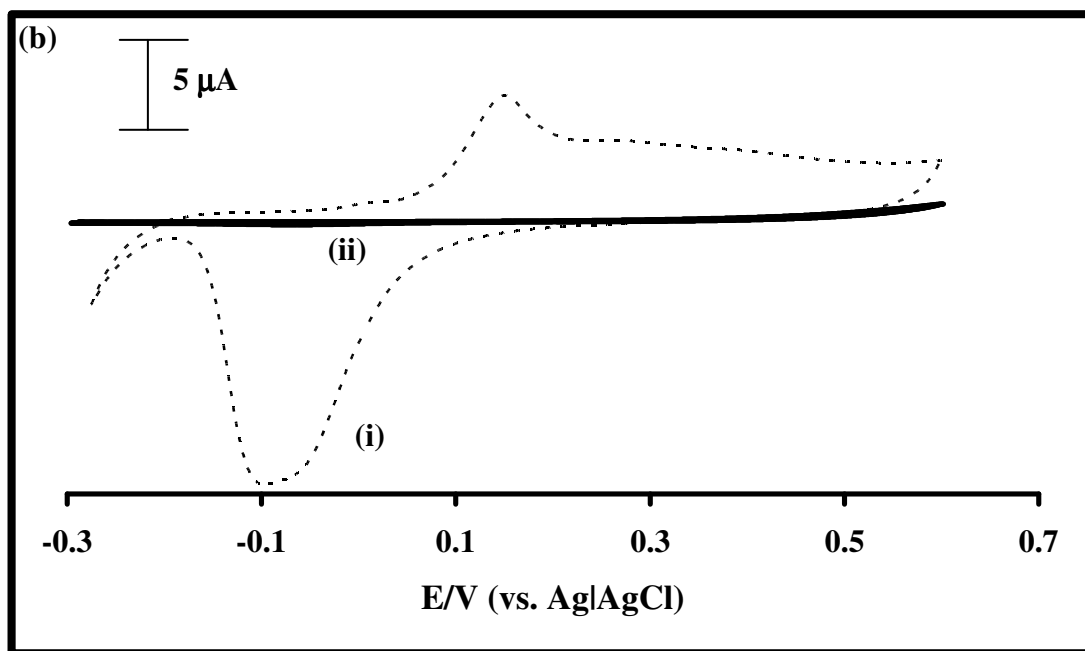
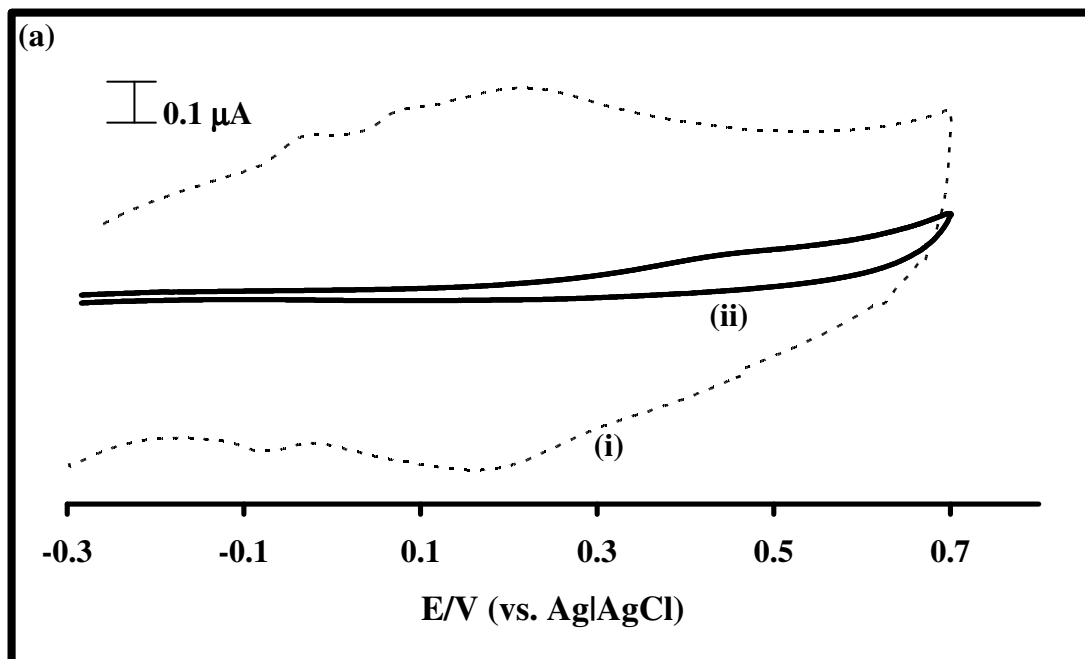


Figure 4. 2: Cyclic voltammograms of (i, dotted) unmodified gold disk electrode and (ii, solid) SAM of complex **12** (a) 1 mM Na_2SO_4 in pH 4 buffer solution, (b) 0.01M KOH solution, (c) 1 mM $\text{Fe}(\text{NH}_4)(\text{SO}_4)_2$ in 2mM HClO_4 solution, (d) 1 mM $\text{K}_3\text{Fe}(\text{CN})_6$ in 2 mM KCl solution. Scan rate = 50 mVs^{-1} .

4.1.2.2 SAM characterization of gold ultramicro cylinder electrodes (UMCE)

The cyclic voltammetry of the bare Au UMCE in 1mM Na₂SO₄ (pH 4) solution is shown in Figure 4.3(a). The Au redox process is observed at ~ 0.2V. The figure also shows another reversible couple at ~ - 0.08V, this is due to the formation of Au ad-atoms on the surface of the Au UMCE [131]. The MPc-SAM modified Au UMCE's showed no Au redox processes and a huge reduction in charging currents was observed confirming SAM formation. The Co^{III}Pc⁻²/Co^{II}Pc⁻² oxidation process is observed as a very weak peak around 0.4V. Figure 4.3(b) shows the blockage of Au oxidation/reduction on the UMCE in 0.01M KOH solution. A pronounced redox process was observed on the bare electrode, with a weaker anodic process. The SAM modified electrode show greatly reduced currents. The SAMs were investigated for the suppression of the Fe(H₂O)₆³⁺/[Fe(H₂O)₆]²⁺ Faradic process, Figure 4.3(c). The MPc-SAM modified electrode show complete inhibition of the oxidation process. The SAM modified UMCEs were studied in 1 Mm K₃Fe(CN)₆ in 2 M KCl, Figure 4.3(d), sigmoidal shaped potential curves which are typical of UMCEs are observed. The rate of diffusion of the [Fe(CN)₆³⁻] species to the electrode surface is very fast resulting in a diffusion thickness that exceeds the size of the electrode, hence steady-state currents are reached quickly and the voltammetric response is sigmoidal. The lack of blockage of the [Fe(CN)₆³⁻]/[Fe(CN)₆⁴⁻] redox couple may be explained as discussed above for the Au disc electrode.



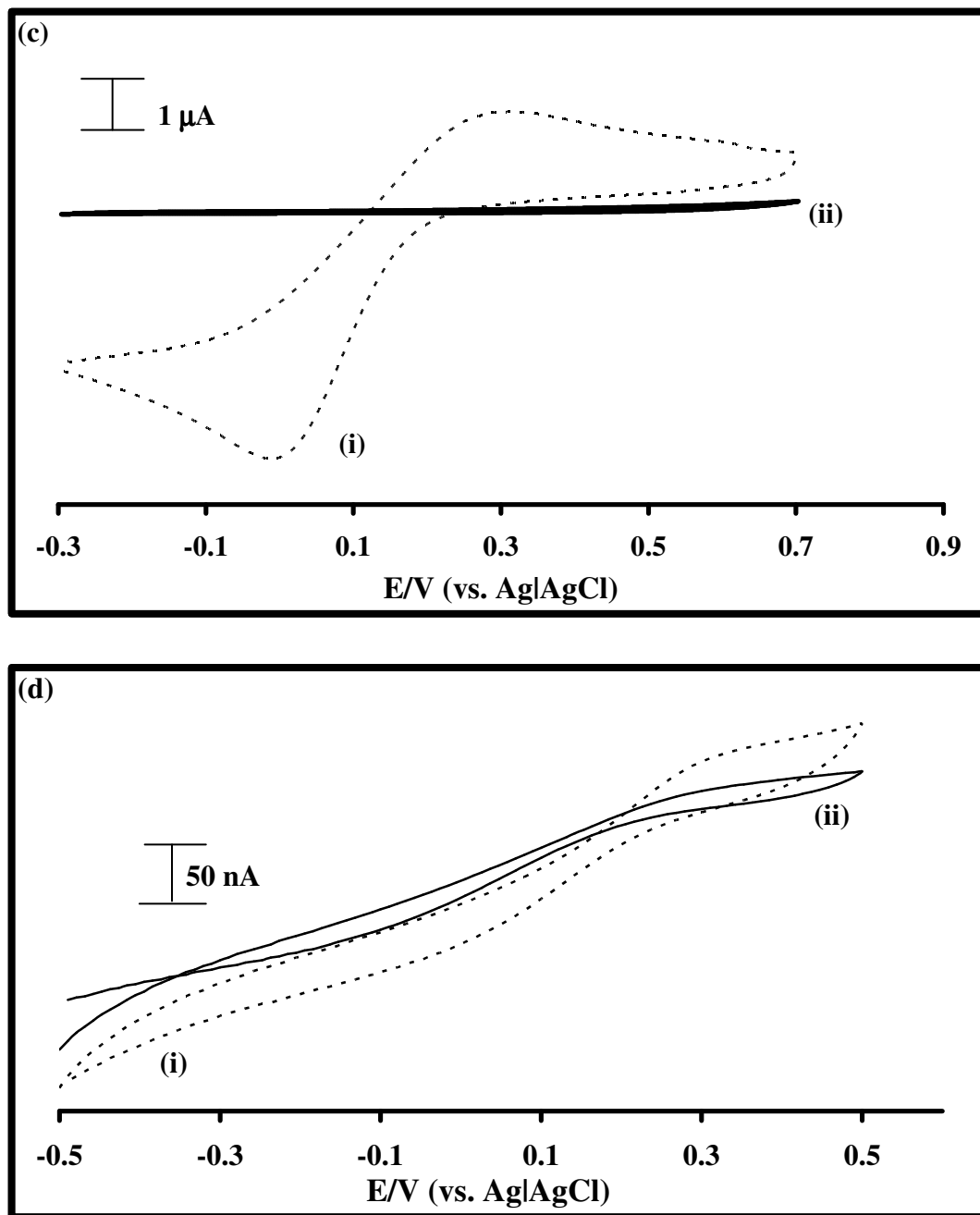


Figure 4. 3: Cyclic voltammograms of (i, dotted) unmodified gold UMCE and (ii, solid) SAM of complex **12** (a) 1 mM Na_2SO_4 in pH 4 buffer solution, (b) 0.01M KOH solution, (c) 1mM $\text{Fe}(\text{NH}_4)(\text{SO}_4)_2$ in 2 M HClO_4 solution, (d) 1 mM $\text{K}_3\text{Fe}(\text{CN})_6$ in 2 M KCl solution. Scan rate = 50 mVs^{-1} .

4.1.2.3 SAM characterization of gold coated fiber electrodes

Figure 4.4(a) shows the bare and modified Au fiber in pH 4 buffer solution containing 1mM Na₂SO₄, the modified gold fiber shows relatively good inhibition of the gold redox process. The current produced at the bare electrode is larger (in the mA range) than currents produced at the Au disk (Figure 4.2) and Au UMCE (Figure 4.3) bare electrodes (both in μA range), this is because the fiber is made of numerous micro strands. Blockage of the Au redox processes was observed in 0.01M KOH as shown in Figure 4.4(b). Attempts to study the fibers in Fe(NH₄)(SO₄)₂ and K₃Fe(CN)₆ solutions were made but were unsuccessful as the Fe³⁺/Fe²⁺ couple was not observed for both solutions.

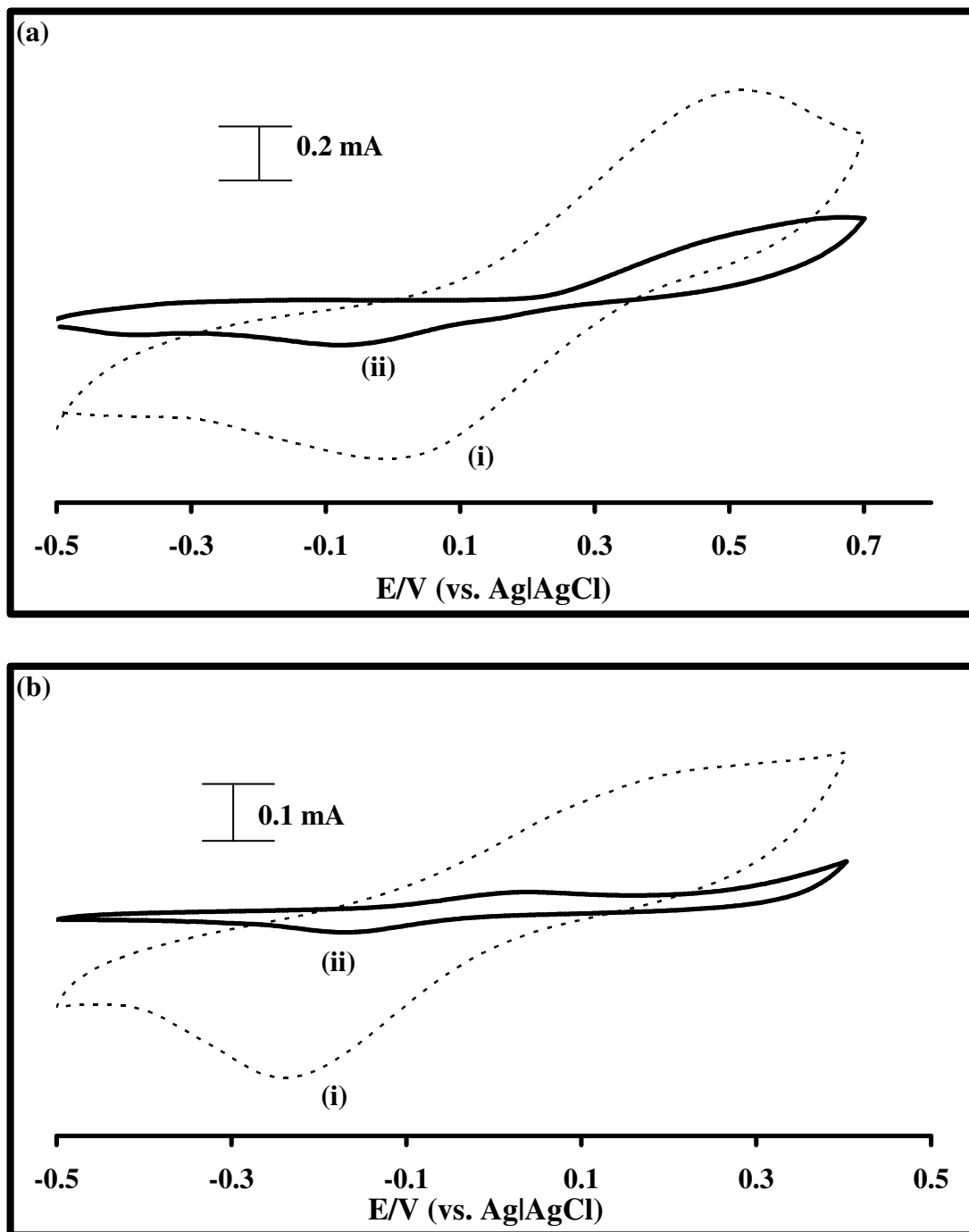


Figure 4. 4: Cyclic voltammograms of (i, dotted) unmodified gold coated fiber and (ii, solid) SAM of complex **12** (a) 1 mM Na_2SO_4 in pH 4 buffer solution, (b) 0.01M KOH solution.

Images of the unmodified and complex **12** SAM modified Au coated fiber were taken using a 40X Ramanscope. Figure 4.5(a) shows the unmodified gold fiber and Figure 4.5(b) shows the modified fiber, this fiber is less fluorescent compared to the unmodified, showing that it has been modified.

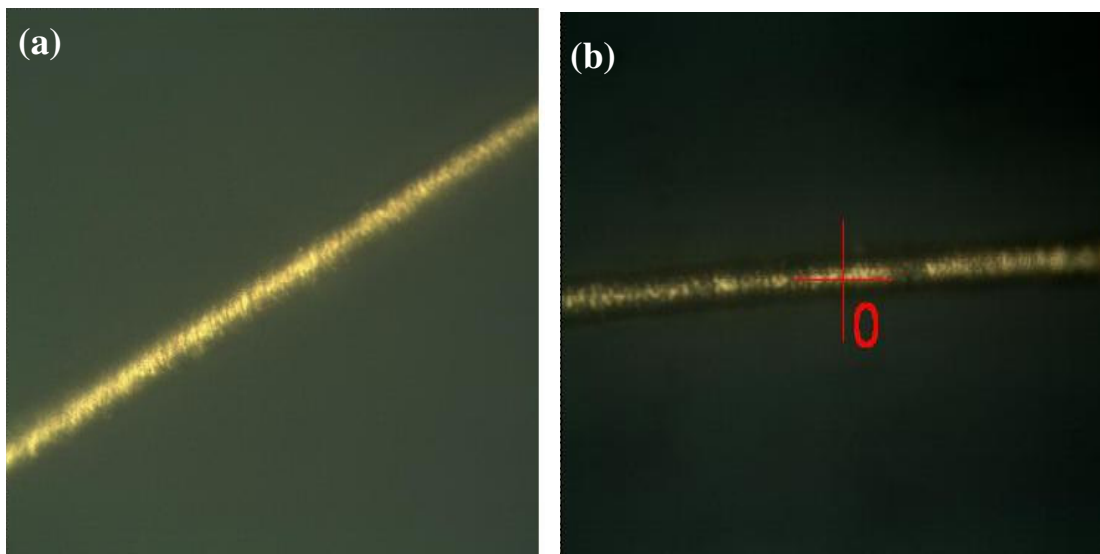


Figure 4. 5: Ramanscope images of (a) bare fiber and (b) complex **12** SAM-fiber.

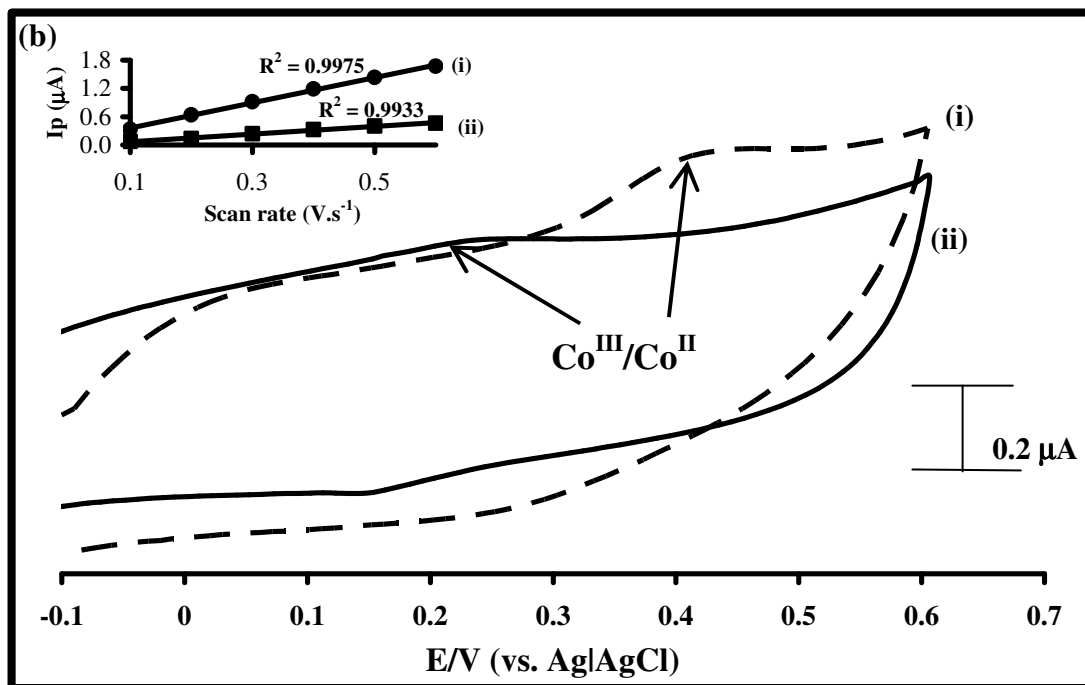
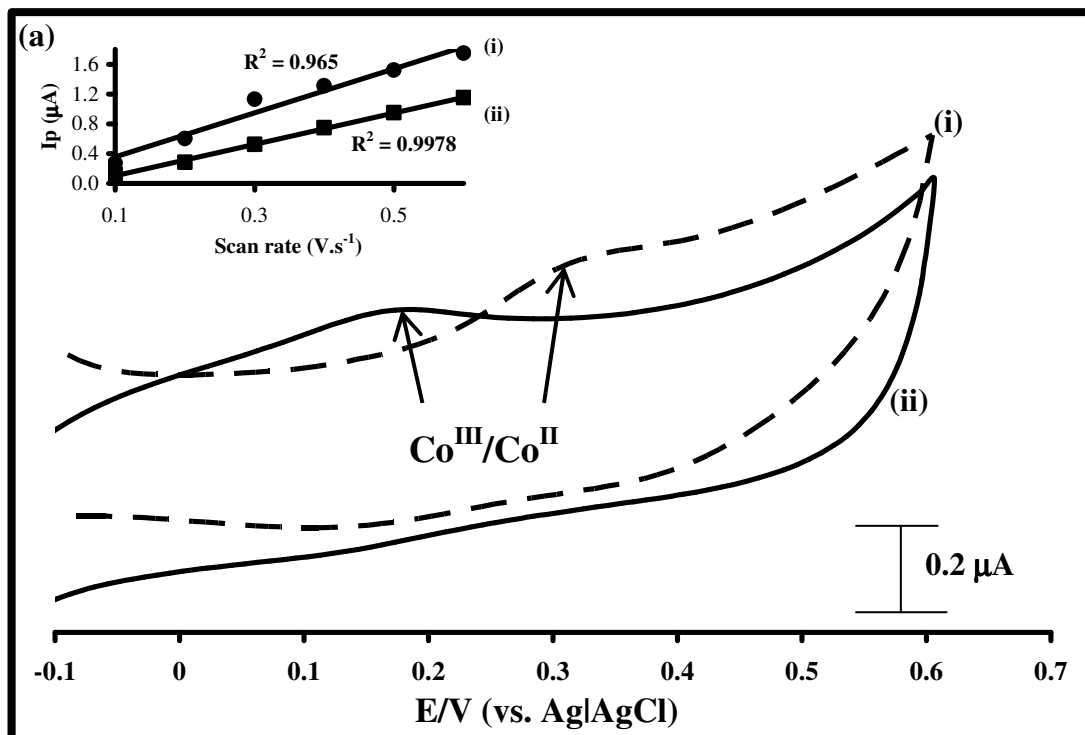
4.1.3 Redox couples of MPcs on SAM electrodes

The redox properties of the surface confined MPcs were probed in pH 4 and pH 7.4 phosphate buffers. This was done because the electrodes were fabricated for L-cysteine oxidation in pH 4 buffer and for nitrite oxidation in pH 7.4 buffer.

Figures 4.6(a)-(b) show the CVs of MPc-SAMs of complexes **12** and **13** respectively in pH 4 and pH 7.4 buffer on gold disk. The $\text{Co}^{\text{III}}/\text{Co}^{\text{II}}$ process was observed for complex **12** at 0.3 V and at 0.4 V for **13** in pH 4 buffer, this process is known to be difficult and if found irreversible for adsorbed CoPc complexes [60], but it is reasonably well resolved in Figure 4.6. The peak appears at less positive potentials in pH 7.4 buffer.

Metal redox processes were observed for complex **14**, Figure 4.6(c) at -0.24 V in pH 4 due to $\text{Mn}^{\text{III}}/\text{Mn}^{\text{II}}$ redox process. The currents for the MPc redox peaks increased linearly with scan rate (Figures 4.6(a)-(c) inserts) showing that the MPcs are surface confined onto the gold electrodes. No clear peaks were observed for complex **15** in both pH 4 and pH 7.4 buffer solutions.

Figure 4.7 shows the $\text{Co}^{\text{III}}\text{Pc}^{-2}/\text{Co}^{\text{II}}\text{Pc}^{-2}$ oxidation processes observed for complex **12** and **13** SAMs on UMCE as very weak peaks around 0.4V and 0.3V respectively in 1mM Na_2SO_4 contained in pH 4 solution. No peaks were observed on the gold coated fibers.



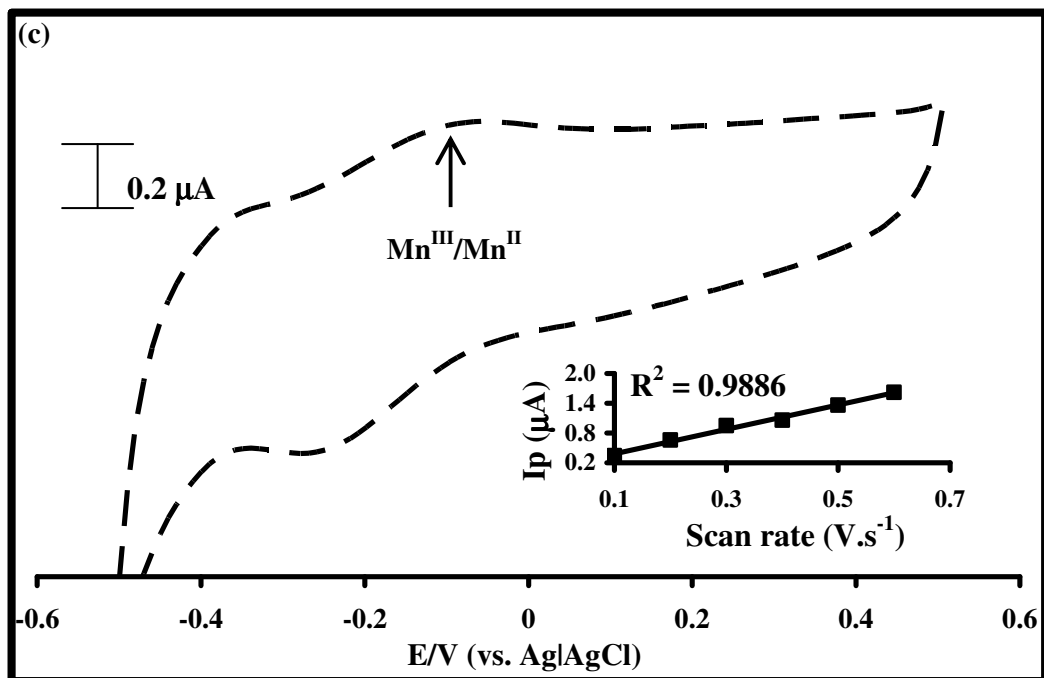


Figure 4. 6: Cyclic voltammograms of complex **12** (a), **13** (b) and **14** (c) in pH 4 buffer solution (dashed line) and pH 7.4 buffer solution (solid line) showing MPC related redox peaks on Au disk electrode. Scan rate = 100 mVs⁻¹. Insert is variation of redox peak current with scan rate.

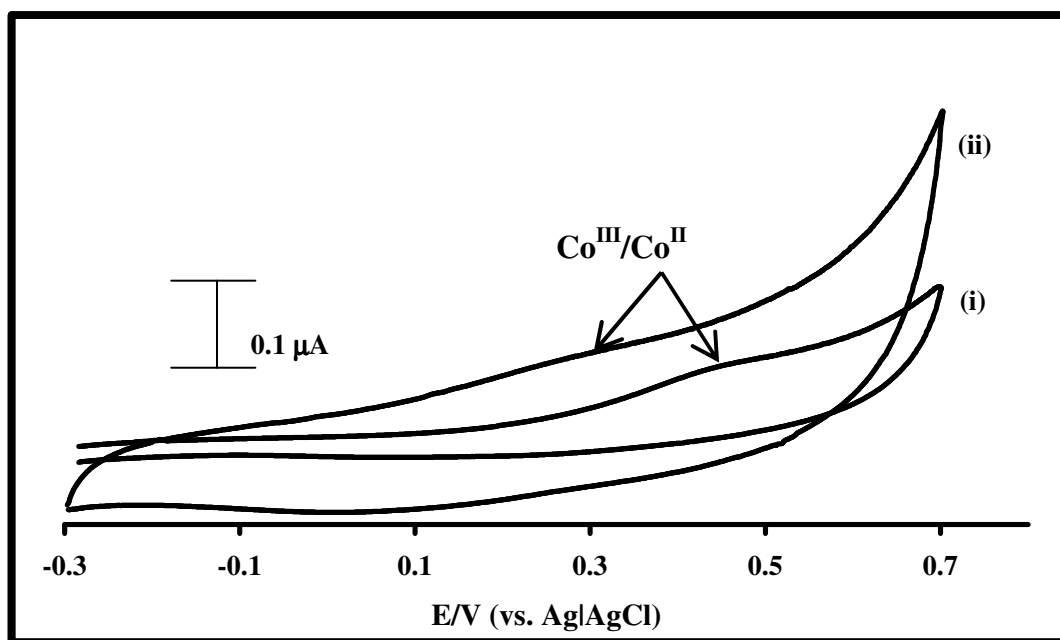


Figure 4. 7: Cyclic voltammograms of complex **12** (i), **13** (ii) SAMs on UMCE in pH 4 buffer solution. Scan rate = 100 mVs⁻¹.

Surface coverage (Γ_{MPc} , mol/cm²) of complexes on the gold disk electrodes were estimated using equation 4.1:

$$\Gamma_{\text{MPc}} = \frac{Q}{nFA} \quad 4.1$$

where Q is the background corrected electric charge under anodic peaks (due to metal redox peaks of MPcs) of the SAM modified gold disk electrodes, in buffer solution (Figure 4.6), n is the number of electrons transferred (assumed to be 1), F is the Faraday constant (96485 C/mol) and A is the surface area of the electrode (0.02011 cm²). The surface coverage for the complexes in pH 4 buffer solution is shown on Table 4.1. These values are close to the expected value (1×10^{-10} mol cm⁻²) for a phthalocyanine monolayer lying flat on a surface [79], confirming a monolayer formation of the phthalocyanine on the electrode surface. The Γ_{MPc} were not calculated on fiber and UMCE due to lack of accurate A values.

The ion blocking factor, often called ion barrier factor (Γ_{ibf}) was calculated using equation 4.2 to give an indication of the solvent or ion permeability of the SAMs, the ideal value of $\Gamma_{\text{ibf}} = 1$, indicates the SAMs ability to block ions or solvent from penetrating the surface of the electrode [81].

$$\Gamma_{\text{ibf}} = 1 - \left(\frac{Q_{\text{SAM}}}{Q_{\text{Bare}}} \right) \quad 4.2$$

where Q_{SAM} and Q_{Bare} is charge under the cathodic peaks in 0.01M KOH solution (Figures 4.3(b), 4.3(b), 4.4(b)) for SAM modified electrodes and bare solid disk electrodes respectively. The Γ_{ibf} values are shown in Table 4.1. The best SAMs formed are on the UMCE as they showed the highest ion barrier factor, considering the same complex for example **13**.

Table 4. 1: Surface coverage and ion barrier factor values for the various MPCs-SAMs in pH 4 buffer solution.

Complex	Γ , (10^{-10} mol.cm ⁻²)	Γ_{ibf}
Disk-SAM (12)	1.35	0.96
Disk-SAM (13)	1.04	0.82
Disk-SAM (14)	1.22	0.96
Disk-SAM (15)	-	0.93
UMCE-SAM (12)	-	0.97
UMCE-SAM (13)	-	0.95
Fiber-SAM (12)	-	0.88
Fiber-SAM (13)	-	0.88

4.2 Electropolymerization

The adsorption of complexes **19**, **20** and **21** on glassy carbon electrode (GCE) was successfully achieved via electropolymerisation of these complexes in DMF by repetitive scanning at a constant scan rate of 100 mV.s⁻¹.

Figure 4.8(a) shows voltammograms during the polymerization of complex **19** cycled in the potential range of -0.4 to 1.0 V vs. Ag|AgCl. The intensity of currents for process **III** increased with increasing scan number and there was a decrease in current intensity at the -NH₂ oxidation potential indicating a depletion of the amino monomer. A new broad peak at ~ -0.1V was formed. The formation of new peaks is characteristic of electropolymerization. After polymerization a glossy brown film was observed on the

surface of the electrode. Following polymerization the electrode (represented as *poly-19*) was cycled in pH 7.4 buffer solution as shown on Figure 4.8(b). The $\text{Co}^{\text{II}}/\text{Co}^{\text{III}}$ (process **III**) was the only process observed for the polymer. This process was more pronounced compared to Figure 4.6(a) and (b) with $E_{1/2}$ value of 0.22V. The insert in Figure 4.8(b) shows the linear relation between process **III** and the scan rate, confirming a surface confined *poly-19*.

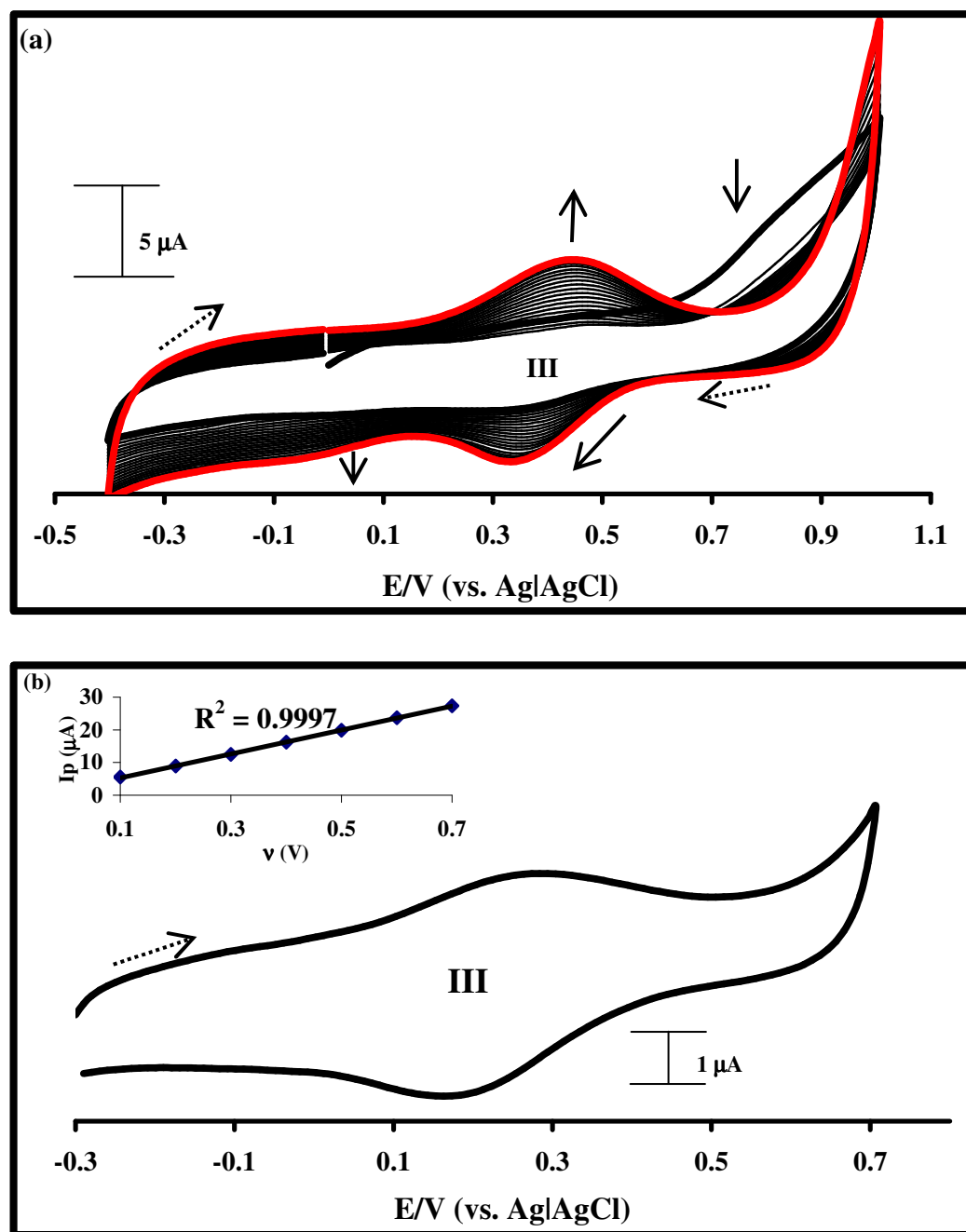


Figure 4. 8: (a) Evolution of cyclic voltammograms on GCE in DMF containing 0.1 M TBABF₄ during repeated successive scans showing the formation of *poly-19* and (b) cyclic voltammograms of *poly-19* film on GCE in phosphate buffer solution (pH 7.4). Inset is plot of i_p vs. v . Scan rate = 100 mVs^{-1} .

Figure 4.9(a) shows a series of CVs (30 scans) during electropolymerisation of complex **20**, cycled in the potential range of -0.6 to 1.0 V vs. Ag|AgCl. During electropolymerisation, the couple associated with the $\text{Mn}^{\text{III}}/\text{Mn}^{\text{II}}$ process at $E_{1/2} = -0.31$ increased in current intensity with the cathodic and anodic peaks slightly shifting towards more negative and less negative potentials respectively. Gradual formation of new peaks at 0.20 V and 0.43 V was observed. The shifts and formation of new peaks confirm the formation of an electroactive polymer on the electrode surface. Recording the cyclic voltammogram in pH 7.4 buffer solution of the modified electrode, now called *poly-20*, resulted in the feature shown in Figure 4.9(b), which shows the $\text{Mn}^{\text{III}}/\text{Mn}^{\text{II}}$ (labelled process **II** at -0.42 V) and $\text{Mn}^{\text{III}}\text{Pc}^{-2}/\text{Mn}^{\text{III}}\text{Pc}^{-1}$ (labelled process **III** at 0.27 V), shifted to more negative potentials in aqueous media compared to Figure 3.15 in DMF.

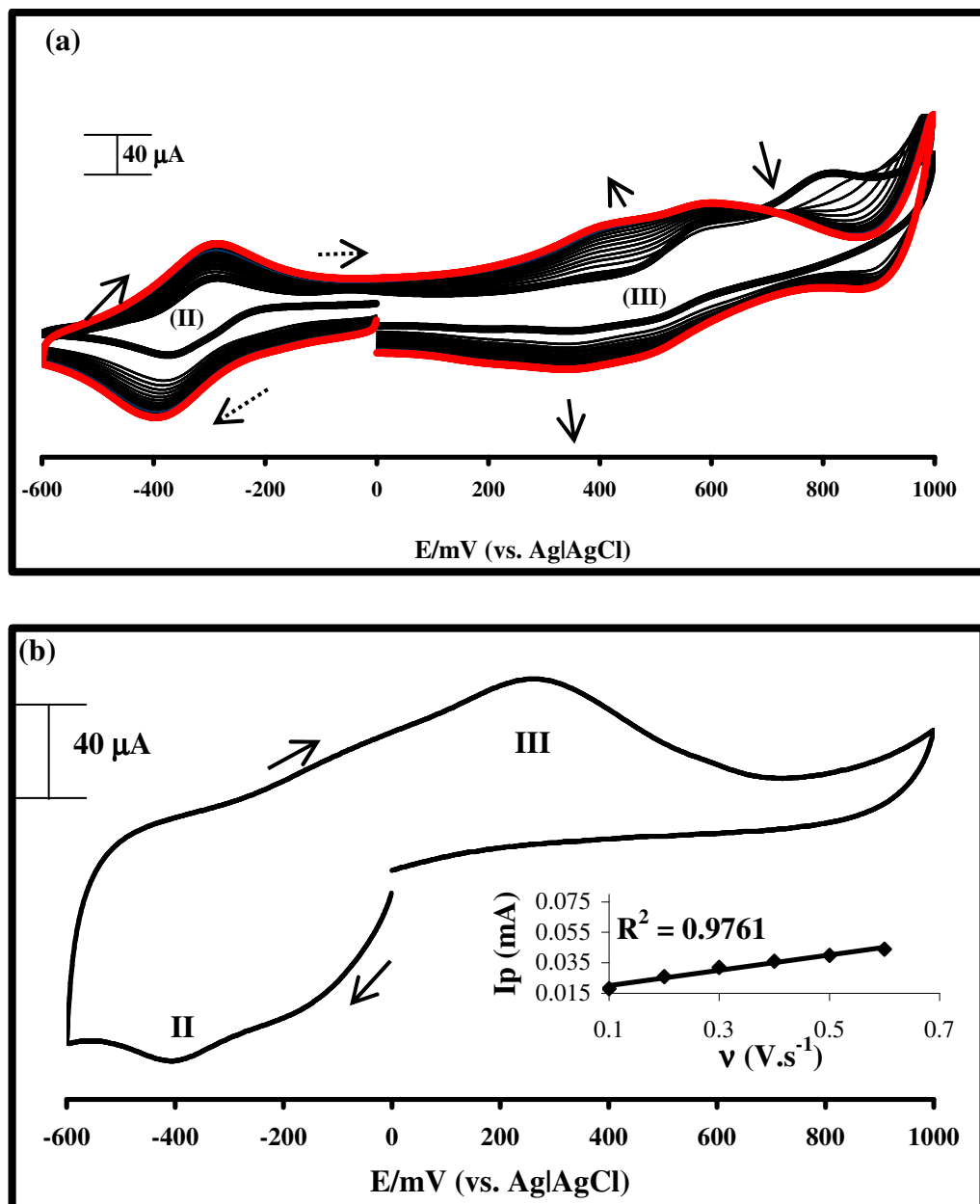


Figure 4. 9: (a) Evolution of cyclic voltammograms on GCE in DMF containing 0.1 M TBABF₄ during repeated successive scans showing the formation of *poly-20*, (b) cyclic voltammograms of *poly-20* film on GCE in phosphate buffer solution (pH 7.4). Inset is plot of i_p vs. v . Scan rate = 100 mVs⁻¹.

Electropolymerisation of complex **21** was achieved through repetitive cycling at the applied potential between -1.5 V and 1.5 V vs. Ag|AgCl; 30 consecutive scans thereof are shown in Figure 4.10(a). Upon polymerization, all redox processes increased in intensity as the amount of complex deposited on the electrode increased. A new peak due to the polymer was formed at -0.6 V. A green film was observed on the surface of the electrode after electropolymerization, further confirming deposition of complex **21**. A CV of the polymer was recorded in a phosphate buffer (pH 7.4) solution, where the polymer peak was observed at -0.49 V and oxidation features at 0.18 V and 0.45 V (Figure 4.10(b)).

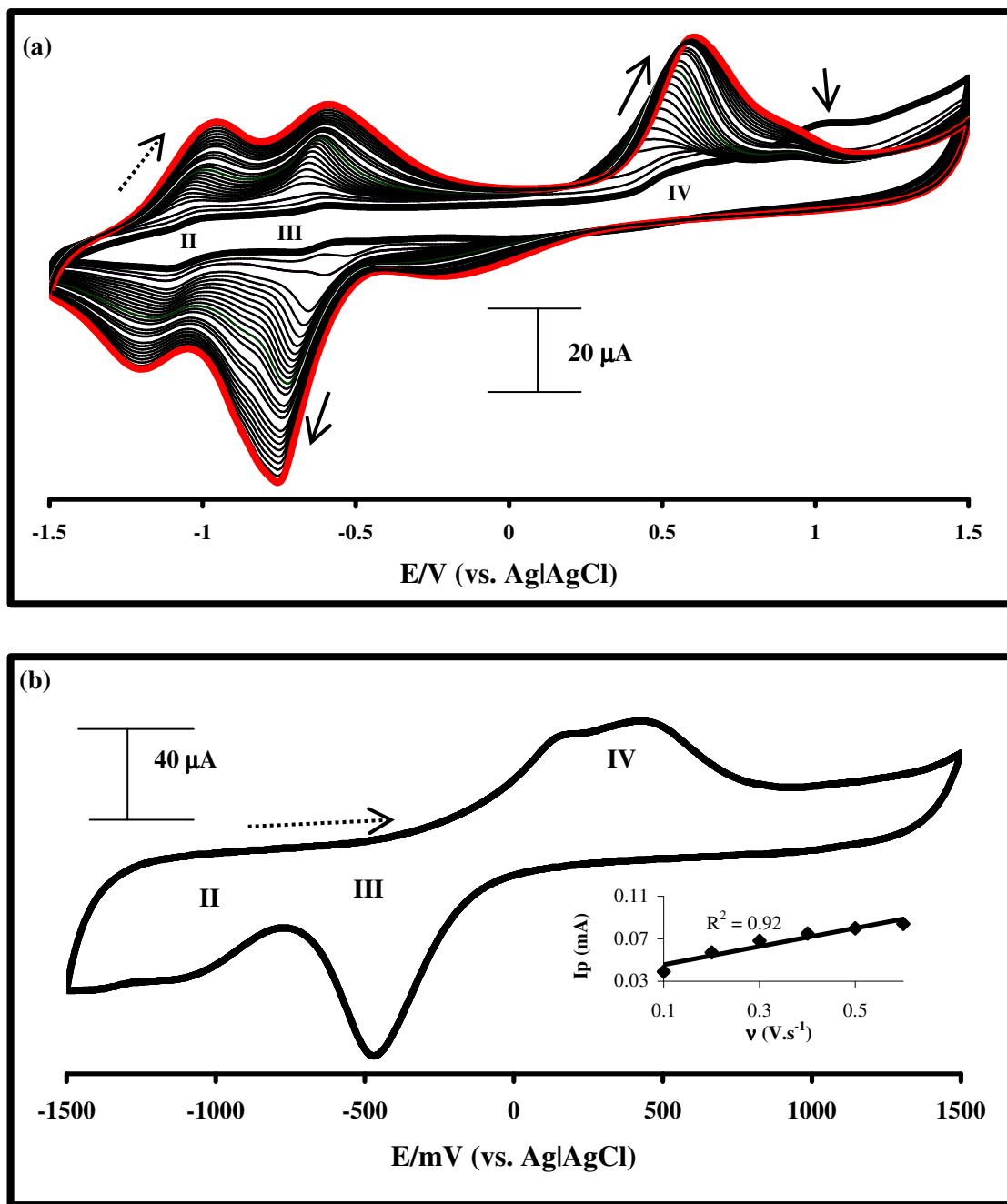


Figure 4. 10: Evolution of cyclic voltammograms on GCE in DMF containing 0.1 M TBABF₄ during repeated successive scans showing the formation of (a) *poly-21* and of (b) *poly-21* film on GCE in phosphate buffer solution (pH 7.4). Scan rate = 100 mVs⁻¹. Inset is plot of i_p vs. v .

The surface coverage, Γ_{MPc} of all modified electrodes (**19-21**) was determined using equation 4.3;

$$I_p = \frac{n^2 F^2 A v \Gamma_{\text{MPc}}}{4RT} \quad 4.3$$

where I_p is peak current, v is the scan rate, R is the gas constant, T is the temperature and the rest of the constants have their usual meaning. Surface coverage was calculated to be $8.2 \times 10^{-10} \text{ mol/cm}^2$, $9.0 \times 10^{-10} \text{ mol/cm}^2$ and $7.5 \times 10^{-10} \text{ mol/cm}^2$ for **19**, **20** and **21** respectively indicating that the films are larger than a monolayer of MPcs on the electrodes.

Conclusion

The phenylthio derivatized Pcs were deposited on the gold electrodes through self-assembly, the films showed blockage of Faradaic processes confirming the existence of a film on the electrode surface. The amino derivatized Pcs were successfully adsorbed on a glassy carbon electrode through electropolymerization.

Chapter 5

Electrocatalysis

5. Electrocatalysis

The phthalocyanine modified electrodes discussed in Chapter 4 were used as electrochemical sensors for the electrocatalytic oxidation of nitrite and L-cysteine. This chapter will explore the catalytic responses and kinetic parameters of the modified electrodes.

5.1 Nitrite electrocatalytic oxidation

5.1.1 SAM modified gold electrodes (12-15 SAMs)

At bare electrodes the nitrite oxidation reaction exhibits slow electron transfer kinetics and occurs at potentials substantially higher than its thermodynamic redox potential. Phthalocyanine modified electrodes are thus used as electron-transfer mediators with the aim of lowering the overpotential and increasing catalytic currents. Nitrite oxidation reactions were carried out in pH 7.4 buffer as disproportionation of nitrite to nitric oxide (NO) is insignificant at this pH and thus the catalysis monitored is that of nitrite oxidation. Figure 5.1 shows the electro-catalytic responses of complexes **12**, **13**, **14** and **15** SAM modified gold electrodes. There was no oxidation of nitrite at the bare electrode within the potential range applied (0 - 0.7V), nitrite oxidation on bare gold electrode has been reported at potentials higher than 0.8 V [50]. On the SAM modified electrodes, high current responses and clear nitrite oxidation peaks were observed. Complex **12** showed the best catalytic response both in terms of overpotential lowering (Table 5.1) and current

enhancement. Cathodic peaks at $\sim 0.2\text{V}$ were observed for complex **12** and **14** SAMs, these peaks were attributed to phthalocyanine reduction peaks.

Table 5. 1: Parameters for the electrocatalytic oxidation of 1mM nitrite at modified electrodes with complexes **12-15** and **19-21** in pH 7.4 buffer solution.

Complex	E_p/V (vs. Ag AgCl)	I_p (μA)	% I_p decrease (%)	Limit of detection (μM)	b (mV/decade)	α	k ($\text{cm}\cdot\text{s}^{-1}$)	n
12 (Co)	0.56	15.8	20	1.38	96	0.38	0.131	2.4
13 (Co)	0.58	8.6	14	1.35	86	0.31	0.052	1.6
14 (OHMn)	0.58	12.7	24	1.96	196	0.69	0.04	2.6
15 (OTi)	0.66	12.5	15	2.38	218	0.73	0.041	2.7
19 (Co)	0.35	13	7	1.73	100	0.42	0.056	1.7
20 (OHMn)	0.69	36	15	0.50	112	0.47	0.024	1.8
21 (OTi)	0.67	43.3	57	0.58	132	0.55	0.025	1.9

The SAM modified electrodes showed resistance to passivation when cycled in 1mM nitrite solution a number of times (Figure 5.2). The percentage difference between the first and the second scan is shown on Table 5.1 with values less than 25%. The currents for nitrite oxidation on disk electrodes could be regenerated to $> 65\%$ by rinsing the electrode in pH 7.4 buffer.

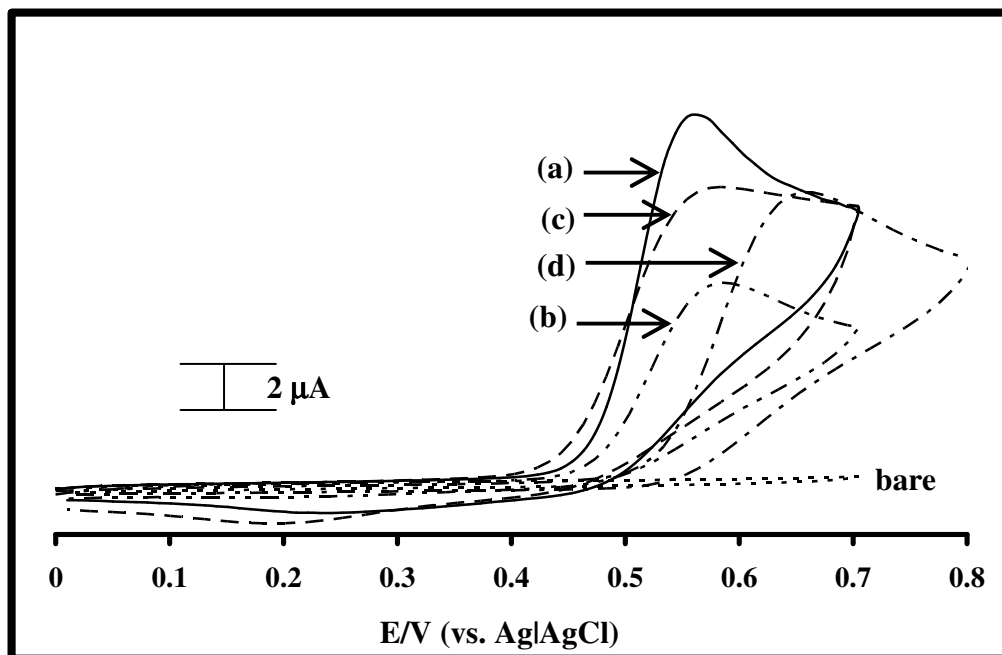


Figure 5. 1: Cyclic voltammograms of bare Au, complex (a) **12**, (b) **13**, (c) **14** and (d) **15** SAM electrodes for 1mM nitrite oxidation in pH 7.4 buffer. Scan rate = $100mVs^{-1}$.

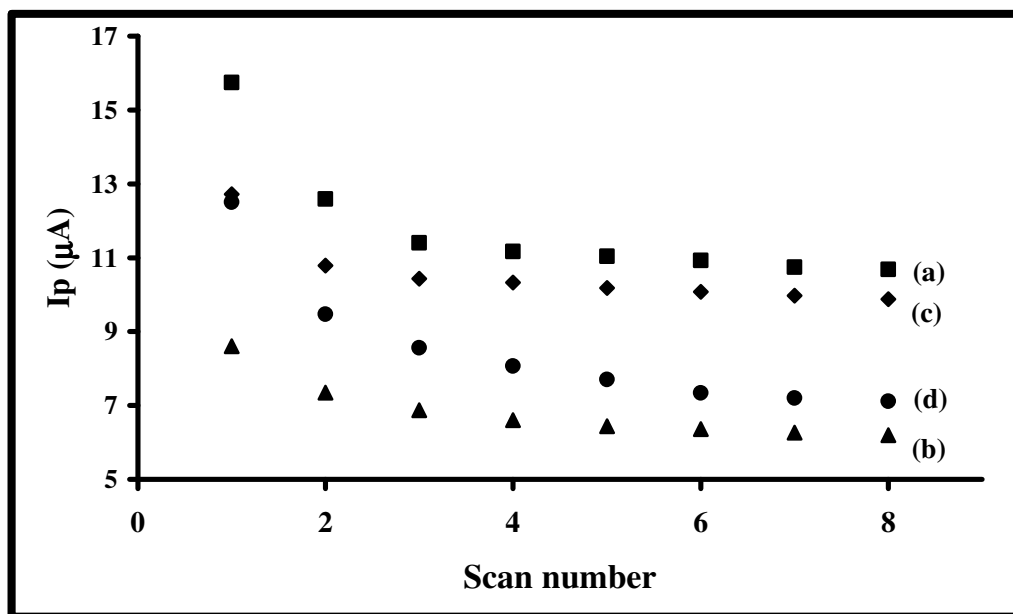


Figure 5. 2: Peak current variation with scan number for the electrocatalytic response of 1mM nitrite on complex (a) **12**, (b) **13**, (c) **14** and (d) **15** SAM modified electrodes in pH 7.4 buffer. Scan rate = $100mVs^{-1}$.

A linear relationship between the peak current (I_p) and square root of scan rate (v) for a fixed nitrite concentration was observed, Figure 5.3, for all SAM modified electrodes confirming a diffusion controlled nitrite electrooxidation. A linear dependence of nitrite concentration (Figure 5.4 for **12**) on currents was also observed for the SAM modified electrodes where the detection limits for nitrite analysis were determined using 3σ criterion. Limits of detection ranged from 1.35×10^{-6} to 2.38×10^{-6} M for **12** to **15**.

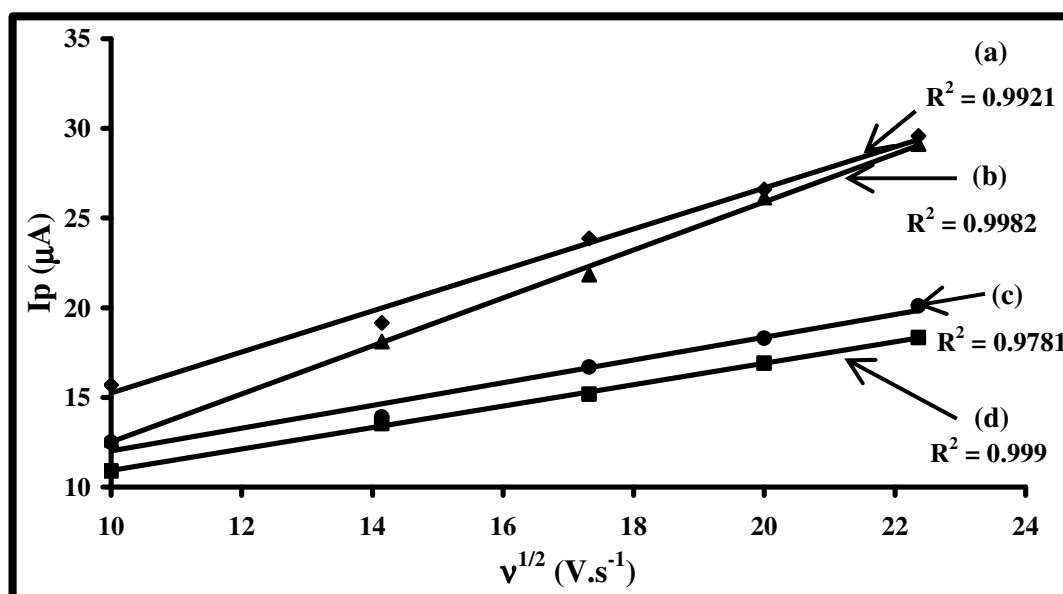


Figure 5. 3: Peak current variation with square root of scan rate for the electrocatalytic response of 1mM nitrite on complex (a) **12**, (b) **13**, (c) **14** and (d) **15** SAM modified electrodes in pH 7.4 buffer.

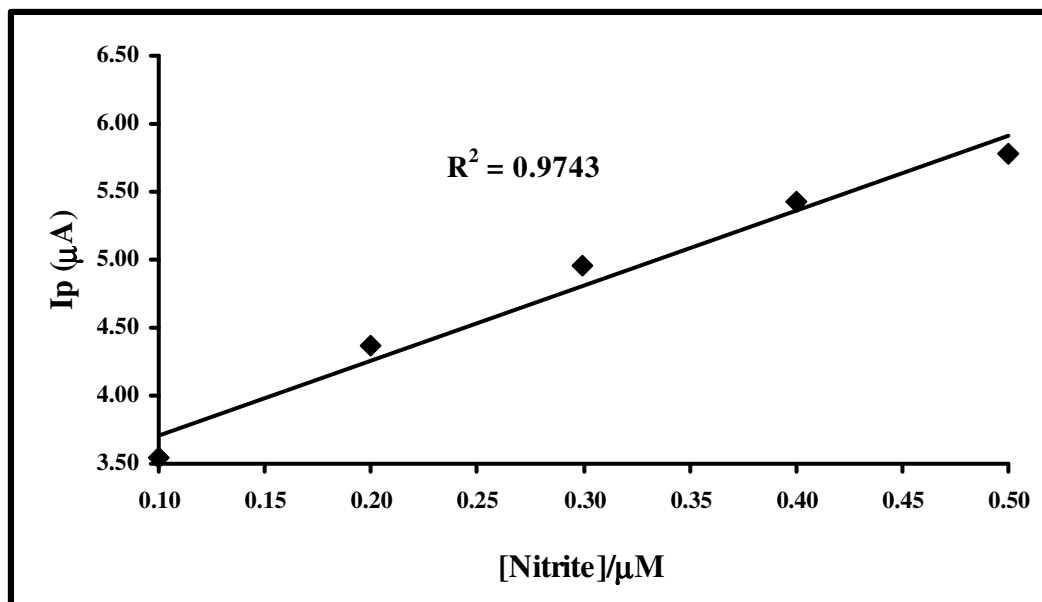


Figure 5. 4: Plot of peak current versus nitrite concentration on complex **12** modified electrode in pH 7.4 buffer.

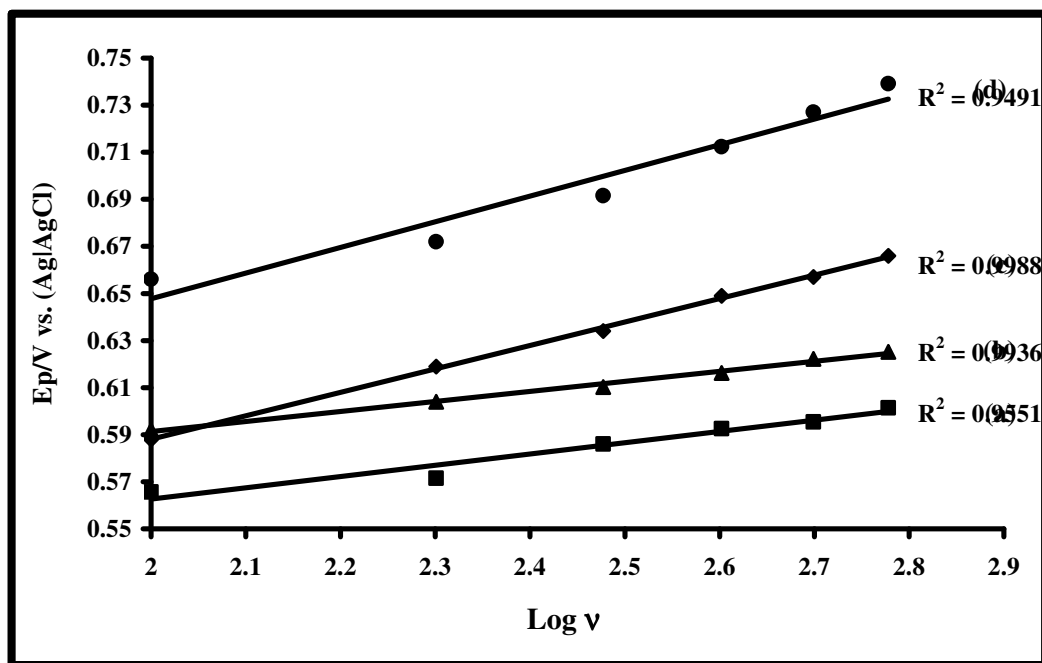


Figure 5. 5: Peak potential variation with logarithm of scan rate for the electrocatalytic response of 1mM nitrite on complex (a) **12**, (b) **13**, (c) **14** and (d) **15** SAM modified electrodes in pH 7.4 buffer.

Further analyses of the electrocatalytic experiments were determined from plots of E_p vs. log of scan rate (log v), Figure 5.5, for a totally irreversible process and using equation 5.1 [73]

$$E_p = \frac{2.3RT}{2(1-\alpha)n_a F} \log v + K \quad 5.1$$

where α is the transfer coefficient, n_a is the number of electrons involved in the rate determining step, v is the scan rate, K is a constant, R is the gas constant, T is the temperature, F is Faraday's constant and E_p is the peak potential. The Tafel slope (b) is defined by: $b = 2.3RT/(1-\alpha)n_a F$. Tafel slopes for nitrite electrocatalysis were determined and ranged between 86 - 218. mV/decade, Table 5.1, for **12-15**.

Tafel slopes of ~120 mV/decade suggest that the transfer of the first electron is the rate-determining step whereas slopes of 60 mV/decade suggest a fast electron transfer is preceded by a slow chemical step (rate determining step). For **12** and **13** the chemical step is the rate determining step and for **14** and **15** the first electron transfer is the rate determining step. For **14** and **15** the large Tafel slope values (~ 200 mV/decade) suggest either a strong substrate-ligand interaction [89] or chemical reactions coupled to electrochemical steps [60].

The resulting transfer coefficients, α , Table 5.1, imply that the oxidation of nitrite on complex **15** SAM modified electrode is favourable in comparison to the other electrodes since it has the highest α value. The rate at which the electrocatalyses take place, i.e. heterogeneous rate constants, k , were obtained from equation 5.2 [73]

$$K = E^{o'} + \frac{RT}{(1-\alpha)n_a F} \times \left[0.78 + \frac{2.3}{2} \log \left(\frac{(1-\alpha)n_a F D}{k^2 RT} \right) \right] \quad 5.2$$

where $E^{o'}$ is the formal potential, D is the nitrite diffusion coefficient ($2.1 \times 10^{-5} \text{ cm}^2 \cdot \text{s}^{-1}$ [132, 133]) and the remaining symbols are as they were described before. The electrooxidation of nitrite on complex **12** SAM had the highest k value suggesting that this electrode efficiently catalyses nitrite than the other electrodes. The total number of electrons (n) transferred during the electrocatalyses was determined from equation 5.3 [73],

$$I_p = 2.99 \times 10^5 n [(1 - \alpha) n_a]^{1/2} A C_o D^{1/2} \nu^{1/2} \quad 5.3$$

where C_o is the concentration of the nitrite and the remaining symbols were described above. A total of ~2 electrons were obtained for all electrodes, therefore suggesting that the nitrite oxidation result in nitrate (NO_3^-) as the product.

An attempt was made to calculate Tafel slope values employing rotating disk electrode (RDE) experiments which usually give better results. The RDE plots did not give plateaus hence were not employed.

Studies for the interaction between nitrite and complex **12**, **13**, **14** and **15** were carried out using spectroscopy. Even though these studies are done in solution, they give an indication of nitrite binding to adsorbed MPCs. Figure 5.6 (a) shows the spectral changes observed when nitrite was added to complex **12** in DMF. The Q-band shifted from 695 to 702 nm. This change could be due to axial coordination of nitrite to **12** since small changes in Q-band reflect axial ligation or it could be the oxidation of the central metal from Co^{II} to Co^{III} [23, 134]. The color of the Pc solution changed from an initial blue color to green by the end of the reaction. In order to check if oxidation of Co^{II} to Co^{III}

occurred, a reducing agent (NaBH_4) was added at the end of the reaction and as shown in Figure 5.6 (b) there was a shifting of the Q-band from 702 to 710 nm with an isobestic point at 600nm. The Q-band was broad and there was a charge transfer band formed at 470nm, this band is typical for $\text{Co}^{\text{I}}\text{Pc}$ complexes. The original spectrum in Figure 5.6 (a) was not regenerated suggesting that the observed spectral changes in this figure are due to nitrite coordination to **12** and not $\text{Co}^{\text{III}}\text{Pc}$ formation. At the end of this reaction the color of the solution went from green to a dirty green (almost brown) color. Similar spectral changes were observed for complex **13**.

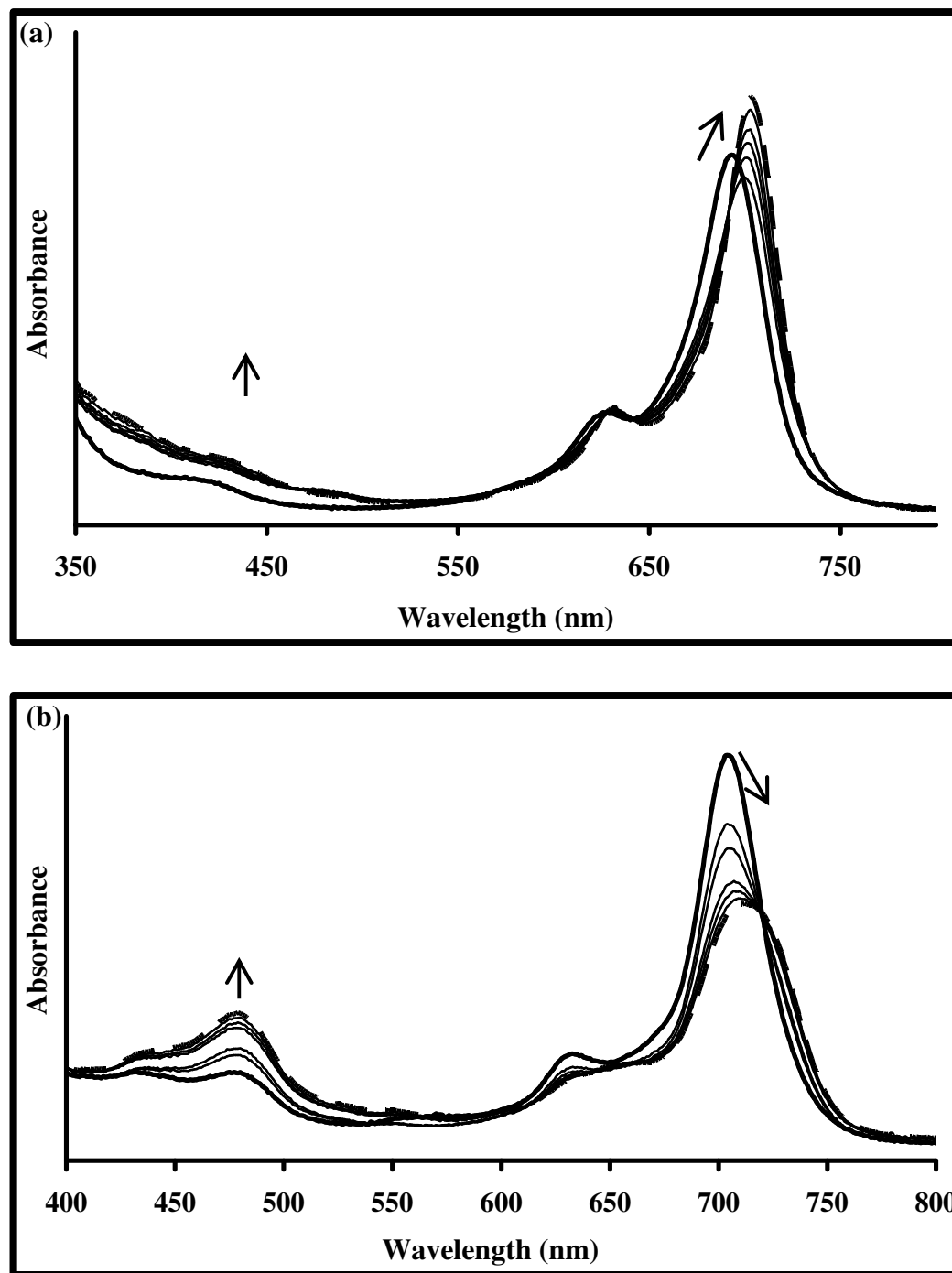
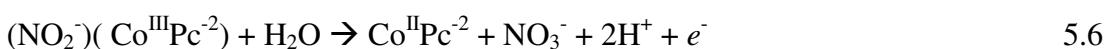
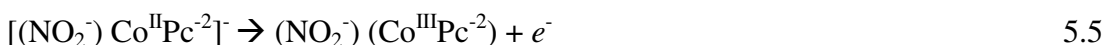


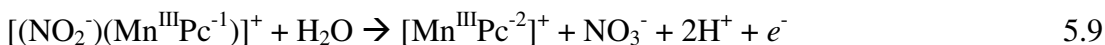
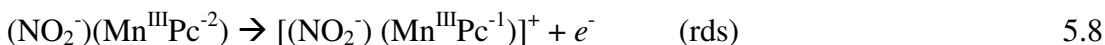
Figure 5. 6: Spectroscopic changes of (a) **12** ($\sim 1 \times 10^{-6}$ M) observed on addition of 1mM nitrite solution in DMF to solution (solid line) initial spectrum, (dashed line) final spectrum after 5 minutes, and (b) on addition of NaBH₄ to the final spectrum in (a).

Based on the above spectral changes, Tafel slopes obtained from cyclic voltammetric experiments and the total number of electrons involved in the overall reaction, the following reaction mechanism is proposed for complexes **12** and **13** in Scheme 5.1 (eqs 5.4-5.6). An electrochemical step is preceded by a chemical reaction (5.5) which is axial ligation.



Scheme 5. 1: Proposed mechanism for the catalytic oxidation of nitrite on complex **12** and **13** SAM modified electrodes.

A 2 nm shift in the Q-band of complex **14** (Mn^{2+}Pc) was observed upon the addition of nitrite to the solution (figure not shown), this shift suggests the coordination of nitrite on the central metal. For **14**, the electrochemical step was rate determining. Based on observed spectral changes and Tafel slope values the following reaction mechanism is proposed as shown in Scheme 5.2 (equations 5.7-5.9).



Scheme 5. 2: Proposed mechanism for the catalytic oxidation of nitrite on complex **12** SAM modified electrode.

Complex **15** has been shown to interact with nitrite and a reaction mechanism has been proposed with Tafel slope values >120 mV/decade and two electrons being transferred during catalysis [49].

5.1.2 MTAPc modified electrodes (*poly 19-21*)

The modified glassy carbon electrodes were investigated for catalysis of nitrite electrooxidation in pH 7.4 phosphate buffer solution. Figure 5.7(a) shows the responses obtained for nitrite oxidation at the bare and *poly-19* modified electrode, Figure 5.7(b) shows nitrite oxidation at the bare, *poly-20* and *poly-21* modified electrodes. The oxidation peaks of *poly-19*, *poly-20* and *poly-21* in the absence of nitrite are observed between 0.1 and 0.5 V, Chapter 4, and the bare GCE showed nitrite oxidation as a broad peak near 0.96 V. The nitrite peak on bare in Figure 5.7(a) is not observed due to the narrow potential range.

It can be seen that the electrocatalytic oxidation of nitrite is effectuated by the modified electrode as evidenced by the decrease in the overpotential and increase in catalytic currents on *poly-19*, *poly-20* and *poly-21*. The overpotential was lowered from 0.96 V vs. Ag|AgCl at the bare electrode to 0.35, 0.69 and 0.66 V at the *poly-19*, *poly-20* and *poly-21* modified electrodes respectively. Thus the central Mn and Ti metal did not differ much in terms of lowering the nitrite oxidation potential and Co showed the best activity in that it gave the lowest oxidation potential. High catalytic currents were observed for *poly-20* and *poly-21* compared to *poly-19* as can be seen in Figure 5.7 (a) and (b).

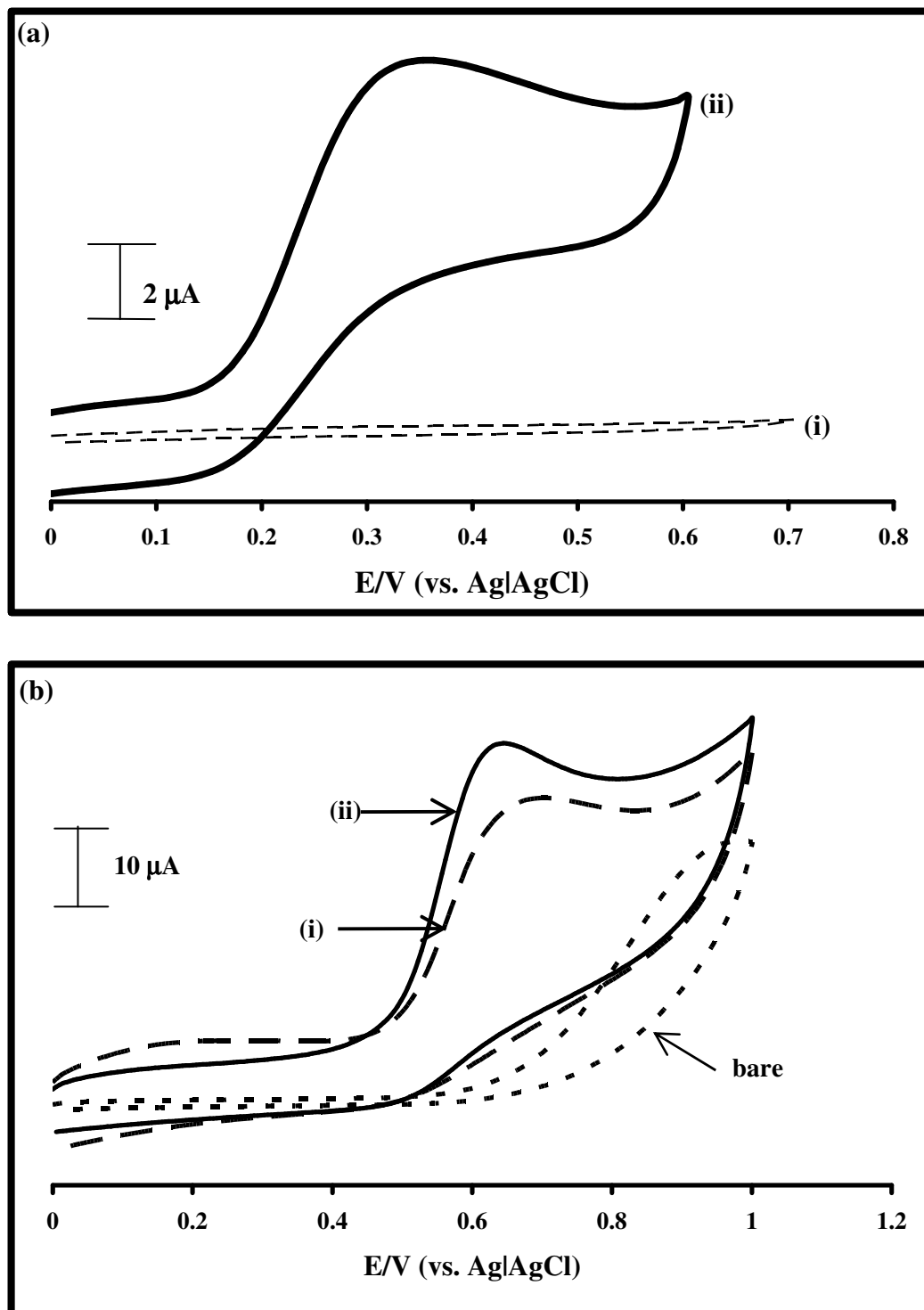


Figure 5. 7: Cyclic voltammograms of oxidation of 1 mM nitrite (a) on bare GCE, (i) *poly-19* modified GCE (ii) and (b) on on bare GCE, (i) *poly-20* and (ii) *poly-21* modified GCE in pH 7.4 phosphate buffer solution. Scan rate = 100 mVs⁻¹.

Figure 5.8, Table 5.1, shows that there was a 7% decrease in the catalytic current of *poly-19* from the first to the second scan whereas *poly-21* and *poly-20* showed a 57% and 15% decrease respectively, thus *poly-19* is the most stable catalyst. Plots of peak current vs. the square root of scan rate, Figure 5.9, were linear for the catalysts, suggesting diffusion-controlled processes.

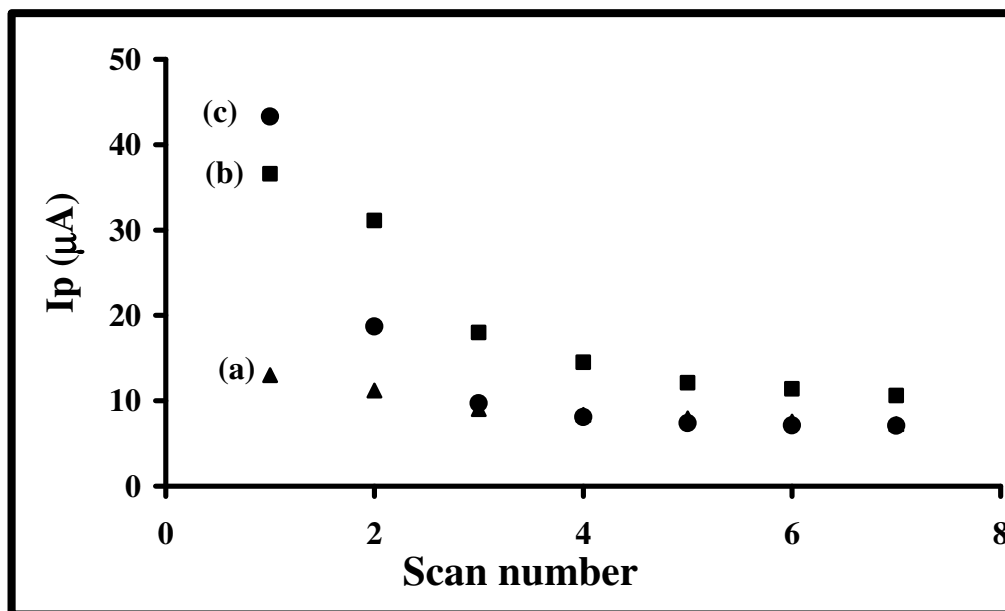


Figure 5. 8: Peak current variation with scan number for the electrocatalytic response of 1mM nitrite on *poly* (a) **19**, (b) **20**, and (c) **21** modified electrodes in pH 7.4 buffer. Scan rate = $100\text{mV}\cdot\text{s}^{-1}$.

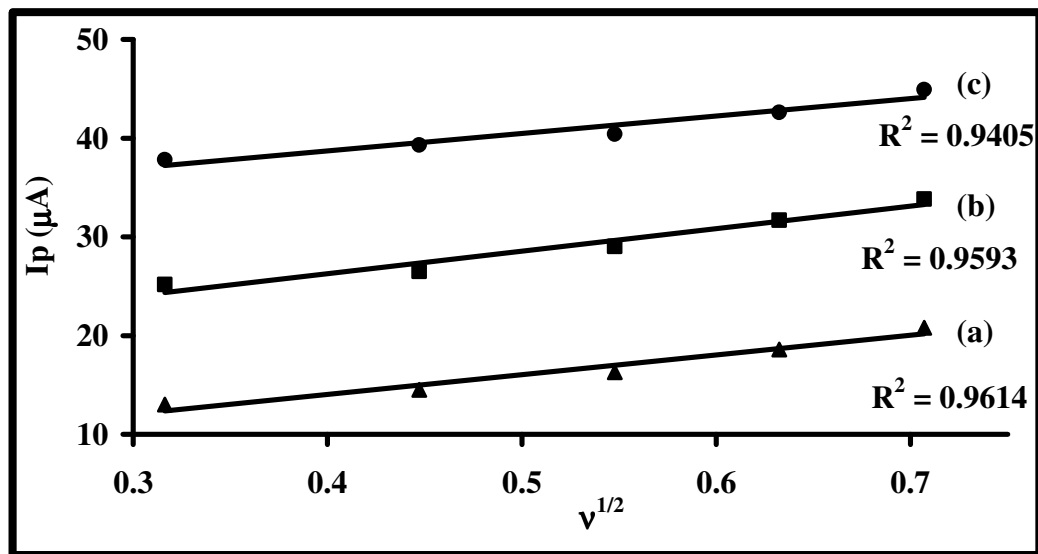


Figure 5. 9: Peak current variation with square root of scan rate for the electrocatalytic response of 1mM nitrite on *poly* (a) **19**, (b) **20**, and (c) **21** modified electrodes in pH 7.4 buffer.

Plots of E_p vs. log of scan rate ($\log v$), Figure 5.10 were used to determine kinetic parameters using equation 5.1. Tafel slope values obtained ranged between 55 – 335 mV/decade. Tafel slope values were also determined by RDE below and they are the ones shown in Table 5.1. Equation 5.2 was used to calculate the heterogeneous rate constants; *poly-19* (Co^{II} central metal) had the highest value suggesting that this electrode is more efficient at catalysis than the other MTAPc (Table 5.1) as was the case for complexes **12-15** where **12-SAM** (also Co^{II} central metal) had the highest k value. The total number of electrons transferred for the electrooxidation process was determined (using equation 5.3) to be close to 2 for all catalysts confirming nitrite oxidation to nitrate.

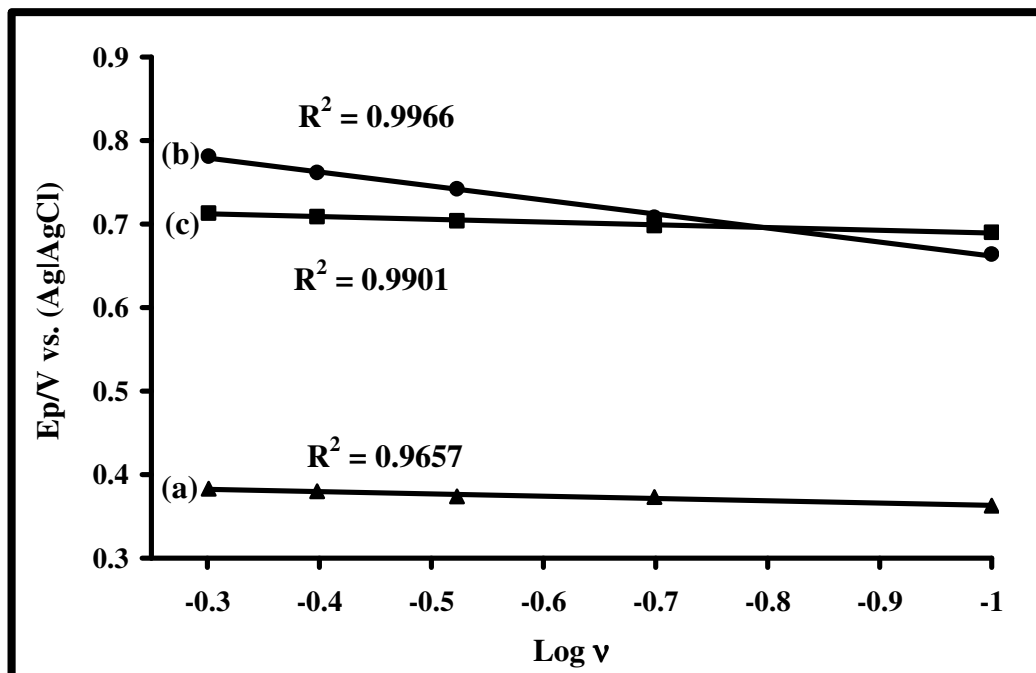


Figure 5. 10: Peak potential variation with logarithm of scan rate for the electrocatalytic response of 1mM nitrite on *poly* (a) **19**, (b) **20** and (c) **21** modified electrodes in pH 7.4 buffer.

Kinetic studies of nitrite oxidation catalysed by the *poly*-MTAPcs were also carried out using rotating disc electrode voltammetry, Figure 5.11. Plateaus were obtained in this case hence Tafel slopes were estimated. Kinetic parameters were determined based on Tafel equation, equation 5.10,

$$\eta = a + b \log i \quad 5.10$$

where η is the overpotential, a is the exchange current density (i_0) and b is the Tafel slope, which were obtained from plot of logarithm of kinetic current versus overpotential (η), Figure 5.12. Kinetic current (i_K) is given by $i_k = (i_m \times i_L)/(i_m - i_L)$. i_K is the current when the system is under complete kinetics, i.e. analyte transport is governed by rotation

of the electrode and not diffusion, i_L is the limiting current (plateau in RDE voltammogram) and i_m is measured current and it has to be less than 5% of i_L . Using Figure 5.12, Tafel slopes for nitrite oxidation electrocatalysis were determined to be 100, 112 and 132 mV/decade for **19**, **20** and **21** respectively, confirming that the transfer of the first electron is rate determining. The transfer coefficients, α , were determined to be 0.42, 0.47 and 0.55 respectively for **19**, **20** and **21**, Table 5.1, implying that there is an equal probability that the reaction may go forward forming products or backwards to the reactants.

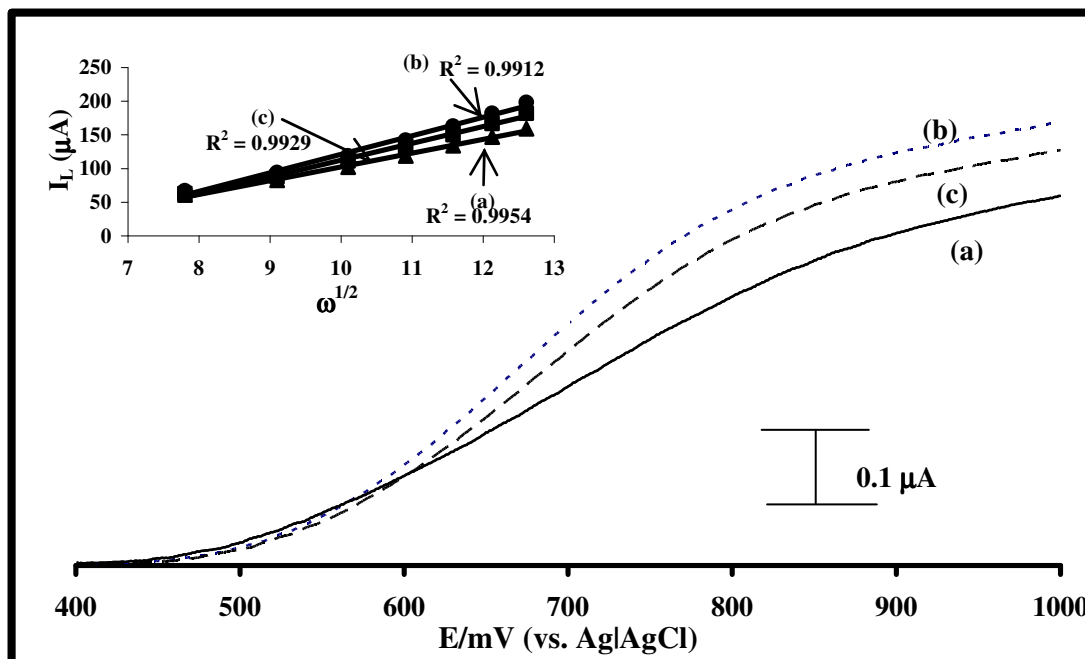


Figure 5. 11: Hydrodynamic voltammograms of nitrite (1mM) oxidation on *poly* (a) 19, (b) 20 and (c) 21 modified electrodes. Rotation rate 800 rpm scan rate 20 mVs^{-1} . Insets are the corresponding Levich plots.

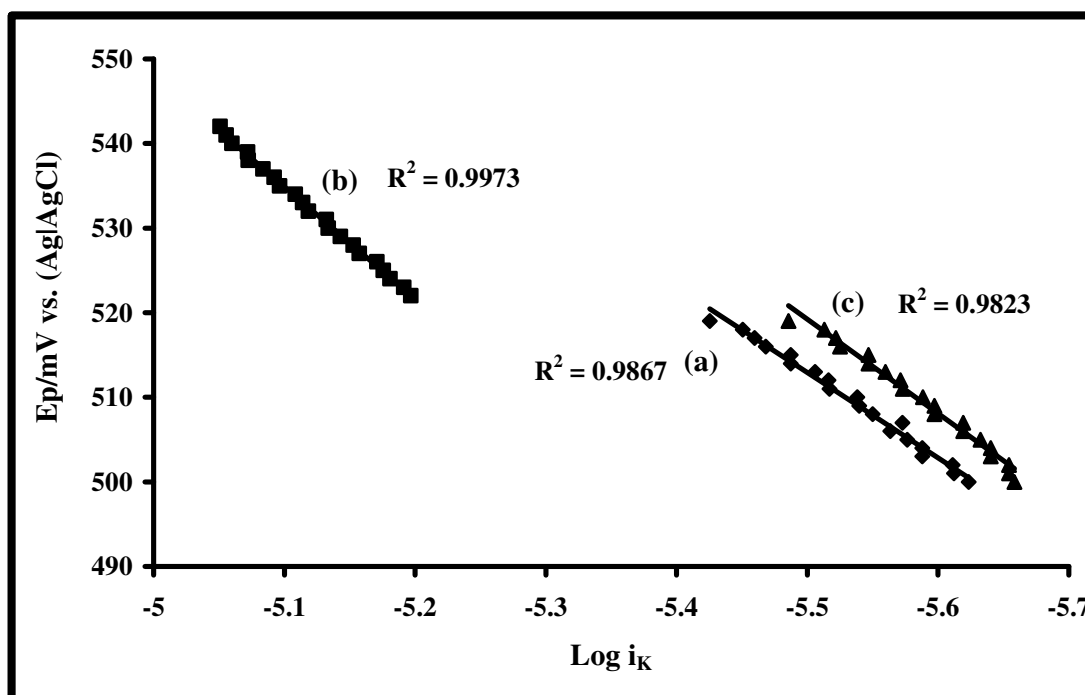
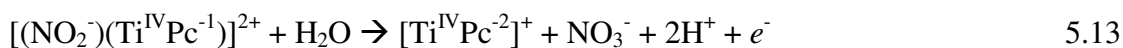
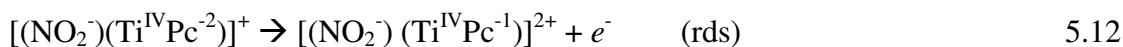


Figure 5. 12: Tafel plot for nitrite oxidation on *poly* (a) 19, (b) 20 and (c) 21 modified electrodes for 1mM nitrite in pH 7.4 buffer solution.

Interaction between nitrite and *poly*-MTAPc electrodes was evidenced by small shifts cyclic voltammogram of the polymer redox processes in the presence of small concentrations of nitrite (Figure not shown). Such small shifts indicate that redox processes are occurring on different complexes due to axial ligation. Mechanisms for nitrite oxidation can be proposed based on the above findings: two electrons are transferred leading to formation of nitrate, the first electron is involved in the rate-determining step, there is coordination between nitrite and the complexes.

For CoTAPc, the proposed mechanism is the same as Scheme 5.1. For (OH)MnTAPc, the proposed mechanism is the same as Scheme 5.2. For OTiTAPc, the proposed mechanism is the same as for the peripherally substituted counterpart reported before [48] which is shown in Scheme 5.3 (eqs 5.11-5.13).



Scheme 5. 3: Proposed mechanism for the catalytic oxidation of nitrite on *poly*-**21** modified electrode. Axial oxygen left out for clarity.

5.1.3 Nitrite detection in a food sample

It is clear from both cyclic voltammetry and hydrodynamic experiments that complex **19** is the best catalyst for nitrite electrooxidation in terms of overpotential reduction. This electrode was thus used for the analysis of nitrite in a sausage sample. The sausage sample was bought from a local supermarket and pre-treated according to the described procedure in experimental section. The standard addition method was used for nitrite

concentration determination in the sausage sample, Figure 5.13 shows a peak at 0.78V at the bare electrode, this peak increased in current on *poly-19* (considering background current). When modified with *poly-19*, the electrode proved to be an efficient nitrite sensor as the overpotential was reduced from 0.78V at the bare electrode to 0.64V on *poly-19*. Figure 5.14 shows the nitrite peak current increase on the modified electrode with increasing nitrite concentration.

The concentration of nitrite found in the sausage sample was calculated to be 59.13 ppm, well within the limit for cured meat products [92].

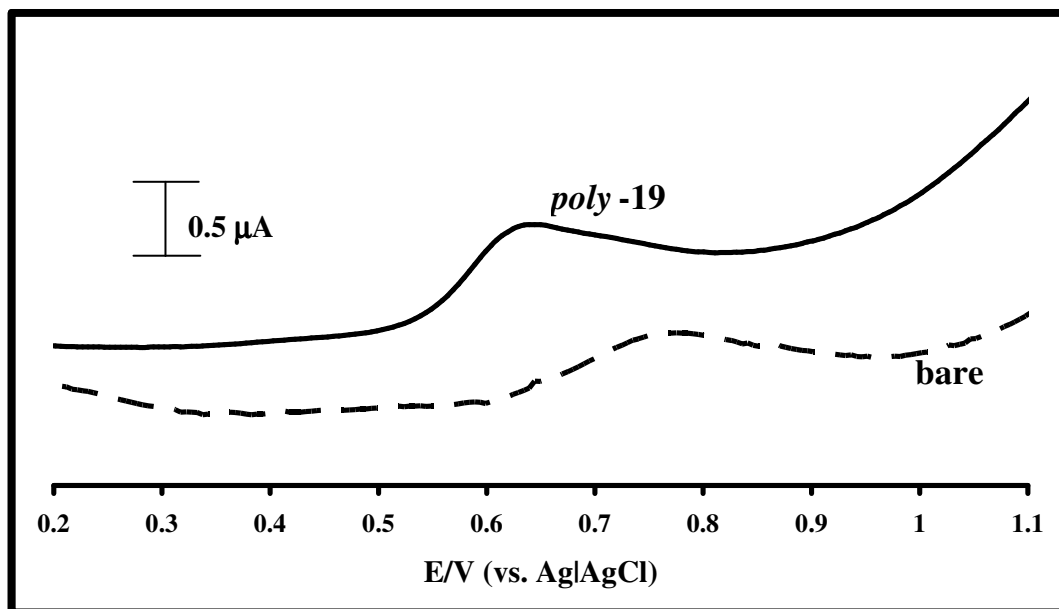


Figure 5. 13: Differential pulse voltammograms of an unmodified glassy carbon electrode (dashed line) and *poly-19* modified electrode in a sausage sample.

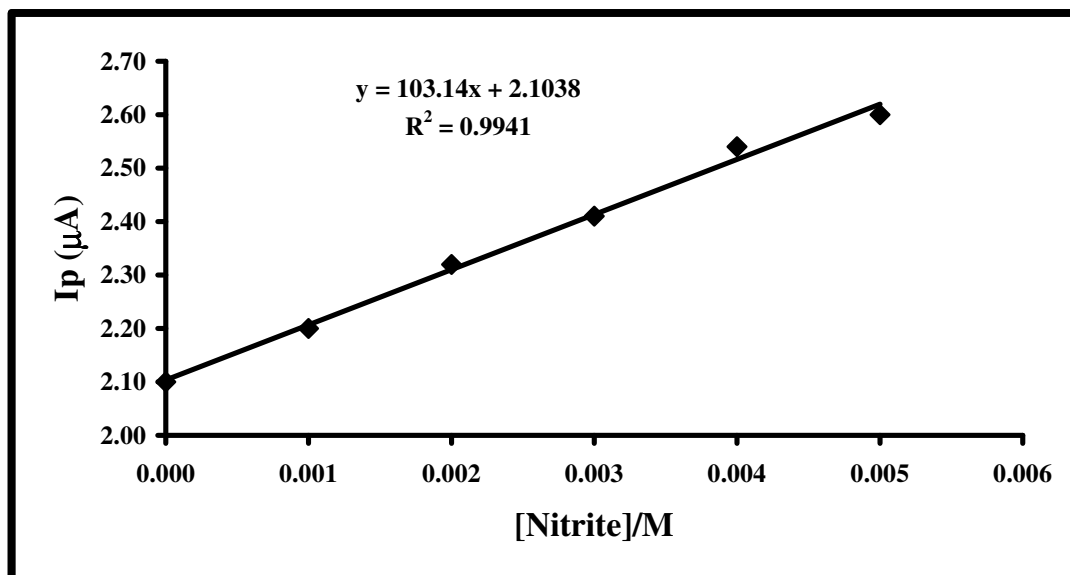


Figure 5. 14: A plot showing the linear dependence of the peak current with increasing nitrite concentration in a sausage sample.

5.2 L-cysteine electrocatalytic oxidation

Gold disk, gold ultramicro cylinder and gold coated fiber electrodes were used for L-cysteine oxidation at pH 4. At this pH L-cysteine is catalysed by $\text{Co}^{\text{III}}/\text{Co}^{\text{II}}$ and not $\text{Co}^{\text{II}}/\text{Co}^{\text{I}}$ [40]. Cysteine concentration of 1mM was employed for all electrodes for comparison purposes.

5.2.1 L-cysteine oxidation on SAM modified gold disk electrodes

Figure 5.15 shows cyclic voltammograms of pH 4 buffer solution containing 1mM of L-cysteine on bare and SAM modified Au disk electrodes using complexes **12**, **13**, **14** and **15**. The bare electrode shows no cysteine oxidation peak. Clear peaks and large increase in currents are observed due to catalytic cysteine oxidation on all the SAMs. Complex **12** SAM showed the lowest overpotential reduction and complex **15** SAM showed the highest enhancement of catalytic currents, Table 5.2. A linear relationship between the peak current (I_p) and square root of scan rate (v) was observed, Figure 5.16 confirming a diffusion controlled L-cysteine electrooxidation. The linear behavior of this plot was observed for all SAM modified electrodes.

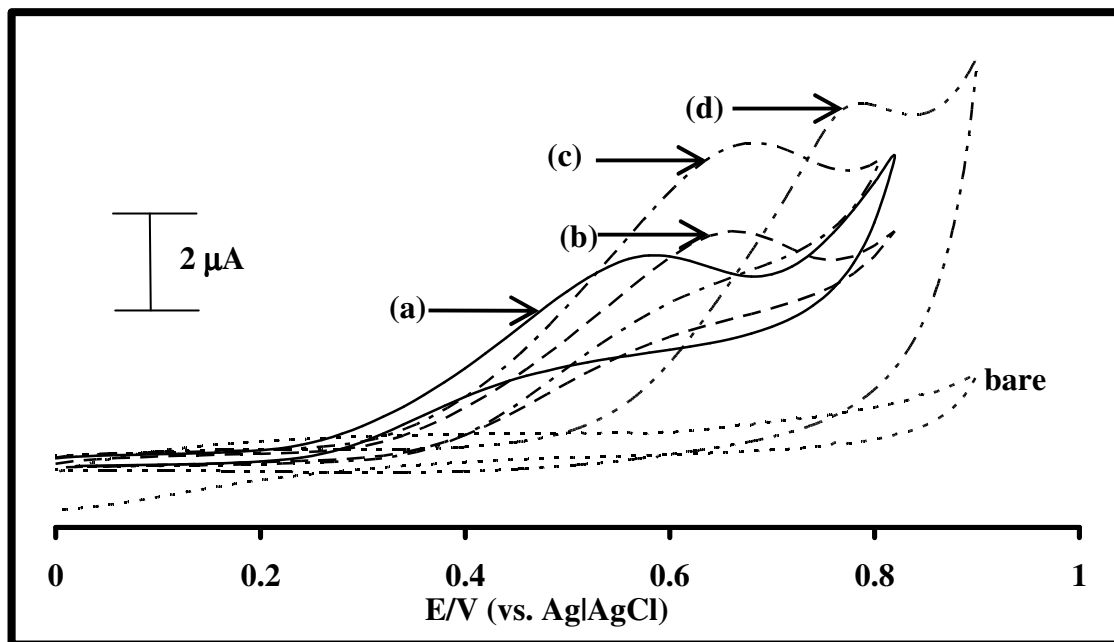


Figure 5. 15: Cyclic voltammograms of bare Au, complex (a) **12**, (b) **13**, (c) **14** and (d) **15** SAM Au disk electrodes for 1mM L-cysteine oxidation in pH 4 buffer. Scan rate = $100\text{mV}\cdot\text{s}^{-1}$.

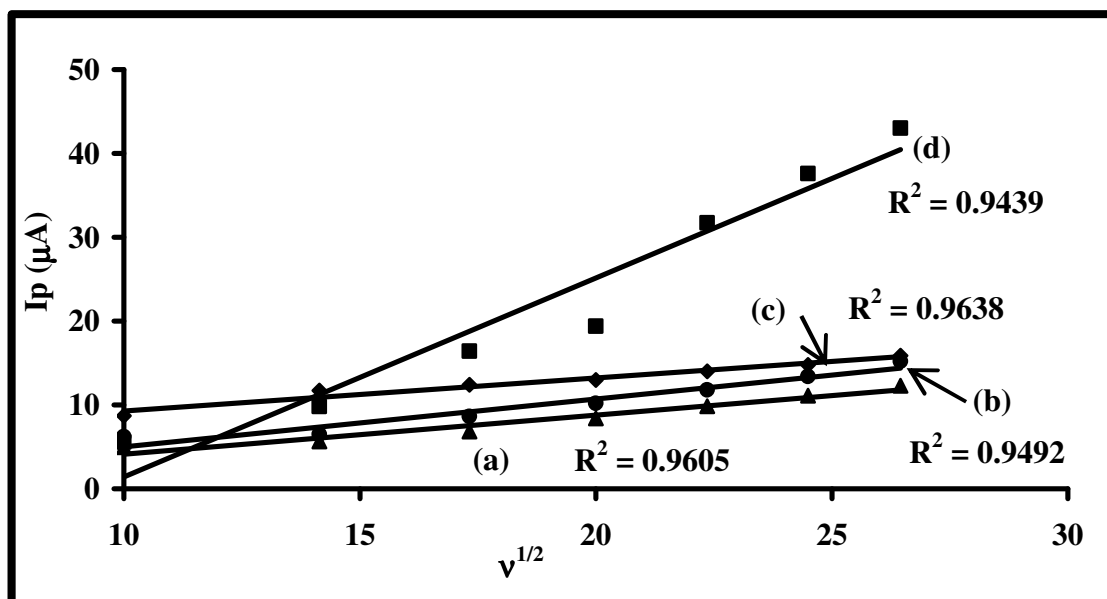


Figure 5. 16: Peak current variation with square root of scan rate for the electrocatalytic response of 1mM L-cysteine on complex (a) **12**, (b) **13**, (c) **14** and (d) **15** SAM modified Au disk electrodes in pH 4 buffer.

Table 5. 2: Parameters for the electrocatalytic oxidation of 1mM L-cysteine at SAM modified gold electrodes with complexes **12**, **13**, **14** and **15** in pH 4 buffer solution.

Complex	E_p (V vs. Ag AgCl)	I_p (μ A)	% I_p decrease (%)	Limit of detection (μ M)	b (mV/decade) (a)	α	K ($\text{cm}\cdot\text{s}^{-1}$)	n (a)
12-disk	0.55	5.64	23	1.86	173 (173)	0.66	0.052	0.75 (0.50)
13-disk	0.65	6.33	24	1.95	184 (199)	0.68	0.049	0.68 (0.48)
14-disk	0.67	8.08	32	0.62	123 (142)	0.52	0.003	1.1 (1.0)
15-disk	0.78	9.91	34	1.06	128 (118)	0.54	0.054	1.4 (0.67)
12- UMCE	0.84	7.28	23	-	-	-	-	-
13- UMCE	0.90	7.63	32	-	-	-	-	-
12-fiber	0.62	257.7	37	-	-	-	-	-
13-fiber	0.77	594.6	67	-	-	-	-	-

(a) number in brackets obtained from RDE experiments

A 23% current decrease was observed for cysteine oxidation on SAM of complex **12** on Au disk electrode, after the first scan Figure 5.17, thereafter the current stabilized. For complex **13** on Au disk electrode, there was a 24% decrease of the current before it stabilized. Complex **14** showed a 32% decrease whereas complex **15** showed a 34% loss in current, Table 5.2. Thus complex **12** shows better stability closely followed by **13**. The currents for cysteine oxidation on disk electrode could be regenerated to > 65% by rinsing the electrode in pH 4 buffer.

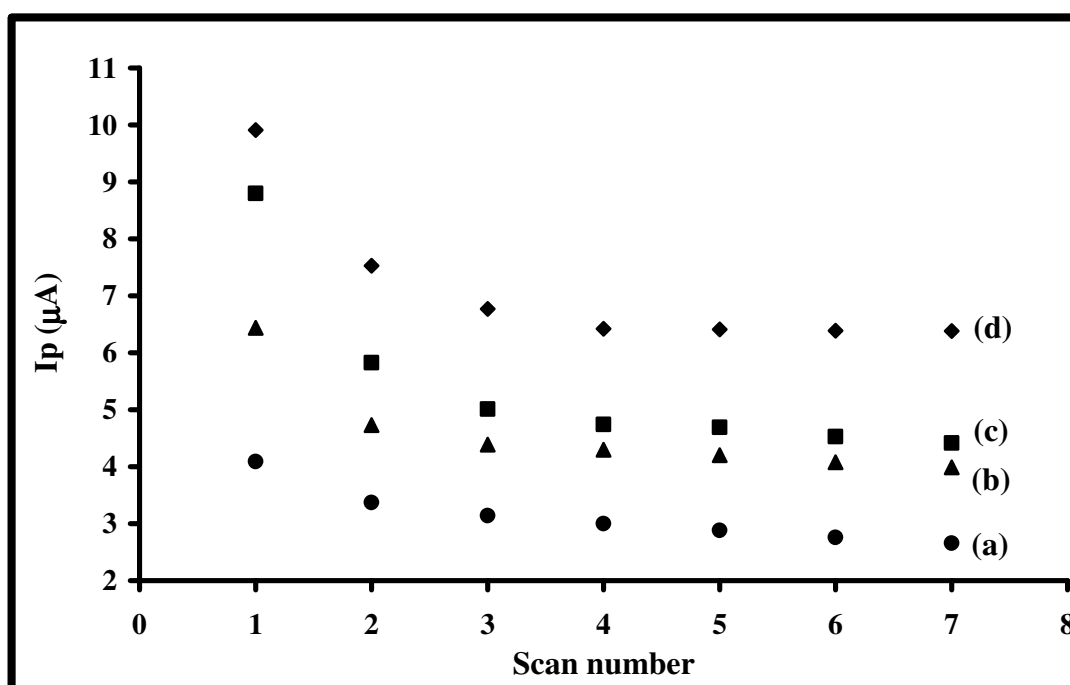


Figure 5. 17: Peak current variation with scan number for the electrocatalytic response of 1mM L-cysteine on complex (a) **12**, (b) **13**, (c) **14** and (d) **15** SAM modified Au disk electrodes in pH 4 buffer. Scan rate = 100mVs^{-1} .

Tafel slopes were determined from linear plots of $\log v$ vs. E_p (Figure 5.18) using equation 5.1. Tafel slope values ranged between 123 – 184 mV/decade suggesting that all

SAM electrodes catalyze L-cysteine via the same reaction mechanism. Transfer coefficient values were found to range between 0.52 – 0.68 and k values indicated that **15** was the most efficient catalyst as shown in Table 5.2. The total number of electrons transferred was close to 1, confirming the electrooxidation of L-cysteine to cystine, which is a one electron process.

Figure 5.19 shows a linear dependence of cysteine concentration on peak currents of complex **12** SAM, similar behavior was observed for the rest of the SAM modified electrodes. The detection limits for cysteine analysis were determined using 3σ criterion and were of the order 10^{-6} M, Table 5.2, which is in the range as reported before [65].

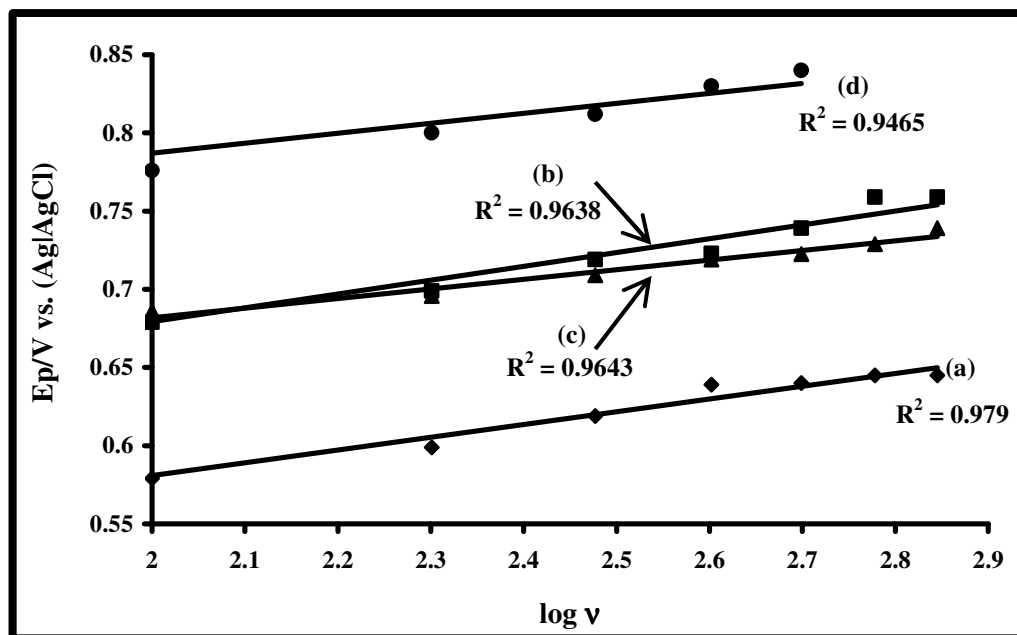


Figure 5. 18: Peak potential variation with logarithm of scan rate for the electrocatalytic response of 1mM L-cysteine on complex (a) **12**, (b) **13**, (c) **14** and (d) **15** SAM modified electrodes in pH 4 buffer. Scan rate = 100mV.s⁻¹.

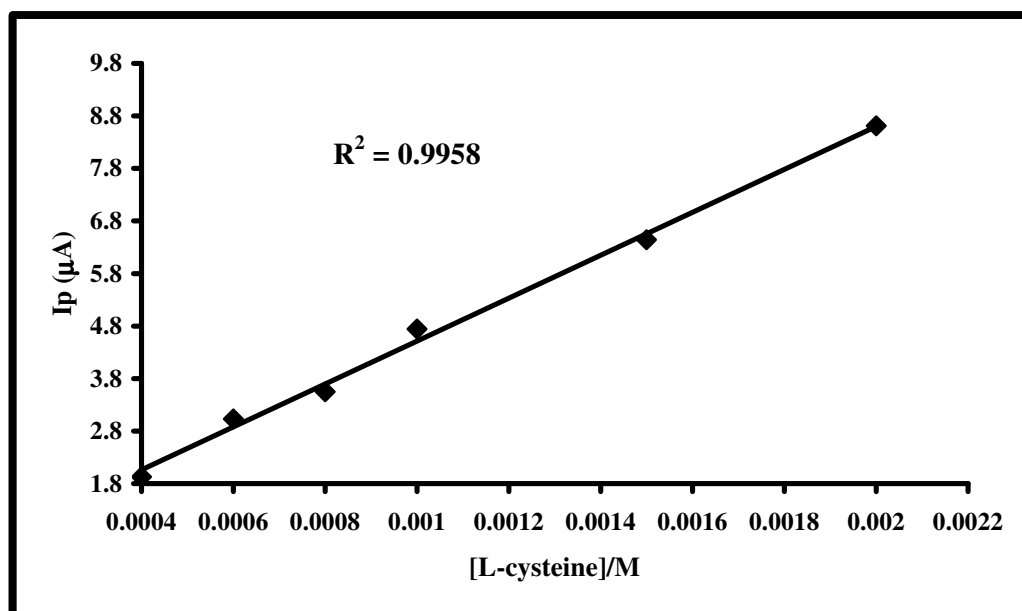


Figure 5. 19: Plot of peak current versus concentration for L-cysteine in pH 4 buffer on SAM of complex **12**.

Figure 5.20 shows typical RDE curves obtained for cysteine oxidation on complex **12**, **13**, **14** and **15** SAM modified electrodes at 800 rpm. The inset shows the Levich plots, showing that the Levich equation is obeyed for all SAMs. The corresponding Tafel slope values were obtained from the plot of E vs. $\log I_k$ (figure not shown) the values were found to be between 118 – 199 mV/decade for the SAM modified electrodes, Table 5.1. The values of the Tafel slopes suggest that the first one electron transfer is rate determining, confirming the well-known mechanism for cysteine oxidation on CoPc complexes [40]. The values of the Tafel slope were similar to those obtained from cyclic voltammetry using equation 5.1, employed for irreversible- diffusion controlled catalytic reaction.

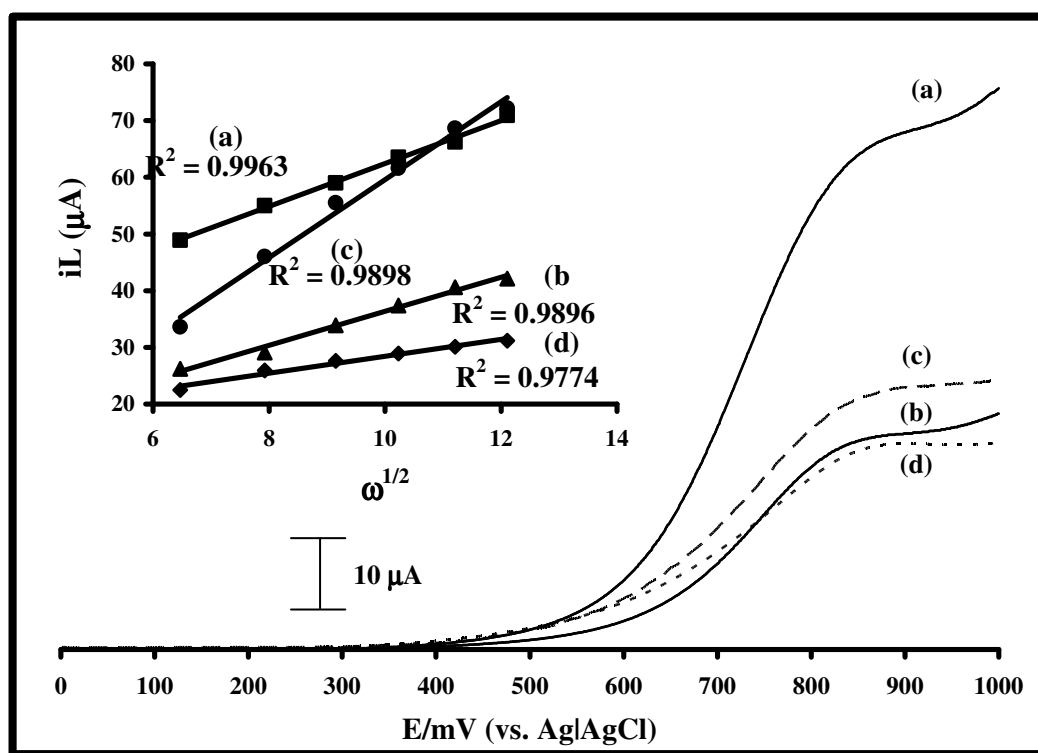


Figure 5. 20: Hydrodynamic voltammograms of L-cysteine (1mM) oxidation on SAM of complex (a) **12**, (b) **13**, (c) **14** and (d) **15**. Rotation rate 800 rpm. Scan rate = 20 mVs⁻¹. Insets are the corresponding Levich plots.

5.2.2 L-cysteine electrooxidation on UMCE and Au coated fiber electrodes

Complexes **12** and **13** were used for the formation of SAMs on UMCE and Au coated fibers. Complex **12** showed better overpotential reduction in the electrocatalysis of L-cysteine, compared to complex **13** on gold disk electrodes. Figure 5.21 (a) shows electrocatalysis of cysteine oxidation using the SAM modified gold UMCE. At the concentration of 1 mM, a crossing over of the cyclic voltammograms at 0.60 V (for **12**-SAM) and 0.67 V (for **13**-SAM) was observed. This was due to passivation of the electrode by cysteine oxidation products. Decreasing the concentration to 0.1 mM resulted in no passivation on both SAM (freshly) modified electrodes (Figure 5.21 (b)). However, for comparison with gold disk electrodes, the concentration of 1 mM was chosen. It is relevant to understand what happens on the electrode surfaces at 1 mM in order to establish the differences between the different electrode geometries. Also a high concentration (1mM) was employed since no L-cysteine oxidation peak was observed for the fiber electrode at lower concentrations.

Cysteine oxidation peaks were observed at 0.84 V and 0.90 V for **12**-SAM and **13**-SAM modified UMCE respectively, Figure 5.21(b) also shows that at lower concentrations catalysis occurred at the same potential (0.95 V) for both SAM modified electrodes which is more positive than observed at higher concentrations. Thus **12**-SAM electrode shows better behavior (at high concentrations) than **13**-SAM electrode in that lower potential for cysteine oxidation is observed at 1 mM L-cysteine concentration. The cysteine catalysis on the UMCE occurs (0.84 and 0.90 V) at much higher potentials compared to catalysis on the disk electrodes (0.55 and 0.65 V), showing that the latter are preferable for cysteine electrooxidation. Figure 5.22 shows that there was a continuous

decrease in current with scan number for the oxidation of cysteine on SAMs of complexes **12** and **13** on Au UMCE showing that these electrodes are not stable. However, the electrodes could be regenerated (> 80 %) by rinsing in pH 4 buffer.

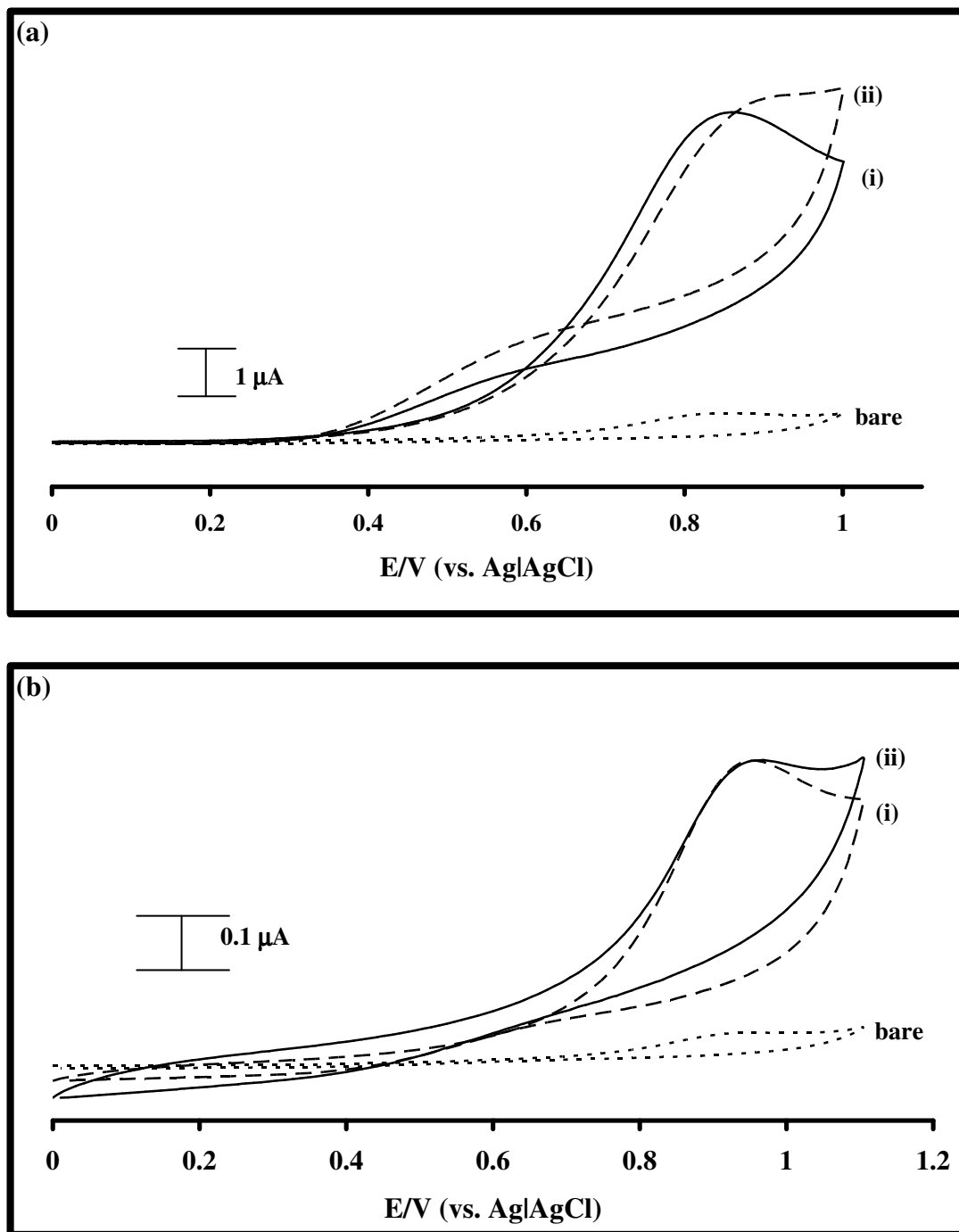


Figure 5. 21: Cyclic voltammograms of bare gold UMC electrode, (i) SAM of complex 12 and (ii) SAM of complex 13 in (a) 1mM L-cysteine in pH 4 buffer solution and in (b) 0.1mM L-cysteine in pH 4 buffer solution. Scan rate = 50 mVs^{-1} .

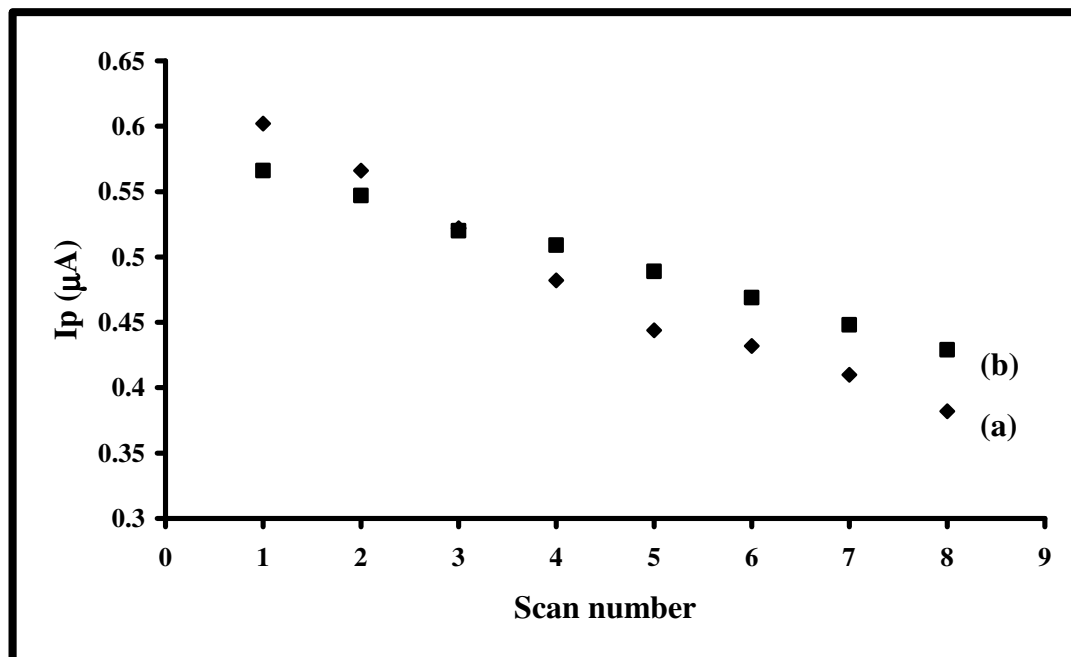


Figure 5. 22: Plot of I_p vs. cyclic voltammetry scan number for the electrocatalytic oxidation of 1mM L-cysteine in pH 4 buffer on (a) **12** and (b) **13** on Au UMCEs.

Figure 5.23 shows L-cysteine electrocatalytic oxidation on SAMs of complexes **12** and **13** on the gold coated fiber. Complex **13**-SAM shows a large increase in the catalytic current, with an oxidation potential of 0.77 V for cysteine oxidation, whereas catalysis with complex **12**-SAM gave an oxidation potential at 0.62 V for cysteine oxidation, but with lower catalytic currents. After the initial scan the gold coated fiber becomes passivated such that the catalytic peak becomes very weak for both SAMs of complexes **12** and **13**, Figure 5.24. The electrode could be regenerated to only 10% by rinsing in pH 4 buffer. However, it is important to note that large current (mA) were observed for the fiber compared to currents produced at the Au disk and Au UMCE bare electrodes (both in μA range). This is because the fiber is made of numerous micro strands. Thus even when the fiber is passivated, it still has higher currents than the Au disk and Au UMCE.

For both the UMCE and Au fiber electrodes, recovery occurs because when rinsing in pH 4 buffer, the oxidation product (cystine) which blocks the active sites on the electrode surface is removed in the process. Cystine is soluble in pH 4 buffer. The recovery process shows that the UMCE recovers best and the fiber hardly recovers at all.

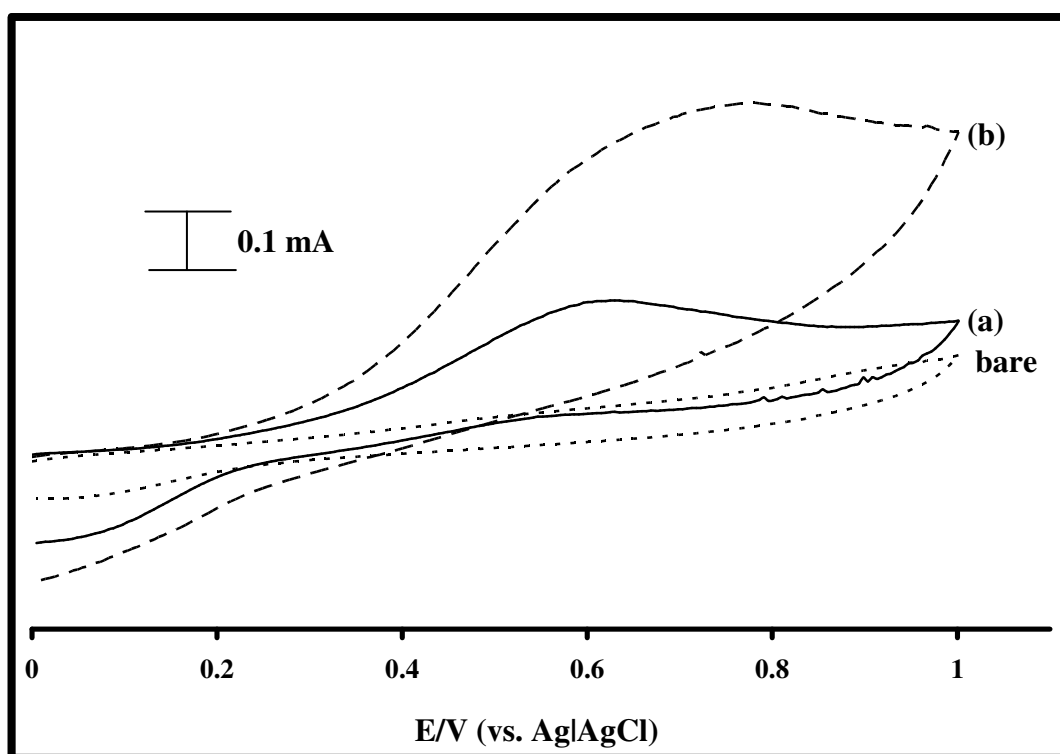


Figure 5. 23: Cyclic voltammograms of bare electrode, (a) SAM of complex **12** and (b) SAM of complex **13** in 1mM L-cysteine in pH 4 buffer solution. Scan rate = 50 mVs⁻¹.

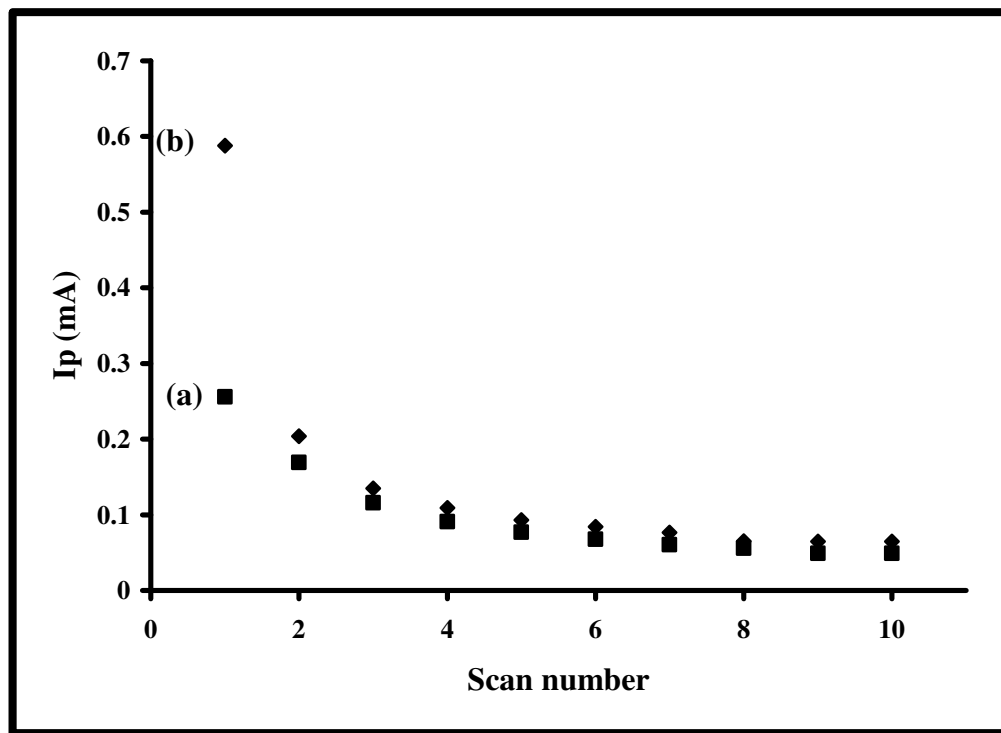


Figure 5. 24: Plot of I_p vs. cyclic voltammetry scan number for the electrocatalytic oxidation of 1mM L-cysteine in pH 4 buffer on (a) **12** and (b) **13** on Au coated fiber electrodes.

Comparing the electrodes modified with complex **12** for cysteine oxidation shows that each Au electrode geometry has its advantages and disadvantages. Comparing Au disk and UMCE showed the latter to have slightly higher currents. In terms of cysteine oxidation overpotential the Au disk outperformed the UMCE by having less positive potential values. Also in terms of stability, the UMCE showed a continuous decrease in current with cyclic voltammetry scan number, whereas the disk stabilized after a 23% decrease in current for **12**. Thus comparing Au disk and UMCE, the former is better for cysteine oxidation in terms of potential and stability. For complex **12** the Au fiber gave much larger currents when compared to both the disk and the UMCE, but gave less

positive cysteine oxidation potential than UMCE and more positive than the disk. However in terms of stability both the fiber and the UMCE performed worse than the disk. Thus in general in terms of overpotential and stability, the Au disk outperformed both the gold coated fiber and the UMCE.

Different overpotential reductions and current increases (sensitivity) were observed for the three electrodes, such differences in electrochemical behaviors suggest that electrocatalysis on the Au surfaces is largely influenced by electrode geometry and electrode size. Electrode geometry plays an important role in determining the type of diffusion on the electrode surface. The disk electrode experiences linear diffusion which suggest that there are less analytes coming to the electrode surface of the disk as compared to UMCE and fiber electrode where mass transport is enhanced due to the non-linear diffusion. This also explains the intense passivation and high current densities experienced at the UMCE and fiber electrode. The fiber electrodes experienced much more increased catalytic currents because the fiber is a bundle of many micro fiber strands.

The potential for cysteine oxidation will be directly related to the $\text{Co}^{\text{III}}\text{Pc}/\text{Co}^{\text{II}}\text{Pc}$ couple of the CoPc derivatives (**12** and **13**) since it is this couple which is known to catalyze cysteine oxidation in acid media [40]. This couple was observed at 0.3V for **12** and 0.4 for **13** in pH 4 buffer, for the Au disk. For UMCE, the $\text{Co}^{\text{III}}\text{Pc}/\text{Co}^{\text{II}}\text{Pc}$ was observed as a very broad feature around 0.4 V for complex **12**. For the fiber, this couple was not clear since it was probably overlapped with peaks due to exposed gold oxide peaks. However it is clear that the lower potential value for cysteine oxidation on Au disk electrode SAMs

for complex **12** is related to the low potential for the $\text{Co}^{\text{III}}\text{Pc}/\text{Co}^{\text{II}}\text{Pc}$ couple on this electrode. The ease of oxidation and hence the enhancement of the catalytic activity may be caused by the fact that non-peripheral substitution enriches the electron density of the π conjugated ring.

5.2.3 L-cysteine detection in biological media

Complex **12** SAM modified disk electrode was used of the detection for L-cysteine in a urine sample, since it showed the best behavior for standard L-cysteine detection. Figure 5.25 shows the differential pulse voltammogram obtained on an unmodified gold disk electrode and on a SAM modified electrode in the presence of human urine without any pre-treatment. Three peaks were determined to be due to ascorbic acid, uric acid and L-cysteine peaks by spiking with standards. The standard addition method was used to determine L-cysteine concentration. On the addition of increasing concentrations of L-cysteine, the three peaks conglomerated to form one peak which increased in current as the L-cysteine concentration increased. Nevertheless L-cysteine concentration in urine was determined from Figure 5.26. This suggests a complex reaction occurring. Figure 5.26 shows the increase of the peak current with increasing L-cysteine concentration. The amount of L-cysteine present in the urine sample was calculated to be 2.4 mM. This was within the urinary L-cysteine excretion range for a healthy human being; (0.03 – 0.3 mmol)/24 hours [119]. These results show that complex **12**-SAM modified gold disk electrode can be efficiently used for L-cysteine detection.

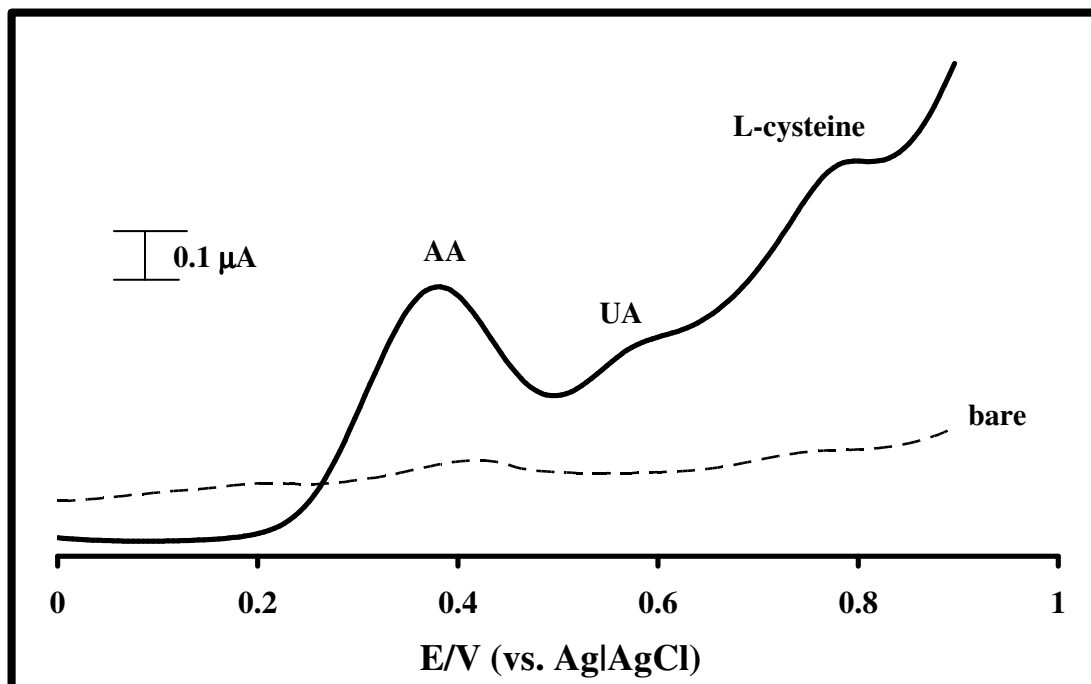


Figure 5. 25: Differential pulse voltammograms of an unmodified gold disk electrode and complex 12 SAM modified gold disk electrode in a human urine sample. AA = Ascorbic acid, UA = Uric acid.

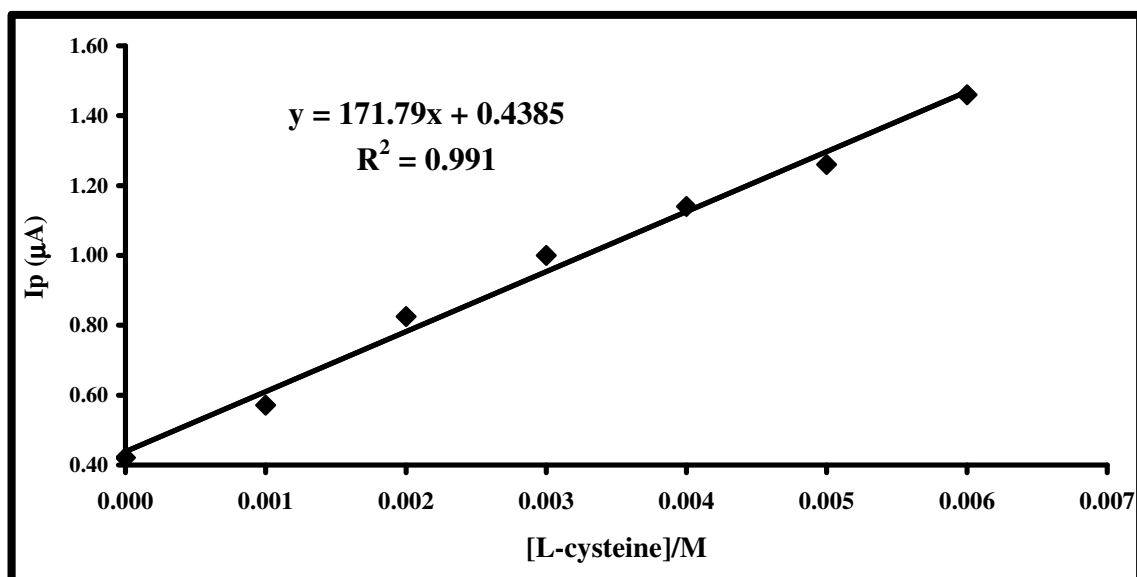


Figure 5. 26: A plot showing the linear dependence of the peak current with increasing L-cysteine concentration in a urine sample.

Conclusion

This chapter has shown *poly-19* modified glassy carbon electrode to be a good sensor for the detection of nitrite (pH 7.4) and complex **12** SAM for L-cysteine (pH 4) detection. This chapter has also shown that for L-cysteine catalysis, electrode geometry and electrode size are factors that influence the efficiency of the catalyst and that the gold disk electrode is the best electrode to use for analysis. Complex **12** SAM and *poly-19* modified electrodes were successfully used in real samples and the results obtained validated these sensors as simple and sensitive electrochemical sensors which have great potential application in biomedical and food analysis.

Chapter 6

Conclusion

6. Conclusion

In this work non-peripherally tetra-substituted Co, Ti and Mn phthalocyanines containing phenylthio and amino substituents were synthesized. These complexes were characterized using spectroscopic and electrochemical methods. Phenylthio and amino substituents are electron donating in nature and have been shown to enhance the electron cloud density of the phthalocyanine ring resulting in red shifted Q-bands. This red shift is further enhanced when the substituents are at the non-peripheral positions.

Cyclic voltammetry was used to characterize the complexes and spectroelectrochemistry was employed to assign the observed redox processes. All the Co complexes showed the same redox processes. The MPcs were immobilized on gold electrodes using self-assembly for the thio substituted complexes and on a glassy carbon electrode through electropolymerization for the amino substituted complexes.

Three gold surfaces were used for SAM formation; a gold disk electrode, a gold ultramicro wire and a gold coated fiber. The SAM modified electrodes were characterized using electrochemical methods (cyclic voltammetry). SAM formation was confirmed by the partial blockage of Faradaic processes and a huge reduction in charging currents. The surface concentration of the SAMs on the gold disk electrodes was of the order of 10^{-10} mol.cm⁻² confirming a phthalocyanine monolayer formation on the electrode surfaces. Redox processes of the surface confined Pc complexes were observed in pH 4 and pH 7.4 buffer solutions, these peaks increased at different scan rates confirming the presence of adsorbed species. The electropolymerized electrodes showed the same stability and had surface concentration values in the order of 10^{-10} mol.cm⁻², but larger 1×10^{-10} mol.cm⁻² suggesting multilayer formation.

The modified Au and glassy carbon electrodes were studied as potential electrochemical sensors for nitrite and L-cysteine. At the bare Au electrode no nitrite or L-cysteine oxidation occurs at the potential range applied whereas on the bare glassy carbon electrode nitrite catalysis occurs at 0.96V vs. Ag|AgCl. The presence of the MPcs on the electrode surface showed enhanced oxidation of nitrite or L-cysteine at lower potentials. This suggests that the MPcs electrocatalyzed the analytes.

Nitrite electrocatalysis on the modified electrodes was performed in pH 7.4 buffer and L-cysteine electrocatalysis in pH 4 buffer solution. The gold UMCE and fiber electrode were used for L-cysteine analysis, the results showed that both electrodes were not stable and overpotential reduction was not as good as those obtained on the disk electrodes. This implies that L-cysteine electrocatalysis may be dependant on electrode size and geometry. High currents were observed for the fiber electrode and high current densities were obtained for the UMCE compared to the disk electrode. The fiber electrodes had a 10% recovery indicating that they can only be used for analysis once, the UMCE however had a good recovery of 80% which was much higher than the 65% recovery obtained on the disk electrodes.

A comparison of the catalytic activities of the modified electrodes shows the following order of overpotential lowering of nitrite and L-cysteine on modified electrodes, CoPcs<MnPcs<TiPcs. CoPc was the most efficient catalyst for both nitrite and L-cysteine oxidation and the $\text{Co}^{\text{II}}/\text{Co}^{\text{III}}$ redox process was responsible for the electrooxidation reactions. Analysis in real samples was conducted and the results showed the CoTAPc complex was able to detect nitrite in a meat sample. The Co phenylthio complex was able to detect L-cysteine in a human urine sample though with

interferences from ascorbic acid and uric acid. This electrode showed to be a promising probe for the simultaneous detection of ascorbic acid, uric acid and L-Cysteine. However attempts to separate these analytes for the standard addition method are required to improve accuracy.

References

References:

1. Fry A. J., Synthetic organic electrochemistry, 2nd Ed., John Wiley & Sons, Inc., Canada, (1986), Chapter 9.
2. Barrera C., Zhukov I., Villagra E., Bedioui F., Páez M. A., Costamagna J., Zagal J. H., *Electroanal. Chem.*, 589, (2006), 212.
3. Wendt H., *Electrochim. Acta*, 29, (1984), 1513.
4. Andrieux C. P., Saveant J. M., *J. Electroanal. Chem.*, 93, (1978), 163.
5. Escudero M. J., Hontanon E., Schwatz S., Boutonnet M., Daza L., *J. Power Sources*, 106, (2002), 206.
6. Michman M., *J. Mol. Cat. A: Chem.*, 107, (1996), 393.
7. Linstead R. P., *J. Chem. Soc.*, (1934), 1016.
8. Dent C. E., Linstead R. P., Lowe A. R., *J. Chem. Soc.*, (1934), 1033.
9. Guillaud G., Simon J., Germain J. P., *Coord. Chem. Rev.* 178-180, (1998), 1433.
10. Collins R. A., Mohammed K. A., *J. Phys. D: Appl. Phys.*, 21, (1988), 154.
11. Zagal J., Bedioui F., Dodelet J. P., In *N4-macrocyclic metal complexes*, Springer: New York (2006).
12. McKeown N. B., *Chem., Ind.*, 92, (1999).
13. Duro A. J., de la Torre G., Barber J., Serrano J. L., Torres T., *Chem. Mater.*, 8, (1996), 1061.
14. Classens C. G., Blau W. J., Cook M., Hanack M., Nolte R. J. M., Torres T., Wöhrle D., *Monatsh. Chem.*, 3, (2001), 132.
15. de la Torre G., Vasquez P, Agulló-López F. *Adv. Mater.*, 9, (1997), 265.

16. de la Torre G., Vaquez P, Agulló-López F, Torres T. J. Mater. Chem., 8, (1998), 1671.
17. Allen C. M., Sharman W., M., van Lier J., E., J. Porphy. Phthal., 5, (2001), 1.
18. Bonnett R., In Chemical Aspects of Photodynamic Therapy, Gordon and Breach Science, Canada, (2000).
19. Barrett P. A., Dent C. E., Linstead R. P., J. Chem. Soc., (1934), 1719.
20. Modibane D. K., Nyokong T., Polyhedron 27, (2008), 1102.
21. Snow A. W., In The Porphyrin Handbook, Kadish K. M., Smith K. M., Guillard R., Academic Press: San Diego, Vol. 17, (2003), 158.
22. Law W.-F., Liu R. C. W., Jian J., Ng D. K. P., Inorg. Chim. Acta, 256, (1997), 147.
23. Stillman M. J., Nyokong T., In Phthalocyanines: Properties and applications Leznoff. C.C. and Lever, A. B. P., VCH Publishers: New York, Vol. 3, (1993).
24. Gregory P. J., Porph. Phthal., 4, (2000), 432.
25. Arslanoğlu Y., Sevim A. M., Hamuryudan E., Gül A. D., Dyes Pigments, 68, (2006), 119.
26. Yiru P., Fenghua H., Zhipeng L., Naisheng C., Jinling H., Inorg. Chem. Commun., 7, (2004), 967.
27. Barrett P. A., Linstead R. P., J. Tvey G. A. P., J. Chem. Soc. (1939), 1809.
28. McKeown N. B., Chambrier I., Cook M. J., J. Chem. Soc. Perkin Trans., 1, (1990), 1169.

29. Maree M. D., Nyokong T., *J. Chem. Res. (S)*, (2001), 68.
30. Sharman W. M., Van Lier J. E., In *The Porphyrin Handbook*, Kadish K. M., Smith K. M., Guillard R., Academic Press: San Diego, Vol. 15, (2003), 1.
31. Wagner H. J., Loufty R. O., Hsiao C-K, *J. Mat. Sci.*, 17, (1982), 2781.
32. Mack J., Stillman M. J., In *The Porphyrin Handbook*, Kadish K. M., Smith K.M., Guillard R., Academic Press: San Diego, Vol. 16, (2003), 46.
33. Lever A. B. P., Milaeva E. R., Spier G., In *Phthalocyanines: Properties and Applications*, Leznoff C. C., Lever A. B.P.:VCH Publishers, New York, Vol. 3, (1993).
34. Kobayashi N. J., In *Phthalocyanines: Properties and applications* Leznoff. C.C. and Lever, A. B.P.: VCH Publishers: New York, Vol. 3, (1993).
35. Nyokong T., Isago H., *J. Porph. Phthal.*, 8, (2004), 1083.
36. Mbambisa G., Nyokong T., *Polyhedron* 27, (2008), 2799.
37. L'her M., Pondeven A., In *The Porphyrin Handbook*, Kadish K. M., Smith K.M., Guillard R., Academic Press: San Diego Vol. 16, (2003), 117.
38. Stillman M. J., In *Phthalocyanines: Properties and applications* Leznoff. C.C., Lever, A. B. P.: VCH Publishers: New York, Vol. 3, (1993).
39. Zagal J., Páez M., Tanaka A. A., dos Santos Jr J. R., C. A. Linkous, J. *Electroanal. Chem.*, 339, (1992), 13.
40. Maree S., Nyokong T., *J. Electroanal. Chem.*, 492, (2000), 120.
41. Gulppi M. A., Paez M. A., Costamagna J. A., Cárdenas- Jirón G., Bedioui F., Zagal J. H., *J. Electroanal. Chem.* 580, (2005), 50.
42. Zagal J. H., *Coord. Chem. Rev.* 119, (1992), 89.

43. Cárdenas-Jirón G. I., Gulppi M. A., Caro C. A., del Río R., Páez M., Zagal J. H., *Electrochim. Acta* 46, (2001), 3227.
44. Linares C., Geraldo D., Páez M., Zagal J. H., *J. Sol. State Electrochem.*, 7, (2003), 626.
45. Obirai J., Nyokong T., *J. Electroanal. Chem.*, 573, (2004), 77.
46. Obirai J., Nyokong T., *J. Electrochim. Acta*, 49, (2004), 1417.
47. Nyokong T., In *N4-macrocyclic metal complexes*, Zagal J., Bedioui F., Dodelet J. P.: Springer, New York, (2006).
48. Tau P., Nyokong T., *J. Electroanal. Chem.*, 611, (2007), 10.
49. Tau P., Nyokong T., *J. Electrochim. Acta*, 52, (2007), 4547.
50. Agboola B., Nyokong T., *Anal. Chim. Acta*, 587, (2007), 116.
51. Zagal J. H., Herrera P., *Electrochim. Acta*, 30, (1985), 449.
52. Mashazi P. N., Westbroek P., Ozoemena K. I., Nyokong T., *Electrochim. Acta*, 53, (2007), 1858.
53. Ozoemena K., Nyokong T., *Electrochim. Acta*, 51, (2006), 2669.
54. Agboola B., Ozoemena K. I., Nyokong T., *Electrochim. Acta*, 51, (2006), 4379.
55. Nanaka T., In *New challenges in organic electrochemistry*, CRC Press, (1998).
56. Murray R.W., Ewing A. G., Durst R. A., *Anal. Chem.*, 59, (1987). 375A.
57. Durst R. A., Bäummer A. J., Murray R. W., Buck R. P., Andrieux C. P., *Pure and Appl. Chem.*, 69, (1997), 1317.

58. Abuña H., In Electroresponsive molecular and polymeric systems, Vol 1., CRC Press (1998) , 98.
59. Cook M. J., Pure Appl. Chem, 71, (2002), 2145.
60. Caro C. A., Bedioui F., Zagal J. H., Electrochim. Acta, 47, (2007), 1489.
61. Khene S., Geraldo D. A., Togo C. A., Limson J., Nyokong T., Electrochim. Acta, 52, (2008), 183.
62. Brown K. L., Mottola H. A., Langmuir, 14, (1998), 3411.
63. Nyokong T., Bedioui F., J. Porph. Phthal., 10, (2006), 1101.
64. Mashazi P. N., Ozoemena K. I., Maree D. M., Nyokong T., Electrochim. Acta, 51 (2006), 3489.
65. Ozoemena K. I., Nyokong T., Electrochim. Acta, 47, (2002), 4035.
66. Simpson T. R. E., Russel D. A., Chambrier I., Cook M. J., Horn A. B., Thorpe S. C., Sensors and Actuators (B), 29, (1995), 353.
67. Westbroek P., Priniotakis G., Kiekens P., Analytical electrochemistry in textiles, Woodhead publishing limited, England, (2005).
68. <http://www.sensatex.com>
69. Pacelli M., Loriga G., Taccin M., Paradiso R., Proceedings of the 3rd International Summer School and Symposium on medical devices and biosensors. MIT, (2006), Boston.
70. Pacelli M., Loriga G., Taccin M., Paradiso R., Gemignani A., Ghelarducci B., J. Telecomm. Inform. Techn., 4, (2005).
71. Schwarz A., Hakuzimana J., Gasana E., Westbroek P., Van Langenhove L., ITMC International Conference, (2007), Casablanca.

72. Xue P., Tao X. M., Kwok K. W. Y., Leung M. Y., Tu T. X., Text. Research Jour. (2004), 929.
73. Bard A. J.; Faulkner L. R., Electrochemical Methods. Fundamentals and Applications, 2nd Ed. Wiley, New York, (2001).
74. Amatore C., In Physical Electrochemistry principles, methods, and applications, Rubinstein I., Marcel Dekker, Inc., New York, (1995).
75. Speiser B., In Encyclopedia of Electrochemistry, Instrumentation and Electroanalytical Chemistry, Unwin P., Wiley-VCH, Vol. 3, Weinheim, (2003).
76. Foster R. J., In Encyclopedia of Electrochemistry, Instrumentation and Electroanalytical Chemistry, Unwin P., Wiley-VCH, Vol. 3, Weinheim, (2003).
77. Amatore C., Mansourhaute E., Simonneau G., Electrochem. Commun., 2, (2000), 81.
78. Kissinger P. T., Heineman W. R., Laboratory techniques in electroanalytical chemistry, 2nd Ed., CRC Press, (1996), 419.
79. Z. Li, M. Lieberman, Langmuir, 17, (2001), 4887.
80. Ozoemena K. I., Nyokong T., Microchem. J., 75, (2003), 241.
81. D. L. Pilloud, X. Chen, P. Dutton, C.C. Moser, J. Phys. Chem., 104, (2000), 2868.
82. Christensen P. A., Hamnett A., Techniques and mechanisms in electrochemistry, Blackie Academic & professional, Glasgow, (1994), 55.

83. Kiafer A. E., Gmez-Kaifer M., *Supramolecular Electrochemistry*, Wiley-VCH, Germany, (1999), 14.
84. Nicholson R. S., *Anal. Chem.*, 37, (1965), 1351.
85. Brett C. M. A., Brett A. M. O., *Electrochemistry principles, methods, and applications*, Oxford University Press, New York, (1993).
86. Wang J., In *Analytical Electrochemistry*, VCH Publishers, (1994), 173.
87. Mount R. A., In *Encyclopedia of electrochemistry, Instrumentation of Electroanalytical Chemistry*, Vol. 3. Wiley-VCH, Weinheim, (2003).
88. Burstein G. T., Preface, *A hundred years of Tafel's equation: 1905-2005*, *Corr. Sci.*, 47, (2005) 2858.
89. Wermeckers B., Beck F., *Electrochim. Acta*, 30, (1985), 1491.
90. Ramarathnam N., Rubin L. J., Diosady L. L., *J. Agric. Food. Chem.*, 39, (1991), 1839.
91. Idrissi L., Amine A., *Analy. Lett.*, 38, (2005), 1943.
92. Badea M., Amine A., Benzine M., Curulli A., Mascone D., Lupu A., Volpe G., Pelleschi G., *Microchim. Acta*, 147, (2004), 51.
93. Chamsi A. Y., Fogg A. G., *Anaylst*, 113, (1998), 1723.
94. Rocha J. R., Kasminsky L., Paixao T.R.L.C., Bertotti M., *Electroanalysis*, 13, (2001), 155.
95. Matemadombo F., Nyokong T., *Electrochim. Acta*, 52, (2007), 6856.
96. Caro C. A., Bedioui F., Zagal J. H., *Electrochim Acta*, 47, (2002), 1489.
97. Wen Z-H., Kang T-F., *Talanta*, 62, (2004), 351.

98. Agboola B., Ozoemena K. I., Nyokong T., *Electrochim. Acta*, 51, (2006), 6470.
99. Matemadombo F., Griveau S., Bedioui F., Nyokong T., *Electroanalysis*, 20, (2008), 1863.
100. Bulaj G., Kortemme T., Goldenburg D. P., *Biochem.*, 37 (1998), 8965.
101. Kleinman W. A., Richie J. P., *Biochem. Pharmacol.*, 60, (2000), 19.
102. Heatfield M. T., Fearn S., Sterenton G. B., Waring A. C., Sturman S. G. *Neurosci. Lett.*, 110, (1990), 216.
103. Cengiz M., Yuksel A., Seven M., *Pharmacol. Res.*, 41, (2000), 423.
104. Ebadi M., Srinivason S. K., Baxi M. D., *Prog. Neurobiol.*, 48, (1996), 1.
105. Bald E., Kaniowska E., Chwatko G., Glowacki R., *Talanta*, 50, (2000), 1233.
106. Ueland P. M., Mansoor M. A., Guttormsen A. B., Muller F., Aukrust P., Refsum H., Svardal A. M., *J. Nutr.*, 126, (1996), 1281.
107. Wang Z. L., Pang D., *J. Electroanal. Chem.*, 283, (1990), 349.
108. Keita B., Contant R., Mialane P., Secheresse F., de Oliveira P., Nadjjo L., *Electrochem. Comm.*, 8, (2006), 767.
109. Mafatle T. J., Nyokong T., *J. Electroanal. Chem.*, 408, (1996), 213.
110. Sehlotho N., Nyokong T., *Electrochim Acta*, 51, (2006), 4463.
111. O'Shea T. J., Lunte S. M., *Anal. Chem.*, 66, (1994), 307.
112. Sehlotho N., Nyokong T., Zagal J. H., Bedioui F., *Electrochim Acta*, 51, (2006), 5125.

113. Ozoemana K.I., Westbroek P., Nyokong T., *Electroanalysis*, 14, (2003), 1762.
114. Sekota M., Nyokong T., *Electroanalysis*, 9, (1999), 1257.
115. George R. D., Snow A. W., *J. Heterocyclic Chem.*, 32, (1995), 495.
116. Young J. G., Onyebuagu W., *J. Org. Chem.*, 55, (1990), 2166.
117. Tau P., Nyokong T., *Dalton Trans.*, (2006), 4482.
118. Acher B. N., Fohlen G. M., Parker J. A., Keshavayya J., *Polyhedron*, 6, (1987), 1463.
119. Chen X., Wang F., Chen Z., *Anal. Chim. Acta*, 623, (2008), 213.
120. Cong F. D., Ning B., Du X. G., Chen D. J., Chen B., *J. Mol. Sci.*, 20, (2001), 27.
121. Sehlotho N., Nyokong T., *J. Electroanal. Chem.*, 595, (2006), 161.
122. Takahashi K., Kawashima M., Tomita Y., Itoh M., *Inorg. Chim. Acta* 232, (1995), 69.
123. Sehlotho N., Durmus M., Ahsen V., Nyokong T., *Inorg. Chem. Comm.*, 11, (2008), 479.
124. Tau P., Nyokong T., *Polyhedron*, 25, (2006), 1802.
125. Losic D., Shapter J. G., Gooding J. J., *Langmuir*, 17, (2001), 3307.
126. Porter M. D., Bright T. B., Allara D. L., Chidsey C. E. D., *J. Am. Chem. Soc.*, 109, (1987), 3559
127. Finklea H., O., In *Electroanalytical chemistry*, Bard A., Runbinstein I., Vol 19, Marcel Dekker, Inc., (1996), 110.

-
128. Agboola B., Ozoemena K. I., Westbroek P., Nyokong T., *Electrochem. Comm.*, 9, (2007), 310.
 129. Claußen A., Ochoa G., Páez M., Costamagna J., Nyokong T., Bedioui F., Zagal J. H. J., *Solid State Electrochem.* 12, (2008), 473.
 130. Griveau S., Pavez J., Zagal J. H., Bedioui F., *J. Electroanal. Chem.*, 495, (2001), 75.
 131. Adzic R. R., Haijo M. W., Yeager E. B., *J. Electroanal. Chem* 260, (1989), 475.
 132. Santos W. R. S., Sousa A. L., Luz R. C. S., Damos F. S., Kubota L. T., Tanaka A. A., Tanaka S. M. C. N., *Talanta*, 70, (2006), 588.
 133. Pournaghi-Azar M. H., Dastango H., *J. Electroanal. Chem.*, 567, (2004), 211.
 134. Chebotareva N., Nyokong T., *J. Coord. Chem.*, 46, (1997), 435.